Titre: Title:	Solvent Cast Direct Ink Writing of Mesoscale Metallic Structures
Auteur: Author:	Chao Xu
Date:	2018
Type:	Mémoire ou thèse / Dissertation or Thesis
Référence: Citation:	Xu, C. (2018). Solvent Cast Direct Ink Writing of Mesoscale Metallic Structures [Thèse de doctorat, École Polytechnique de Montréal]. PolyPublie. https://publications.polymtl.ca/3705/

UNIVERSITÉ DE MONTRÉAL

SOLVENT CAST DIRECT INK WRITING OF MESOSCALE METALLIC STRUCTURES

CHAO XU

DÉPARTEMENT DE GÉNIE MÉCANIQUE

ÉCOLE POLYTECHNIQUE DE MONTRÉAL

THÈSE PRÉSENTÉE EN VUE DE L'OBTENTION

DU DIPLÔME DE PHILOSOPHIAE DOCTOR

(GÉNIE MÉCANIQUE)

DÉCEMBRE 2018

UNIVERSITÉ DE MONTRÉAL

ÉCOLE POLYTECHNIQUE DE MONTRÉAL

Cette thèse intitulée :

SOLVENT CAST DIRECT INK WRITING OF MESOSCALE METALLIC STRUCTURES

présentée par : XU Chao

en vue de l'obtention du diplôme de : Philosophiae Doctor

a été dûment acceptée par le jury d'examen constitué de :

M. TURENNE Sylvain, Ph. D., président

M. THERRIAULT Daniel, Ph.D., membre et directeur de recherche

M. LEBEL LABERGE Louis, Ph.D., membre et codirecteur de recherche

M. KHAMENEIFAR Farbod, Ph. D., membre

M. BROCHU Mathieu, Ph. D., membre externe

DEDICATION

I dedicate the dissertation to my beloved wife, Lu

ACKNOWLEDGEMENTS

I wish to thank all the people who helped me and supported me during my study and living in Canada.

First of all, I would like to express my highest respect and deepest appreciation to my supervisors Professor Daniel Therriault and Professor Louis Laberge Lebel. I am very grateful for their continued support and encouragements that helps me overcome every challenge encountered. During the four and a half years of my Ph.D., they helped me improve my writing skills, showed me how to make great presentations, and encouraged me to attend conferences and scientific competitions. I learnt a lot from them, both the scientific research skills and the abundance of knowledge that is helpful in my life. It is a great time to get along with them through the whole Ph.D. study, full of happiness and laughter. They are helpful and resourceful supervisors, close friends and wise mentors in my life. All the guidance and memories are a great treasure to my life.

I would also thank all the members of the Laboratory of Multiscale Mechanics (LM^2) for their help and company during my study. My special thanks go to Dr. Rouhollah Farahani and Dr. Kambiz Chizari for their advice, help to review my paper and encouragement. I am grateful to Prof. Gilles L'Esperance for the guidance on metallurgy science, Yahya Abderrafai for his help on G-code, Lingyu Yue for teaching me DIC, research associate Isabelle Nowlan for her help on tensile tests, Arslane Bouchemit, Vincent Wuelfrath-Poirier and Olivier Sioui-Latulippe from Centre for Characterization and Microscopy of Materials $(CM)^2$ for helping me on the thermal treatments, the interns Bronagh Quinn, Mohamed Azzouni and Kaiqing Yu for their help on 3D printing, my internship supervisor Sid Banerjee from Advanced Design group of Bombardier Aerospace for his help and interesting discussions.

I would like to acknowledge the financial support from the Fonds de recherche du Québec – Nature et technologies (FRQNT) and China Scholarship Council (CSC).

Finally, I could not accomplish this without the support from my families, especially my beloved wife, Lu Zhang. You are the one in my life. Thank you for your unconditional support in every aspect and bringing me a lovely daughter.

RÉSUMÉ

La fabrication additive (FA), également appelée impression tridimensionnelle (3D), modifie actuellement la façon dont nous concevons et fabriquons des structures de géométrie complexes. La possibilité de fabriquer presque toutes les géométries souhaitées permet la conception des structures requises pour obtenir les meilleures performances plutôt que la facilité de fabrication. FA crée un objet en ajoutant du matériau couche par couche à l'aide d'un modèle de conception assistée par ordinateur (CAD). Les avantages la rendent populaire auprès des chercheurs universitaires et de l'industrie manufacturière. Les processus de fabrication sans moule réduisent considérablement le coût et le temps nécessaires au prototypage rapide. Bien que les matériaux polymères FA soient très avancés pour créer facilement des structures 3D complexes, le métal est indispensable pour de nombreuses caractéristiques telles que la haute résistivité thermique, la conductivité électrique et les performances mécaniques. Les structures métalliques de méso-échelle fabriquées par additif sont largement utilisées dans diverses applications, par exemple les implants médicaux, les batteries, les électrodes et les capteurs. De nombreuses techniques de métal FA commercialisées, par exemple la fusion sélective au laser et la fusion par faisceau d'électrons, reposent sur un faisceau d'énergie de haute intensité pour faire fondre des particules métalliques de micro-taille. Cependant, le faisceau d'énergie nécessite des équipements coûteux et provoque des contraintes résiduelles dans les pièces fabriquées.

L'objectif général de cette thèse est de développer un procédé de fabrication additive à faible coût permettant la fabrication de structures métalliques à méso-échelle présentant des performances électriques et mécaniques très élevées. Tout d'abord, une méthode a été développée pour construire des structures métalliques denses en combinant direct ink writing (DIW) à la température ambiante et traitements thermiques après déposition: frittage et infiltration métallique secondaire. La grande flexibilité du procédé permet la fabrication de géométries personnalisées, par exemple des structures entièrement remplies, poreuses, emboîtées et en surplomb. Ces structures sont imprimées à partir d’une encre métallique hautement concentrée constituée de microparticules d’acier fortement allié (HAS), d’acide poly-lactique (PLA) et de dichlorométhane (DCM). Les structures imprimées sont traitées thermiquement pour le frittage du métal menant à améliorer les performances mécaniques et électriques. La porosité des filaments des structures infiltrées en cuivre ne dépasse pas 0,2%. Des essais de traction et des mesures de conductivité électrique sont

effectués sur les structures infiltrées en cuivre, qui révèlent que le module d'Young est égale à 195 GPa et que la conductivité électrique atteint $1,42 \times 10^6$ S / m. Cette méthode permet la fabrication simple de structures métalliques de hautes performances, ce qui constitue un choix prometteur pour les applications technologiques où le coût est un facteur important.

Par la suite, le procédé a été amélioré en utilisant une encre métallique soluble dans l'eau et respectueuse de l'environnement. L'encre métallique est composée de micro-poudres d'acier, d'un polymère biodégradable: du chitosane, d'acide acétique et d'eau dé-ionisée. Le composite est également réutilisable, ce qui signifie que toutes les structures et les déchets de construction non imprimés correctement peuvent être recyclés et réutilisés pour l'impression 3D en les dissolvant à nouveau dans de l'acide acétique. Les structures fabriquées présentent également des propriétés élevées, par exemple une faible porosité du filament de 1,0%, une conductivité électrique élevée de $1,3 \times 10^6$ S / m et un module d'Young de 160 GPa. Cette encre métallique peut être utilisée pour l'impression 3D de structures métalliques hautes performances, avec un très faible impact sur l'environnement.

Alors que DIW construit un objet couche-par-couche et que chaque couche doit être supportée par des couches antérieures ou par un substrat, certaines structures 3D métalliques complexes comportant des surplombs, de longs ponts ou des creux doivent être imprimées en générant des structures de support ces fonctionnalités. Cependant, le moment de retirer le support est problématique. Le retrait avant le traitement thermique provoque l'effondrement des parties en surplomb en raison d'un manque de support tandis que le support deviendra inséparable de la structure du bâtiment après le traitement thermique. Donc, une méthode d'écriture à encre directe multi-matériaux a été développée pour la fabrication de structures en acier 3D complexes à l'aide d'un support amovible imprimé à partir de cuivre ou d'alumine. Le support en cuivre est fondu et s'infiltre complètement dans les pores de la structure du bâtiment lors du traitement thermique. L'infiltration de cuivre améliore la conductivité électrique de la structure en acier fabriquée de ~400% et la rigidité de 34%. De son côté, le support en alumine est physiquement et chimiquement stable pendant le traitement thermique, ce qui évite toute contamination de la structure d'acier. Le support en céramique demeure fragile, peut-être facilement retiré de la structure d'acier frittée.

Le procédé de fabrication d'additives pour pièces métalliques par écriture directe présenté ici ouvre de nouvelles perspectives pour la fabrication de structures métalliques à méso-échelle présentant

des géométries complexes et de hautes performances. La méthode développée fournit une solution pratique, rentable, respectueuse de l'environnement et pratique pour la fabrication de diverses appareils pour des applications telles que les implants médicaux, les capteurs et les batteries.

ABSTRACT

Additive manufacturing (AM), also referred to as three-dimensional (3D) printing, is currently changing the way we design and fabricate structures due to its ability to build complex geometries that are not accessible by subtractive manufacturing approaches. The ability to fabricate almost any desired geometry enables the design of structures required for best performance rather than ease of manufacturing. AM builds an object by adding material in a layer-by-layer fashion based on a computer-aided design (CAD) model. Abundance advantages of AM make it popular among academic researchers and the manufacturing industry. Few restrictions on the geometry of fabricated structures enable AM to create customized healthcare products. Mold-free manufacturing processes significantly reduce the cost and time for rapid prototyping. Although AM of polymeric materials is highly advanced to easily create complex 3D structures, metal is indispensable for many features such as thermal resistivity, electrical conductivity and mechanical performance. Additive manufactured mesoscale metallic structures are widely used in diverse applications, e.g., medical implants, batteries, electrodes, sensors, aerospace components and dental devices. Many commercialized metal AM techniques, e.g., selective laser melting and electron beam melting, rely on a high-intensity energy beam to fuse micro-sized metal particles. The energy beam, however, requires expensive equipment and causes residual stresses in the fabricated parts.

The general objective of this dissertation is to develop a low-cost additive manufacturing method allowing the fabrication of mesoscale metal structures featuring high electrical and mechanical performances. First of all, a method was developed to build dense metallic structures by combining room-temperature direct ink writing (DIW) and post-deposition thermal-treatments: sintering and secondary metallic infiltration. The high flexibility of the method enables the fabrication of customized geometries, e.g., fully-filled, porous, interlocked and overhang structures. These structures are printed from a highly concentrated metallic ink consisting of highly alloyed steel (HAS) microparticles, polylactic acid (PLA) and dichloromethane (DCM). The as–printed structures are thermally treated to improve the mechanical and electrical performances. The filament porosity of the copper infiltrated structures is as low as 0.2%. Tensile tests and electrical conductivity measurements are carried out on the copper infiltrated structures, which reveal that the Young's modulus is up to 195 GPa and the electrical conductivity is as high as 1.42×10^6 S/m.

This method enables the simple fabrication of high performance metallic structures, which provides a promising choice for technological applications where cost is an important factor.

Subsequently, the method was improved by using a water-soluble and environment-friendly metallic ink. The metallic ink is made up of steel micro powders, a biodegradable polymer: chitosan, acetic acid and deionized water. It is also reusable, which means that any incorrectly built as-printed structures and scrap materials can be recycled and reused for 3D printing by dissolving them again in acetic acid. The fabricated structures also exhibit superior properties, e.g., a low filament porosity of 1.0%, a high electrical conductivity of 1.3×10^6 S/m and a Young's modulus of 160 GPa. The metallic ink can be used for the 3D printing of high performance metallic structures, which demonstrates a low environmental impact and a very effective utilization of metallic materials.

As DIW builds an object in a layer-by-layer fashion and each layer has to be supported by previous layers or a substrate, some complex metallic 3D structures featuring overhangs, lengthy bridges or enclosed hollows have to be printed by generating support structures to hold these features. However, the timing to remove the support is a dilemma. Removal prior to the thermal treatment will cause the overhang features to collapse due to lack of support. Otherwise, the support will become inseparable from the building structure after the thermal treatment. Thus, a multi-material direct ink writing method was developed to fabricate complex 3D steel structures with the help of a removable support printed from copper or alumina. The copper support is melted and completely infiltrates into the building structure during the thermal treatment. It improves the electrical conductivity of the fabricated steel structure by 400% and the stiffness by 34%. The alumina support is physically and chemically stable during the thermal treatment, bringing no contamination to the building structure, which can be easily removed by hand after the thermal treatment. These two types of supports are selected by the desired properties of the fabricated structure.

The direct ink writing metal additive manufacturing method demonstrated herein opens new prospects for the fabrication of mesoscale metallic structures featuring high performance and complex geometries. It provides a promising, cost-effective, environment-friendly and practical solution for the manufacturing of various applications such as aerospace components, medical implants, sensors, dental devices and batteries.

TABLE OF CONTENTS

LIST OF TABLES

LIST OF FIGURES

LIST OF SYMBOLS AND ABBREVIATIONS

AM	Additive manufacturing
CHI	Chitosan
CNTs	Carbon nanotubes
DCM	Dichloromethane
DED	Direct energy deposition
DIC	Digital image correlation
DIW	Direct ink writing
DMF	Dimethylformamide
E	Young's modulus
EBM	Electron beam melting
EDS	Energy dispersive X-ray spectroscopy
EHD printing	Electrohydrodynamic printing
FDM	Fused deposition modeling
HAS	Highly alloyed steel
LMD	Laser metal deposition
MCED	Meniscus-confined electrodeposition
MEMS	Microelectro-mechanical systems
PBF	Powder-bed fusion
PLA	Polylactic acid
PLGA	Poly (lactic-co-glycolic acid)

PM	Powder Metallurgy
PVA	Polyvinyl alcohol
PEG	Polyethylene glycol
PVDF	Polyvinylidene fluoride
R_a	Surface roughness
S	Steel structure
S-Al_2O_3	Steel structure with alumina support
SC-DIW	Solvent cast direct ink writing
SC-3DP	Solvent-cast 3D printing
S-Cu	Steel structure with copper support
SEM	Scanning electron microscopy
SLA	Stereolithography
SLM	Selective laser melting
SLS	Selective laser sintering
T_g	Glass transition temperature
TGA	Thermogravimetric analysis
UTS	Ultimate tensile strength
UV	Ultraviolet
YS	Yield strength
2D	Two-dimensional
3D	Three-dimensional

CHAPTER 1 INTRODUCTION

1.1 Background

Additive manufacturing (AM), also referred to three-dimensional (3D) printing, builds an object by adding material in a layer-by-layer fashion based on a computer-aided design (CAD) model. It is changing the way we design and fabricate structures due to its ability to build geometries that are not accessible by subtractive manufacturing approaches. The ability to fabricate almost any desired geometry enables the design of structures required for best performances rather than ease of manufacturing. Additive manufactured mesoscale metallic structures are widely used in diverse applications, such as medical implants [1], batteries [2], electrodes [3] sensors [4], dental devices [5] and aerospace components [6] due to their high mechanical and electrical performances, few geometrical restrictions and mold-free processes of AM. The most popular and commonly used metal AM technologies are powder bed fusion techniques such as selective laser melting (SLM), selective laser sintering (SLS) and electron beam melting (EBM). [7, 8] In these technologies, fine micro scale metal particles are loaded in a powder bed. An intensive laser or electron beam selectively scans the powder particles to fuse them layer-by-layer. Once completed, the fused part is removed from the powder bed and thoroughly cleaned by removing the unfused particles. The powder bed methods are incapable of fabricating diverse structures such as enclosed volume and fine porous structures. The high-intensity laser system can be expensive and a safety concern. In addition, the repeated high-intensity scanning beam can cause excessive oxidation, metallurgy defects and residual stresses. [9-11]

Solvent cast direct ink writing (SC-DIW) was initially used for AM of polymers, which relies on the extrusion of polymer solution, known as ink, through a micro nozzle and the deposition of the extruded ink on a substrate layer-by-layer to create a 3D object. [12] To overcome some of the shortcomings of powder bed fusion methods, researchers adapted the SC-DIW to metal AM by adding metallic micro- (nano-) particles to the polymer solution, making a highly loaded metallic ink. The metallic ink is extruded through a micro nozzle under an applied pressure. The volatile solvent evaporates rapidly upon extrusion. The polymer turns into a solid and holds the metallic particles as a binder, resulting in a metal-polymer composite 3D structure. To achieve a metallic structure featuring high mechanical and electrical performances, a post-deposition thermal treatment is usually performed to pyrolyze the polymer and sinter the metal particles. Researchers

at Harvard University demonstrated using titanium particles to fabricated metallic scaffolds through SC-DIW.[13] Researchers at Northwestern University reported the fabrication of metallic 3D structures utilizing metal oxides (i.e. Fe_2O_3, NiO and CuO) as the metal precursors.[14] The metal oxides were thermochemically reduced into sintered metal 3D structures in a reducing atmosphere of H_2. As the metal oxides are cheaper than metals, the cost on the materials of this method is lower.

1.2 Dissertation structure

The dissertation consists of seven chapters. Chapter 1 introduces the background of the research and the dissertation structure. Chapter 2 presents a critical literature review related to the research. Chapter 3 identifies the problem, describes the research objectives and introduces the coherence of three articles. The main achievements of the dissertation are given in the format of three peer-reviewed journal papers in Chapters 4, 5 and 6. Chapter 4 demonstrates a solvent cast 3D printing method of fabricating metallic structures and secondary metallic infiltration. Chapter 5 reports the development of a reusable and environment-friendly metallic ink for SC-DIW. In Chapter 6, a multi-material DIW method is developed to fabricate complex 3D metallic structures with removable supports. Chapter 7 provides a general discussion of the results. Chapter 8 draws a conclusion for the entire study, discusses the limitations and provides recommendations for future research.

CHAPTER 2 LITERATURE REVIEW

2.1 Metal AM techniques in mesoscale

In this chapter, metal AM methods in mesoscale are reviewed. Although some mesoscale AM techniques fabricate metal-polymer composites instead of pure metals, they are included in this literature review because a post thermal treatment is usually followed to transfer the composites to pure metal featuring high mechanical and electrical performances. The mesoscale is defined as the feature size in the range of 1-100 mm. As a result, the microscale metal AM methods such as meniscus-confined electrodeposition (MCED) [15, 16], electrohydrodynamic printing (EHD printing) [17, 18], and electroplating of locally dispensed ions in liquid [19, 20] are excluded from this work. In summary, the AM methods that enable fabrication of metallic structures with featuring size of 1-100 mm in one-step or with post thermal treatments are reviewed. The following techniques are included:

- Powder-bed fusion (PBF)
  - Selective laser melting (SLM) / selective laser sintering (SLS)
  - Electron beam melting (EBM)
- Laser metal deposition (LMD)
- Binder jetting
- Stereolithography (SLA)
- Direct ink writing (DIW)
  - Fused deposition modeling (FDM)
  - Solvent-cast direct ink writing (SC-DIW)
  - Laser assisted direct ink writing (laser-DIW)

2.1.1 Powder-bed fusion (PBF)

PBF techniques are the most established and commercialized metal AM methods. They rely on a high-intensity energy beam to locally fuse metal microparticles in a powder bed one layer at a time to build 3D structures. Depending on the type of energy beam and fusion mechanisms, they can be categorized as selective laser melting (SLM), selective laser sintering (SLS) and electron beam melting (EBM).

2.1.1.1 Selective laser melting / selective laser sintering

SLM and SLS use a high-intensity laser as the energy source to fuse metal particles [21-23]. SLM fuses the metal micro particles by melting, whereas SLS fuses the particles by sintering. A typical SLM/SLS machine usually consists of three units: (i) a laser scanning system, (ii) a powder bed, and (iii) a powder delivery system, as shown in Figure 2.1a [24]. The laser scanning system generates an intensive laser and selectively scans the surface of the powder bed according to the CAD model of a 3D object. The metal particles are tightly compacted on a building platform within a tank, creating a powder bed. The particles in the powder bed are usually heated to an elevated temperature to lower the energy needed for sintering or melting. After one layer is selectively scanned and fused by the laser, the platform lowers by one layer thickness. A new layer of metal particles is brought by a roller from the powder delivery system. The 3D object is built in this way layer by layer. Once completed, the fused object is removed from the powder bed and thoroughly cleaned by removing the loose or partially sintered particles. Figure 2.1b presents the printing process of a commercially available SLM printer (SLM@500, SLM solutions, Inc.). An intensive laser selectively scans the metal particles at a high speed of 10m/s. The scanned particles melt and fuse together. The finest layer thickness is typically 20 – 40 μm. The metal building rate is up to 171 cm^3/h [25]. SLM/SLS barely have restrictions on the geometry of the fabricated parts, as the unfused particles act as a support to hold the structure during fabrication. Figure 2.1c displays 3D structures featuring complex geometries fabricated through SLM. Many structures can be arranged in one powder bed and fabricated in one time.

SLM and SLS play an important role in metal AM due to their short manufacturing time, the high mechanical performance of the fabricated parts and few restrictions on the geometry. An increasing number of metals are used in SLM/SLS, including, but not limited to, steel, titanium, titanium alloys, aluminum, nickel based alloys, and cobalt-chrome. SLM and SLS are widely applied in fabricating various applications in medical implants (e.g., titanium hip implant, bridges and crowns in cobalt chrome) [27], aviation and automotive industry (e.g., alumina propeller, stainless steel gears and turbine blade of jet engines made from nickel-based alloys) [27]. However, they are unable to build the structure with enclosed hollows, as the unfused particles inside are impossible to be removed. The high-intensity laser system is expensive and has a potential safety risk. In

addition, the intensive scanning laser beam can cause a dramatic change in temperature, which leads to residual stresses, excessive oxidation and metallurgy defects [28-30].

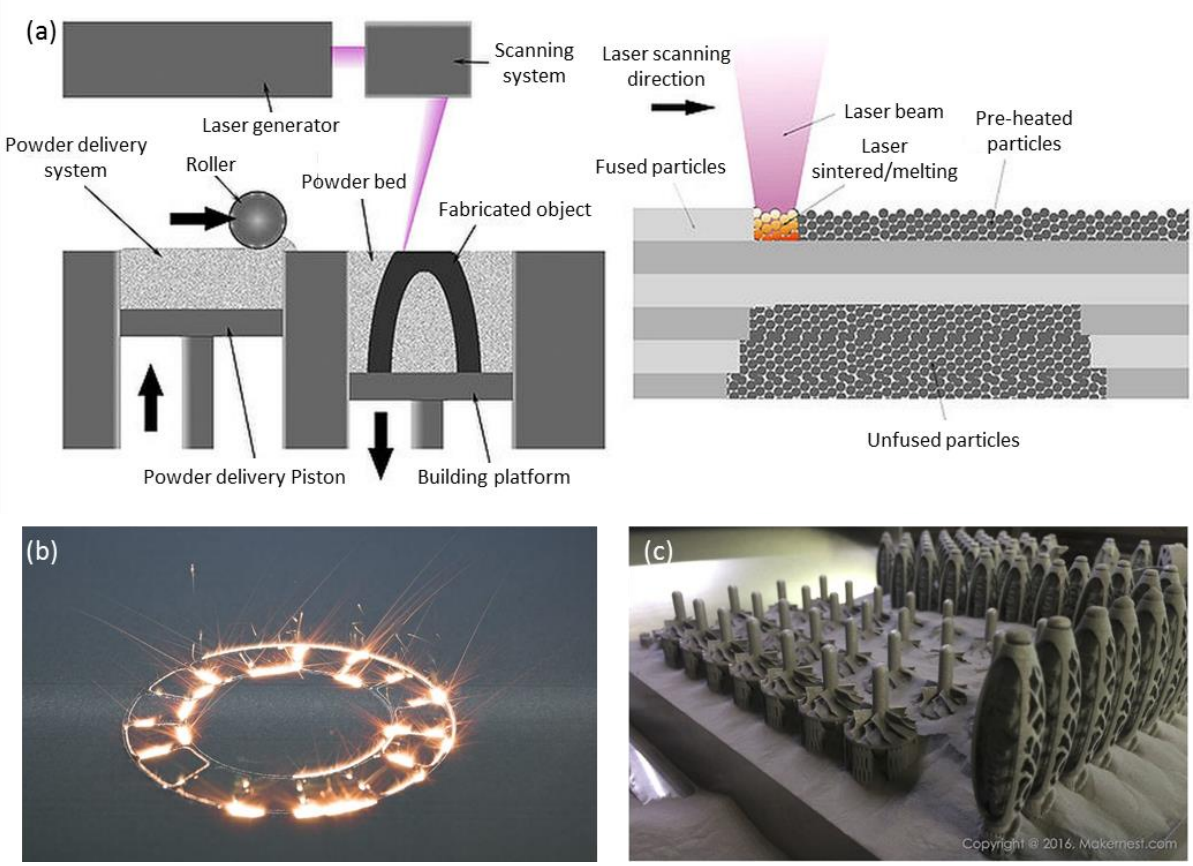

Figure 2.1 SLM and SLS. (a) A schematic of a typical SLM/SLS machine and the printing process [24]. (b) An optical image of SLM process [25]. (c) Metallic 3D structures fabricated through SLM [26].

2.1.1.2 Electron beam melting (EBM)

EBM has similar powder bed and power delivery system as SLM. However, instead of a laser beam, EBM employs an electron beam to melt and fuse the metal particles [31-33]. Figure 2.2 shows a schematic of a typical EBM machine, and photos of the EBM melt pool and a porous metallic structure fabricated through EBM. Due to the use of electron beam as the heat source, parts are necessarily fabricated under vacuum condition. The electron beam heats the metal particles and generates a melt pool to fuse the particles. A fine porous metallic semi sphere is printed through a commercial EBM printer (Arcam Spectra H, Arcam EBM, Inc.) and the resolution is up to 50 – 70

μm [34]. Similar to SLM, EBM is also capable of building various 3D structures with few limitations on the geometry. Diverse metallic particles such as titanium alloy, titanium, inconel and cobalt-chrome, are compatible with EBM. The metallic structure fabricated through EBM are widely applied in medical healthcare [35], automobile and aviation industry [36, 37].

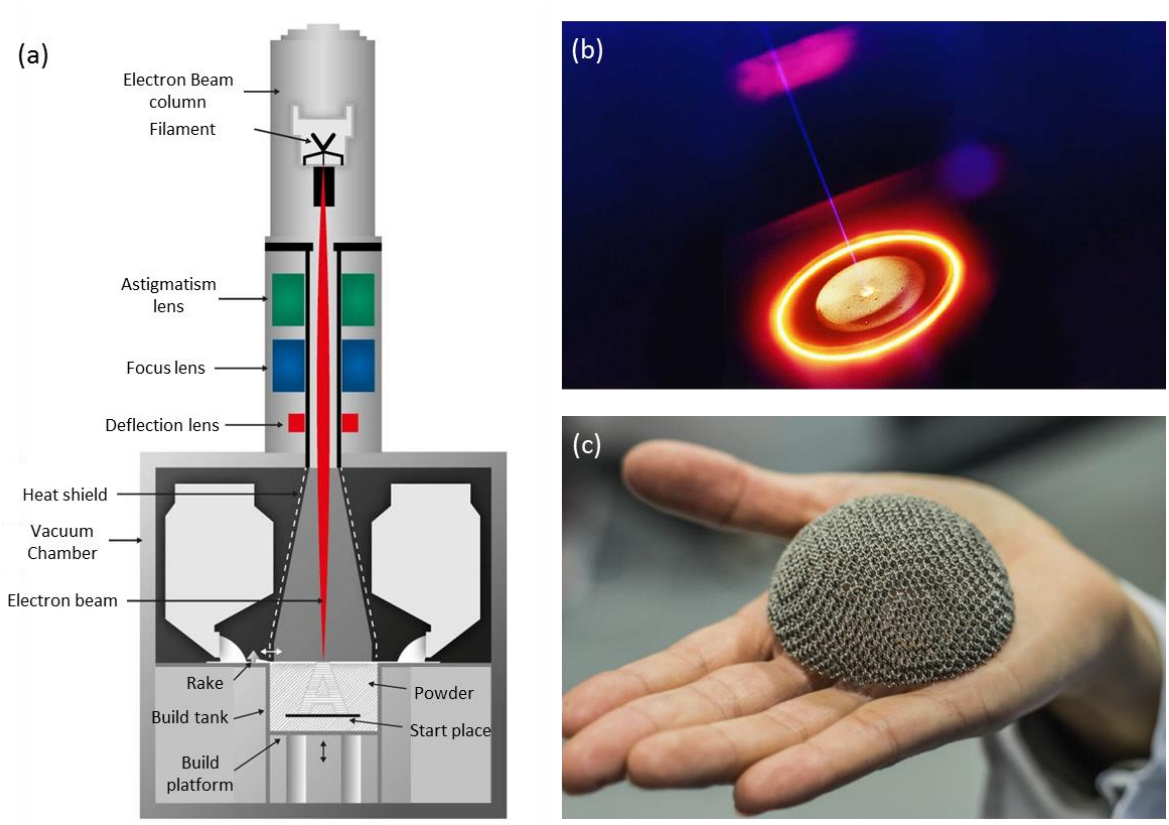

Figure 2.2 EBM. (a) A schematic of a typical EBM machine consisting of a powder bed, a powder delivery system and an electron beam setup [38]. (b) The EBM melt pool [39], and (c) a porous metallic 3D structures printed through EBM [40].

2.1.2 Laser metal deposition (LMD)

Laser metal deposition (LMD), also referred to as direct energy deposition (DED), uses a laser beam to melt metal micro particles that are continuously brought to the print head to build 3D structures [41-43]. Figure 2.3a presents a schematic of a typical LMD printing setup and the printing process. The LMD setup is made up of three major units: the laser system, the powder supply system and the protection gas system. Metal microparticles are consecutively brought to the tip of the print head. The laser beam, which is coaxial with the powder supply system, melts the

metal powders before they reach the workpiece and generates a melt pool. The melt pool is protected against oxidation by shielding inner gas provided by the protection gas system. The melt pool moves as the print head changes the position. The melt pool solidifies by cooling and creates a 3D object layer by layer. Figure 2.3b shows the LMD printing process of a metallic cube. The printed structure is neat and there is no oxidation. LMD is capable to build various metallic structures as displayed in Figure 2.3c. LMD is also capable of retrofitting where adding layers of material to an existing part is required [44, 45].

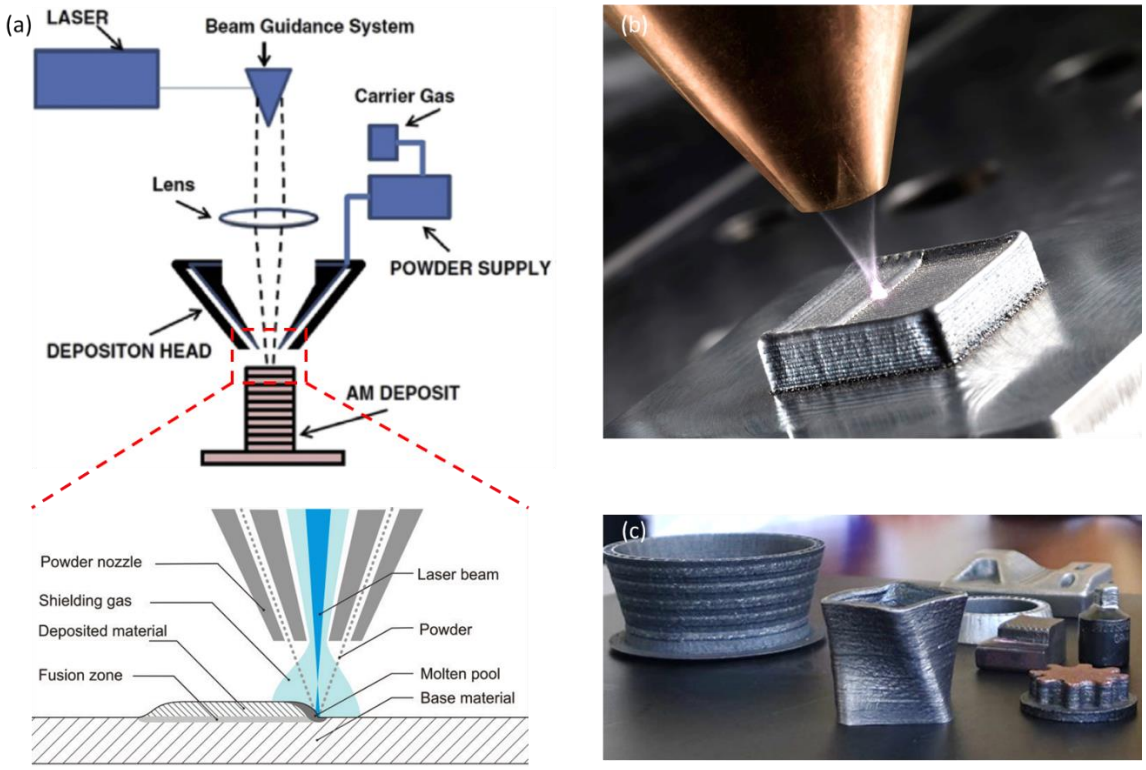

Figure 2.3 LMD (a) A schematic of a typical LMD printer setup and the printing process [46], (b) the printing process of the metallic cube [47], and (c) various metallic 3D structures fabricated through LMD [48].

Various metallic materials are compatible with LMD, such as stainless steel, nickel-based alloys, and copper [49]. Some of them are developed for specific properties, e.g., Fe-Cr-Mn-C for improved wear resistance and Ni-Cr-Al-Fe-Hf for improved oxidation resistance [49]. LMD technique has attracted intense attention in oil and gas sectors, aerospace industry due to its ability to fabricate complex metallic structures in one step [50]. In addition, worn metallic structures can be repaired or refabricated by adding material through LMD [51]. Depending on the processing

parameters and metallic materials, a commercial LMD printer (LENS 850-R, Optomec, Inc.) can achieve building rate of 300 cm^3/h, laser scanning speed of 1.5 m/min and resolution of 40 μm [52]. LMD technique offers rapid building rate and abundance manufacturing capabilities. Compared to powder bed fusion techniques, it presents relatively low heat input and leads to less residual stress in the fabricated parts [53]. However, as the melt pool has to be supported by a substrate or previous layers, LMD is unable to build free-form structures or complex 3D structure featuring overhangs or lengthy bridges. In addition, it is relatively expensive compared to SLM and SLS [54]. As a result, it is not a mainstream metal AM method and considered not robust or repeatable enough compared to powder bed fusion techniques.

2.1.3 Binder jetting

Unlike aforementioned metal AM approaches, binder jetting actually builds metal-organic composite parts instead of pure metal parts. The as-printed parts are turned to pure metal parts through a post-deposition thermal treatment, which will be discussed in details in the following section. Binder jetting is based on selectively depositing liquid binder onto a powder bed to glue metal micro particles layer by layer to build a 3D object [55-57]. As illustrated in Figure 2.4a, a typical binder jetting printer consists of a powder bed, a powder supplier and an inkjet printhead. Metal microparticles are compact in a building platform within a tank, creating a powder bed, similar to the powder bed in powder bed fusion techniques. The inkjet printhead moves according to the CAD model of the object and selectively drops liquid binder on the metal powders to glue them. Once a layer is finished, the build platform lowers by one layer thickness and the powder spreader brings a new layer of metal particles. The process repeats until the object is built. The part being printed is supported within the powder bed by the unbound particles. The as-printed part is removed from the powder bed and carefully cleaned. The as-printed structure is organic binder-metal composites. Then, it is thermally treated in a furnace to burn the organic binder and sinter the metal particles, obtaining a pure metal part. Figure 2.4b presents metallic arts fabricated by a commercially available binder jetting printer (DM P2500) using stainless steel and copper, respectively.

Although binder jetting requires two steps, i.e., printing and thermal treatment, to build a 3D metallic structure, it is superior to the previously mentioned one-step laser based techniques in some aspects. As it is a laser-free process, there is no need for the expensive laser system, which

lowers the cost and minimizes the safety risk. Moreover, binder jetting is faster than powder bed fusion techniques regarding the printing process. The volume printing speed reaches up to 200 cm^3/h (ExOne R2) [58]. However, the post-deposition thermal treatment causes additional cost in terms of time and cost. In addition, the removal of organic binder leads to a low density of the fabricated metal structures, causing relatively poor mechanical performances [59]. Metallic materials including stainless steel, copper and Ti-6Al-4V are compatible with binder jetting process [60]. The fabricated structures are usually applied in rapid prototyping, metal arts and non-structural applications [61, 62].

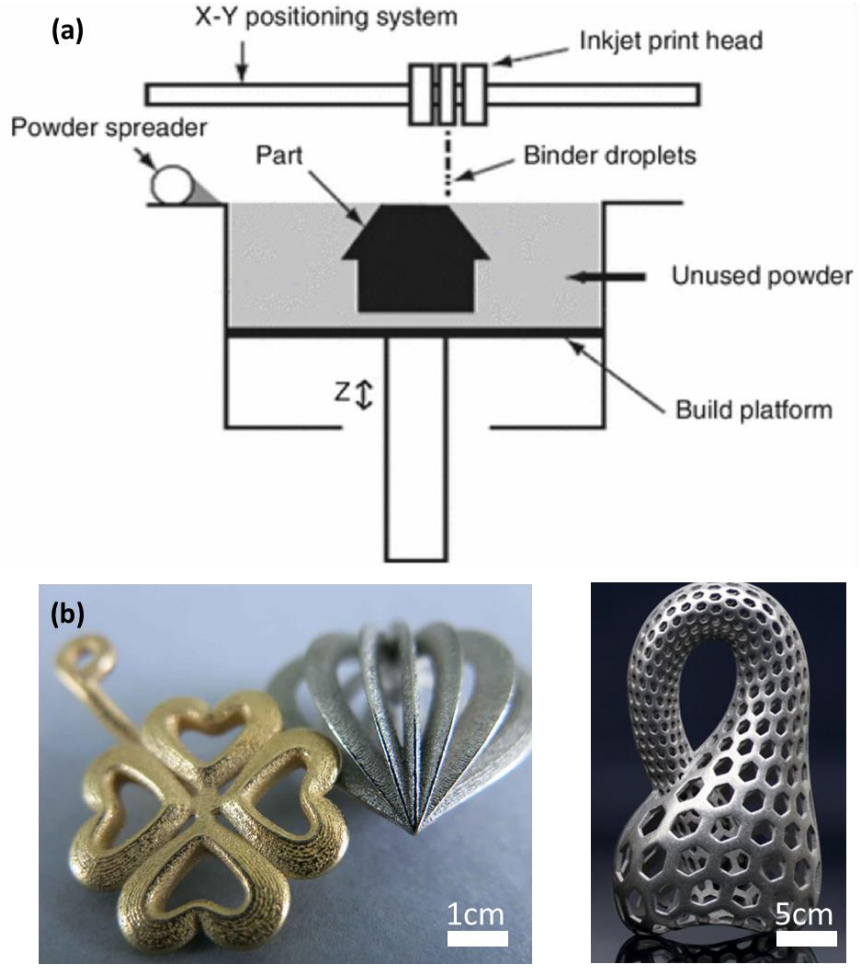

Figure 2.4 Binder jetting (a) A schematic of a typical binder jetting printer [63], (b) 3D metal arts fabricated through binder jetting using stainless steel and copper, respectively [64, 65].

2.1.4 Stereolithography (SLA)

SLA is a photopolymerization based process. It uses an ultraviolet (UV) laser to cure liquid photo monomers in a bath layer by layer to build a 3D object [66-68]. Figure 2.5a shows a conventional SLA setup that consists of a UV light scanner, liquid photo monomers tank and a building platform. The photo monomers are a kind of thermoset resin that can be crosslinked under heat or UV light. This process is called curing [69, 70]. The resin that cures by UV light is referred to as UV curable polymer. It solidifies upon exposure to UV light through curing. When a part is created, the UV light scans the liquid photopolymer contained in the tank guided by a CAD part. The photopolymer is cured and sticks on the build platform as the first layer of the part. After finishing the first layer, the platform lowers by one layer height, the following layer is similarly deposited until the whole part is created. Once completed, the part is removed from the build platform. The uncured resin sticking to the surface is cleaned by rinsing in ethanol. In most commercial SLA printers (e.g., Form 2, Formlabs, Inc.), the build platform is on the top of the resin tank and raised up by one-layer thickness after each layer is created. The part is built bottom-up inversely [71].

SLA was previously a polymeric AM technique, which is recently adapted to metal 3D AM. In order to improve the performances of the fabricated parts, nano- or micro- fillers such as ceramics and metals are added to the resin to make composite structures [72-74]. As the solidification mechanism is the photopolymerization of resin, the amount of the fillers must be carefully controlled to ensure the UV light transparency of the resin. Otherwise, the fillers will block the UV light and the resin cannot be cured by the UV light. Another important factor is the suspension of the filler particles. The particles size should be small enough to form a stable suspension in the resin. If it is too big, the particles will settle down to the bottom of the resin tank and the fabricated structures possess different concentration of fillers in different layers, resulting in an unevenly distributed electrical and mechanical properties. By using the resin with metallic fillers, metal-organic composite structures can be fabricated through SLA [72-74]. To achieve pure metal structures, the as-printed structures pass through a thermal treatment, similar to the one in binder jetting technique. During the thermal treatment, the organic components are burned off and the metallic particles are sintered, resulting in a pure metal structure. Figure 2.5b presents a twisted 3D cross structure and a hollow cylindrical structure fabricated through SLA using UV curable resin with copper micro particle fillers. The overhang features are successfully fabricated as they are supported by the buoyancy provided by the uncured resin.

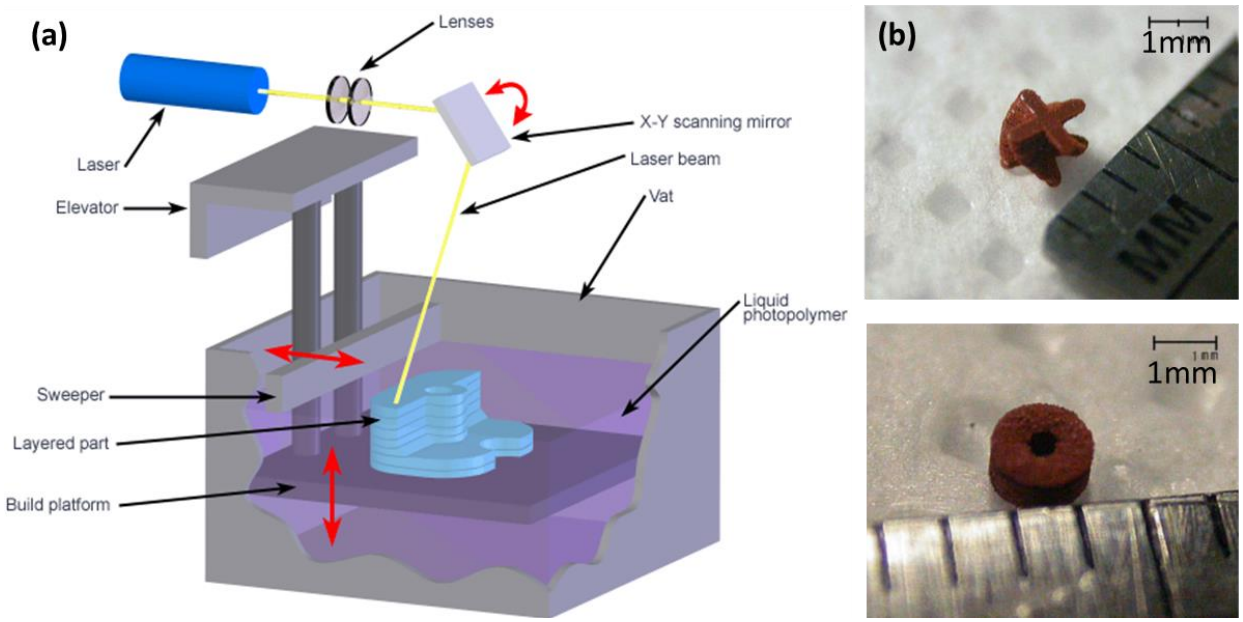

Figure 2.5 SLA (a) A schematic of a typical SLA printer consisting of a UV light scanner, a resin tank and a building platform [75], (b) Metallic structures fabricated through SLA using copper [76].

SLA is compatible only with UV curable resins. The metal nano- or micro- particles can be added to the resin to build metallic structures as long as they satisfy the following requirements: (i) The metallic fillers do not affect the UV light transparency of the resin significantly. (ii) The metallic fillers can form a stable suspension in the resin and will not settle down as time goes. (iii) The metallic particles can be sintered in the subsequent thermal treatment. Recently, the different methods of metal SLA are under development with abundance efforts of many researchers and companies, but they are not maturely commercialized yet. Stainless steel and copper are utilized in metal SLA so far [76, 77]. Compared to other metal AM methods, SLA has a relatively higher resolution. Depending on the materials used and processing parameters (e.g., laser intensity, laser power and scanning speed), the resolution can reach up to 25μm [78]. However, the building rate is lower than other metal AM techniques [79]. SLA is usually applied to fabricate biocompatible medical implants in the healthcare industry [80, 81].

2.1.5 Direct ink writing (DIW)

DIW relies on the computer-controlled layer-by-layer deposition of a filament formed by the extrusion of a viscous liquid, which is called ink, to build a 3D structure [82-86]. Figure 2.6a shows a typical DIW setup, which consists of a print head and a substrate that can move along x, y and z

directions. Figure 2.6b presents a schematic of a continuous filament deposited on a substrate. The ink can be fused polymer, polymer solution and colloids, etc.. Micro- or nano- fillers, such as metal powders, ceramic powders and carbon nanotubes can be added to create composite material inks [87-89]. The viscosity of the ink has to be well tailored for the extrusion process. It should be low enough to facilitate the extrusion through the capillary nozzle. On the other hand, the rigidity of the ink should increase right after being extruded to keep the shape of the filament. The mechanisms can be shear thinning, solvent evaporation induced shape retention and state transfer triggered induced rigidity increase [90]. There are many 3D microstructures fabricated by this technique, for example, a multi-layer porous micro-scaffold made of graphene aerogel as shown in Figure 2.6c.

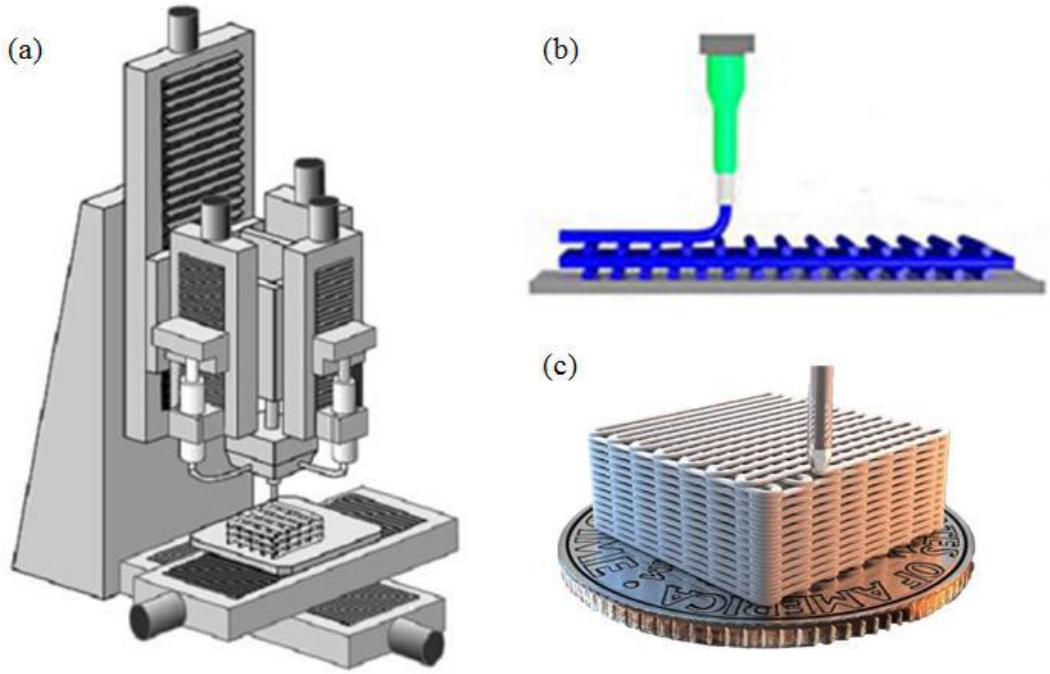

Figure 2.6 DIW fabrication of 3D microstructures. (a) a typical DIW setup consists of a computer-controlled print head and moving stage [91] (b) a filament is layer-by-layer deposited on a substrate [92], (c) a graphene aerogel micro-scaffold fabricated by direct write technique [93,94]

There are three main techniques in this category that are able to fabricate metal or hybrid 3D microstructures: fused deposition modeling (FDM), SC-DIW, and laser assisted direct ink writing. Many novel applications, such as micro-antennas [95], micro-scaffolds for tissue engineering [96-98] and sensors [99-101] can be fabricated by these techniques.

2.1.5.1 Fused deposition modeling (FDM)

FDM has become a widely used commercial 3D printing method since its development in the late 1980s [102]. Conventional setup of FDM technique consists of a heat liquefier chamber, an extrusion nozzle and a platform, as shown in Figure 2.7a. The feedstock, filament shaped material, is heated in the liquefier chamber until it is softened or melted to facilitate the extrusion process [93]. Then it is deposited on the build platform after exiting the extrusion nozzle. Induced by the decrease of the temperature after extrusion, the state of the filament transfers from liquid to solid. As a result, the rigidity required for its shape retention increases. Figure 2.7b shows a commercial FDM printer. By creating a CAD model of an object and inputting it into the printer, the 3D object can be created automatically. Even children can fabricate their own toys with this printer. FDM can be applied to fabricate structures for various applications. Figure 2.7c shows a helical microstructure having 5 turns with a pitch of 0.8 mm and a filament diameter of 0.2 mm fabricated using thermoplastic poly (lactic-co-glycolic acid) (PLGA).

The materials used for the FDM technique were limited to thermoplastics in the past. More recently many novel materials, such as metal/polymer and ceramic/polymer composites [106-108], are now available for this technique. The filament feedstock material for FDM must: 1) soften or melt at a relatively low temperature (around 200-400 ℃) [109] to facilitate the extrusion process, and 2) become quickly stiff when cooled to keep the shape.

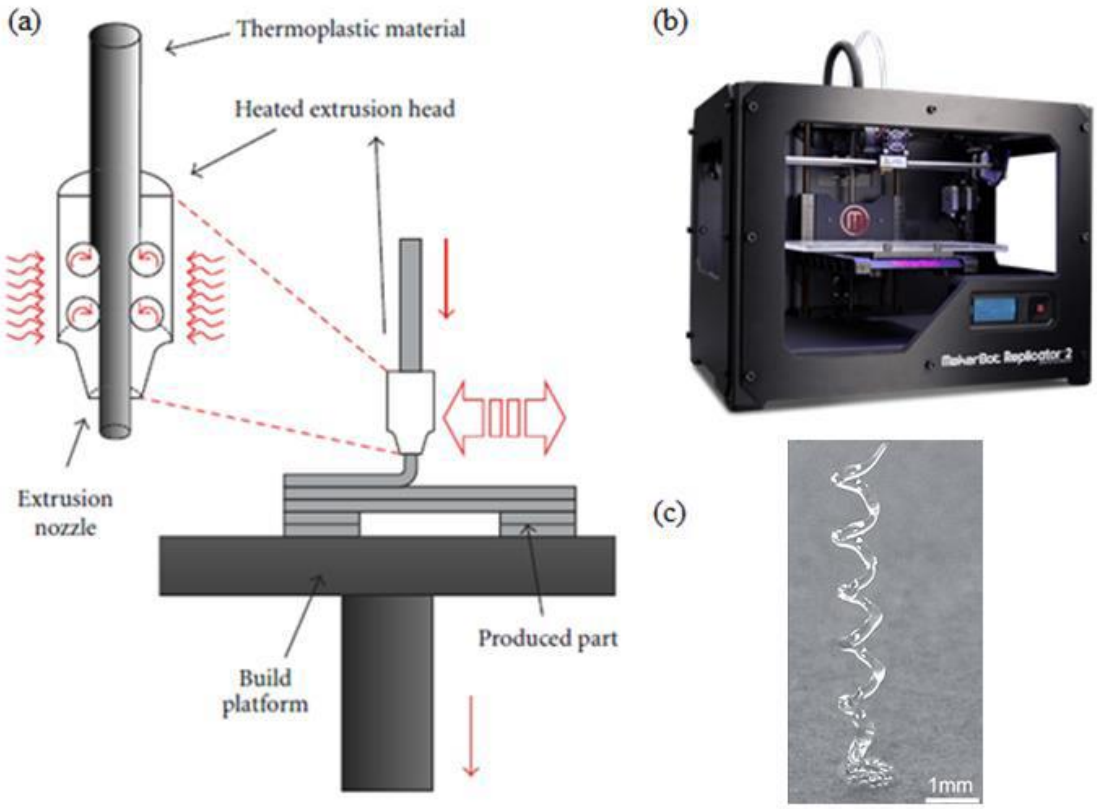

Figure 2.7 FDM fabrication technique (a) schematic of a typical setup consist of a liquefier chamber, an extrusion nozzle and a build platform [103], (b) a commercial FDM printer: MakerBot Replicator [104], (c) optical image of a helical microstructure having 5 turns with a pitch of 0.8 mm and filament diameter of 0.2 mm fabricated using thermoplastic PLGA. [105]

Recently, researchers in MIT and Yale developed an FDM printer which can directly print metals like thermoplastics using a metallic glass feedstock instead of metallic fillers reinforced filaments [110]. Unlike conventional metals, the metallic glasses demonstrated a supercooled liquid region and continues softening upon heating, similar to the thermoplastics. Figure 2.8a and 8b present the schematic of the fabrication process and the physical setup the metal FDM printer. The electrically conductive metallic glass filament is heated by applying current. The electrodes are on the printhead and the substrate. The metallic glass softens upon heated like thermoplastic and deposited on the substrate layer by layer to build a 3D object. Figure 2.8c displays the printing process of a fully dense and pore-free thin wall structure fabricated through FDM using the metallic glass. The structure is orderly stacked layer by layer and there is no obvious oxidation. The cross-section, as illustrated in Figure 2.8d, validates that the structure is fully dense and pore-free, which can lead

to good mechanical properties. This method is a breakthrough in FDM of metallic structures, as it is a one-step process without post-deposition thermal treatment like conventional metal FDM methods. In addition, the printer requires only relatively simple setup compared to laser-based metal AM method, making it cost-effective and safer. However, as it relies on the soften-upon-heated property of metallic glasses, it is only compatible with metal glasses now.

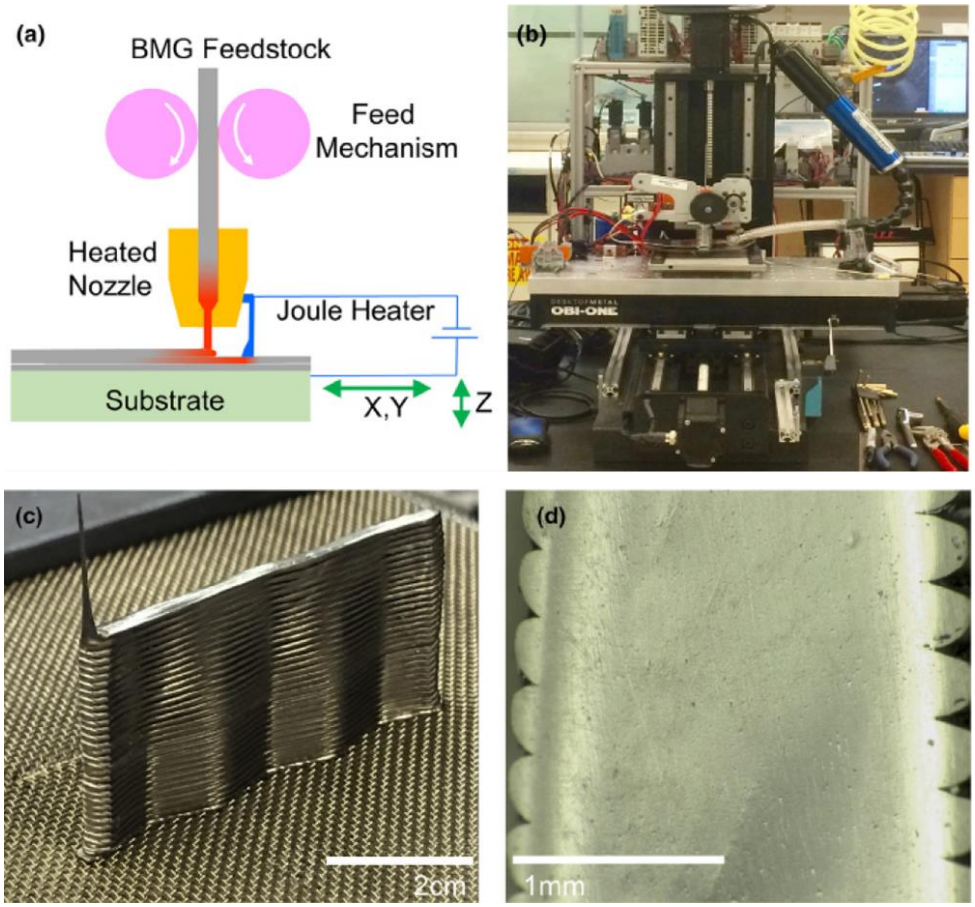

Figure 2.8 FDM of metal metallic glasses (a) schematic of the fabrication process of FDM of metals, (b) physical setup of the metal FDM printer, (c) fully dense and pore-free thin wall structure fabricated using metallic glasses and (d) the cross-section of the fabricated parts [110].

2.1.5.2 Solvent cast direct ink writing (SC-DIW)

SC-DIW uses a polymer solution as the ink, which is a thermoplastic polymer dissolved in a volatile solvent. The ink solution is extruded through a capillary nozzle under a specific pressure [111-113]. The extruded filament is deposited on a computer-controlled moving stage to build a 3D microstructure in a layer-by-layer manner (as shown in Figure 2.9a). The volatile solvent plays

an important role in the printing process. Not only as it dissolves the polymer to decrease its viscosity to facilitate the extrusion process through the fine micro-nozzle, but also it helps the increase of the rigidity of the filament by evaporating at room conditions right after the filament being extruded (Figure 2.9b). Micro- or nano- metal powders, ceramic powders and carbon nanotubes could also be added to build composite microstructures. Ahn *et al.*[114] reported that SC-DW printing of concentrated metallic ink (~70 wt.% TiH_2), consisting of titanium hybrid powder (TiH_2, mean particle size ~20 μm, 4.4.wt% H_2), thermoplastic polymer (PMMA-PnBA-PMMA) and organic solvent (2-butoxyethanol and DBP), is achieved under room conditions (Figure 2.9c). The printed titanium composite microstructures could be transferred to titanium microstructures by heating in a vacuum oven at 1050℃. If the solvent evaporation speed is high enough and the extruded filaments become rigid quickly, free-from structures can be built using this method. Guo *et al*. demonstrated the fabrication of free-form helical structures and supported structures (e.g., scaffolds) through SC-DIW using PLA/DCM ink (Figure 2.9d). Metal oxides are also candidates for the metallic fillers in the ink using in SC-DIW, which will be reduced in the post-deposition thermal treatment in an H_2 atmosphere. Jakus *et al.* reported the fabrication of metallic 3D structures employing metal oxides as the metal precursors [115]. The metal oxides were thermochemically reduced into sintered metal 3D structures in a reducing atmosphere of H_2. Figure 2.9e presents the various 3D structures created through this method using Fe_2O_3, NiO and CuO. The usage of metal oxides instead of metals lowers the cost of raw materials, as metal oxides are usually cheaper than metals.

The main advantage of SC-DIW is that it is simple and possible to print at room conditions. Except for the extrusion nozzle and the moving stage, no additional systems, like heat liquefier chamber or lasers are needed. Another advantage is its good compatibility with various materials. The most commonly used ink of this technique is PLA/DCM solution. A variety of fillers, such as metals, ceramics and CNTs, can be added to it to enlarge the variety of the ink. The viscosity of the ink must be well adjusted. As long as it facilitates the extrusion process and the evaporation process after extruded, it is a qualified ink to be printed by SC-DW. The main drawback of this method is that the commonly used organic solvent (e.g., DCM) is harmful to human bodies and unfriendly to the environment. In addition, since this method uses metal oxides instead of metals as the raw material, massive hydrogen is required during the thermal treatment to chemically reduce them to pure metals. Highly concentrated hydrogen at high temperature can be a safety concern.

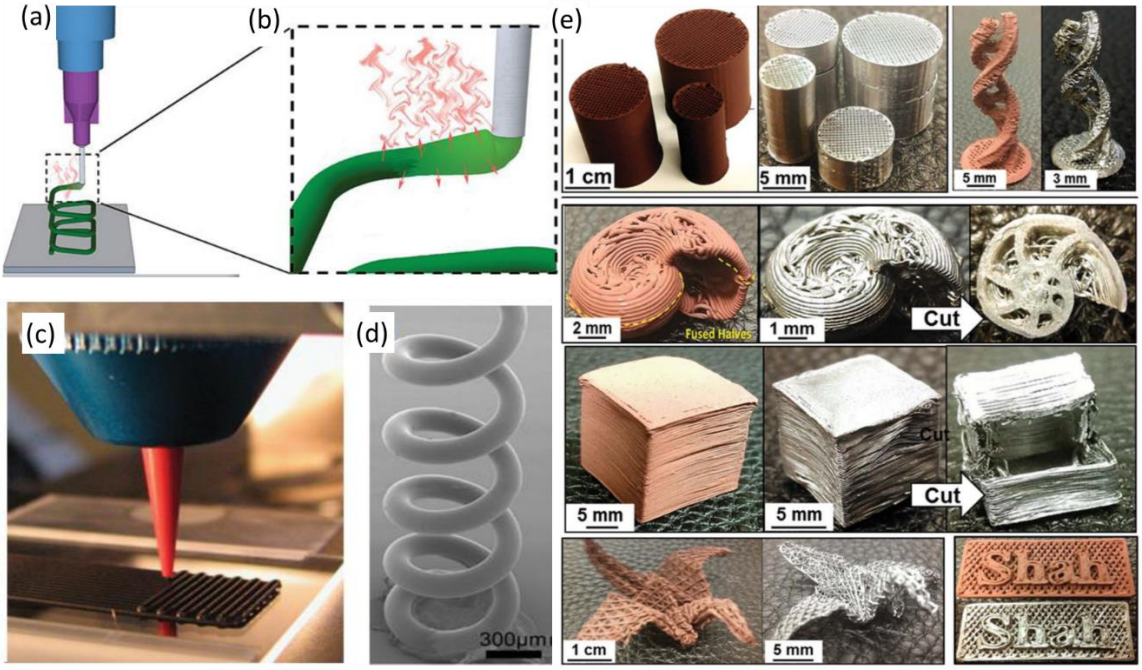

Figure 2.9 SC-DIW techniques (a) a schematic of the print process and (b) solvent evaporation after extrusion [95], (c) solvent cast printing process of metallic ink [114], (d) a PLA helical structure fabricated by SC-DIW [95], and (e) various metallic 3D structures fabricated through SC-DIW using metallic ink [115].

2.1.5.3 Laser assisted direct ink writing

Although SC-DIW demonstrated abundance advantages, it is still an indirect metal AM method where post-deposition thermal treatment is necessary. Moreover, it is hard to achieve free-form fabrication if a heavy metallic filler is loaded in the thermoplastic solution ink. Skylar-scott *et al.* pushed this method to the next stage by developing laser assisted direct ink wiring (Laser-DIW) [116]. In addition to the typical SC-DIW setups, laser-DIW utilizes a focused laser beam to fuse the metallic materials as they are being deposited. Figure 2.10 illustrated the schematic of laser-DIW, the printing process of laser-DIW and the fabricated 3D structures. The ink syringe is positioned obliquely, unlike the vertical position of ink syringe in typical SC-DIW setup. While the laser setup is vertical to sinter the filament right after it is extruded. It combines the deposition and thermal treatment in one step. The metallic ink is water-based silver particle suspensions. Upon heating by the laser, the water evaporates and the silver particles sintered, resulting in a rigid metallic filament (as shown in Figure 2.10B and 2.10C). Figure 2.10D and 2.10E presents the

printing process of a free-form metallic structure. Figure 2.10F displays the top view and side view of the butterflies fabricated using laser-DIW.

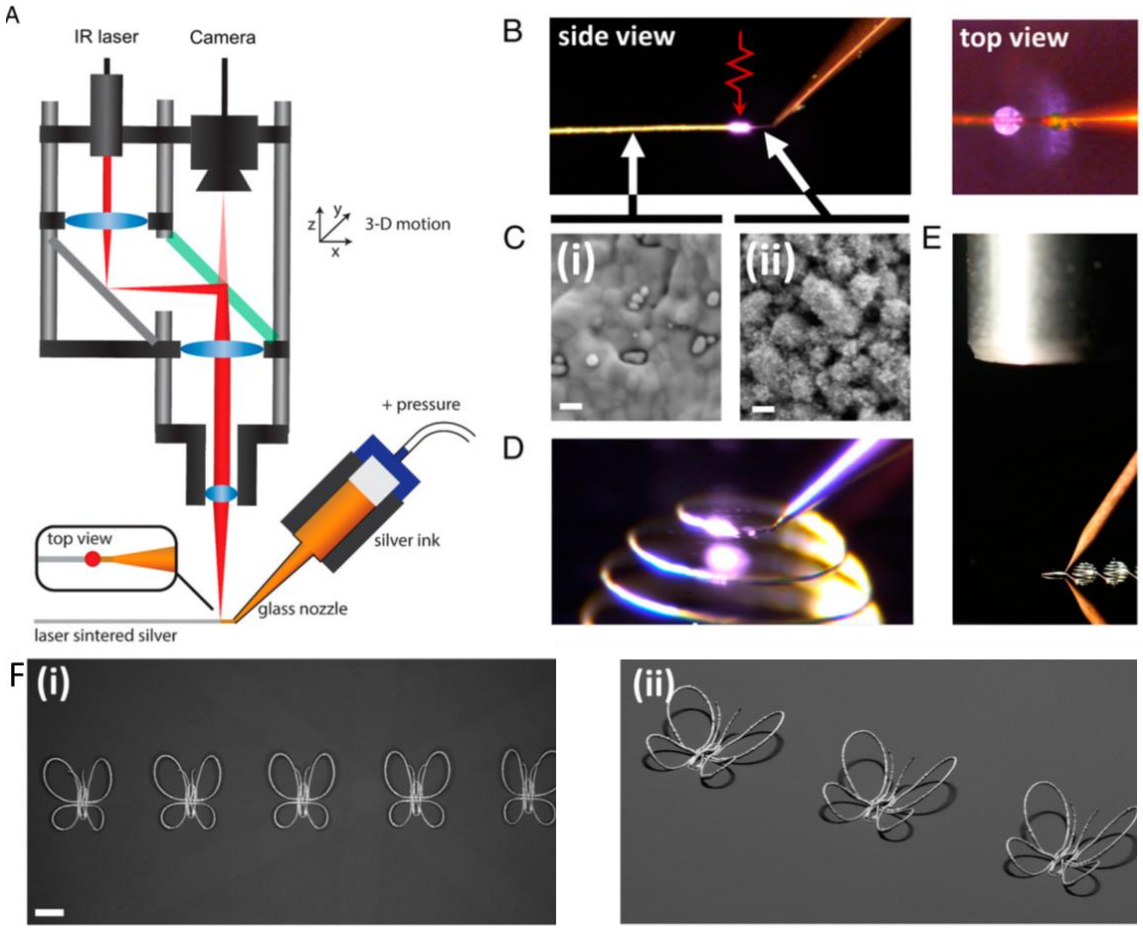

Figure 2.10 Laser-DIW (a) Schematic of the laser-DIW printhead, which consists of the laser microscope, silver ink syringe, and nozzle. (b Side and top views showing the laser (red arrow) focused immediately downstream of the nozzle. Note the change in emissivity of the silver ink upstream and downstream of (C) Nanostructure of (C, i) downstream laser-annealed silver and (C, ii) upstream as-printed silver features. (Scale bar, 100 nm.) (D) The printing process of a metallic structure and (E) the setup. (F) Printed butterflies (scale bar, 1mm) [116].

Laser-DIW is a breakthrough in SC-DIW, which realizes the online sintering and enables the fabrication of free-form metallic structures. However, this method was compatible with only a narrow range of low melting point metals such as silver. Although the mechanical properties were not reported in Ref. [116], given that water evaporation and the sintering of silver powders had to be accomplished within the limited time of laser scanning, the incomplete sintering might lead to

poor mechanical properties of the final product. Furthermore, since this is a laser assisted process, it still suffers from the common laser-induced limitations, like excessive oxidation and the loss of alloying elements.

2.2 Post-deposition thermal treatments

The existing metal AM methods can be categorized as one-step techniques and indirect techniques. The one-step techniques such as SLM, EBM, SLS, LMD, laser-DIW and FDM of metal feedstock create metal structures directly. Indirect techniques build metal-organic composite structures and they are turned to metal structures through post-deposition thermal treatments. The post-deposition treatments usually consist of two necessary steps (i.e., debinding and sintering).

Figure 2.11 shows a schematic representing the process of debinding, sintering and secondary metallic infiltration. The as-printed metal-organic composite structure, also referred to as green part, consist of metal particles and organic binders. The metal particles are covered and bound by the organic binder to hold the structure. Although the bonds provided by organic binder are much weaker compared to the metallic bonding, it is strong enough to hold the structure during the building process. The green part is heated at an elevated temperature, where the organic binder is removed through degradation or pyrolysis. This process is called debinding. After debinding, loose metal particles are left held by the friction forces among the neighboring particles, which is called a brown part. The next step is sintering, which means loose fine metal powders connecting to each other at a temperature lower than their melting point [117]. Sintering can transfer loose metal powders in brown part into solid strong part without losing its original shape [117]. The temperature is raised to a point which is slightly lower than the melting temperature. At this temperature, necks appear between the loose powders to connect each other (sintered part). Sintered part is stronger than the part but is not as strong as bulk materials due to its porosity. The thermal treatment is usually performed in an inner gas atmosphere to prevent the oxidation of metallic particles.

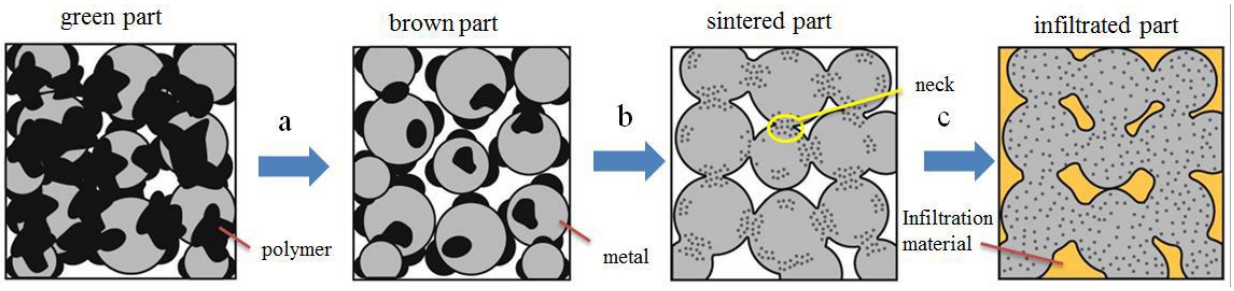

Figure 2.11 Post-deposition thermal treatments: schematic of the process of (a) debinding, (b) sintering and (c) secondary metallic infiltration [118, 119]

Sintering is an important process which is widely used in industry and has many advantages over connecting the metal powders by melting. First, it allows the part to keep its original shape, as the powders are not melted and they are not able to flow as the liquid. Secondly, it enables to create a porous structure, which makes it possible for secondary metallic infiltration to achieve better mechanical and electrical properties. Finally, it needs a lower temperature than melting, which leads to an economy of energy.

CHAPTER 3 RESEARCH OBJECTIVES AND COHERENCE OF ARTICLES

3.1 Problem identification

Although SC-DIW is a promising and practical method of metal AM, there are still a host of efforts to do in SC-DIW of metallic structures. The following problems are imperative to be solved:

- First, there is no metallic structure fabricated through SC-DIW possessing high mechanical and electrical performances that are comparable with those of bulk materials.
- Secondly, most of the metallic inks in SC-DIW approaches contain toxic and volatile organic solvents such as dichloromethane (DCM) and acetone. It can be harmful to the operator and the environment.
- Last but not least, the structures printed by SC-DIW suffers from many geometrical restrictions. As SC-DIW builds a 3D structure layer-by-layer where each layer requires the support from the substrate and previous layers, complex 3D structures with large overhangs or lengthy are difficult to be printed. DIW of polymer can create those structures by printing support underneath the overhang features to hold the structures. Once the printing is completed, the support is removed. However, it does not work for DIW of metal, where a post-deposition thermal treatment is performed. If the support is removed before the thermal treatment, the overhang features will collapse due to the lack of support during the thermal treatment, at a moment when the polymer binder is pyrolyzed while the metal particles are not sintered yet. Whereas, if the support is not removed before the thermal treatment, the support and the building structure will fuse together and become inseparable after the thermal treatment, as they are printed from the same material.

3.2 Research objectives

The main objective of this dissertation is to develop a low-cost AM method based on SC-DIW allowing the fabrication of mesoscale metal structures featuring high electrical and mechanical performances.

To achieve the goal, several specific objectives are presented as follows:

1. Fabricate 3D metallic structures through SC-DIW and post-deposition thermal treatments featuring high mechanical and electrical performances.
2. Develop a secondary metallic infiltration method for the thermally treated structures to further improve the mechanical and electrical performances.
3. Develop a green and environment-friendly polymer solution system, which can be used for the metallic ink of SC-DIW.
4. Develop a reusable metallic ink for SC-DIW.
5. Develop a multi-material SC-DIW method to fabricate complex 3D metallic structures by creating removable support structures using a secondary material.

3.3 Coherence of articles

Chapter 4, 5 and 6 are the core of this thesis, presenting the scientific findings of this work. They cover the general object of development of a low-cost additive manufacturing method based on SC-DIW allowing the fabrication of mesoscale metal structures featuring high electrical and mechanical performances.

Chapter 4 (Article 1) presents the results of the first paper "*Solvent-cast based metal 3D printing and secondary metallic infiltration*", which was published in **Journal of Materials Chemistry C** (Vol. 5, 2017, 10448-10455) (impact factor = 5.976). In this report, a novel metal additive manufacturing method was developed by combining SC-DIW and post-deposition thermal treatments. A highly concentrated metallic ink consisting of highly alloyed steel (HAS) microparticles, polylactic acid (PLA) and dichloromethane (DCM) was used in this method. The fabricated 3D metallic structures feature high mechanical and electrical performances. A secondary metallic infiltration is performed to further improve the properties of the fabricated structures. Specific object 1 and 2 were achieved through this article.

Chapter 5 (Article 2) introduces the results of the second paper "*Environment-friendly and reusable ink for 3D printing of metallic structures*", which was published in **Materials and Design** (Vol. 160, 2018, 262-269) (impact factor = 4.525). In this work, a 3D printable, environment-friendly and reusable metallic ink consisting of chitosan, acetic acid and water was developed. Any incorrectly built as-printed structures and scrap materials can be dissolved again in acetic acid and reused for 3D printing. Specific object 3 and 4 were achieved through this article.

Chapter 6 (Article 3) presents the results of the third paper "*Multi-material direct ink writing (DIW) for complex 3D metallic structures with removable supports*", which was submitted to **Small** (impact factor = 9.598) in November 2018. In this work, a multi-material SC-DIW method was developed to fabricate complex 3D metallic structures by printing support structures from a secondary material. The support could be removed through the post-deposition thermal treatment. The influence of the support on the building structures were investigated by characterizing the dimensional shrinkage, porosity, surface roughness, electrical conductivity and tensile properties. Specific object 5 was achieved through this article.

CHAPTER 4 ARTICLE 1: SOLVENT-CAST BASED METAL 3D PRINTING AND SECONDARY METALLIC INFILTRATION

Published in *Journal of Materials Chemistry C*, Vol. 5, **2017**, 10448-10455.

By

Chao Xu, Arslane Bouchemit, Gilles L'Espérance, Louis Laberge Lebel and Daniel Therriault*

ABSTRACT

Affordable 3D printing methods are needed for the development of high performance metallic structures and devices. We develop a method to fabricate dense metallic structures by combining a room temperature 3D printing and subsequent heat-treatments: sintering and secondary metallic infiltration. The high flexibility of this method enables the fabrication of customized 3D structures, such as fully-filled, porous, interlocked and overhung structures. These geometries are printed using a highly concentrated metallic ink (metallic load up to 98 wt.%) consisting of highly alloyed steel (HAS) microparticles, polylactic acid (PLA) and dichloromethane (DCM). In order to improve the mechanical properties and the electrical conductivity, the as-printed structures are sintered and infiltrated by copper in a furnace protected by a mixture of H2 and Ar. The filament porosity of the copper infiltrated samples is as low as 0.2%. Mechanical testing and electrical conductivity measurement on the copper infiltrated structures reveal that the Young's modulus reaches up to ~195 GPa and the electrical conductivity is as high as 1.42×10^6 S/m. Our method enables the simple fabrication of high performance metallic structures which could open up new technological applications where cost is an important factor.

4.1 Introduction

Metallic structures fabricated by three-dimensional (3D) printing are progressively more used in medical (e.g., artificial bones[1-3]), microwave (e.g., antennas[4,5]), and microelectro-mechanical systems (MEMS) fields (e.g., sensors[6] and micro-electrodes[7-9]). These applications benefit from the high mechanical, electrical and electromagnetic properties of

metals, and the design freedom, mass customization, and ease of use related to 3D printing. Selective laser sintering (SLS)[10,11] and selective laser melting (SLM)[12,13] are commonly used for the fabrication of 3D metallic structures of various sizes. The main techniques use a laser beam to deliver energy on the surface of a powder bed in order to activate bonding between the powder particles. The bonds can be obtained by metallic sintering, metallic melting and binder melting. Typical materials used are titanium alloys,[13-15] while a few studies reported the SLS of steel. For example, McAlea *et al.* reported SLS with polymer-coated steel powders (i.e., 1080 steel, 316 or 420 stainless steel particles coated with thermoplastic polymer blend) followed by a bronze infiltration process. The Young's modulus of manufactured part was 193 GPa.[16] These high temperature fabrication processes require costly laser systems, a large amount of powder to form the powder bed, and several operator protection setups. Moreover, the numerous heat cycles due to repeated laser strikes change the mechanical and chemical properties of the loose powder neighboring the structure's span. As a result, some of the powders cannot be reused.[17] Furthermore, the mechanical properties of SLS/SLM processed parts are usually limited by metallurgical defects such as porosities, cracking, oxide inclusions and loss of alloying elements.[18,19]

Solvent-cast 3D printing is an alternative approach that creates microstructures by depositing a liquid ink on a substrate, layer-by-layer,[20-22] and even in freeform.[23] Inks contain a volatile solvent that evaporates rapidly after extrusion from the deposition nozzle, leading to a rigid filamentary structure. Various ink solutions have been developed for solvent-cast 3D printing, such as polylactic acid (PLA)/dichloromethane (DCM)[23-25] and polyvinylidene fluoride (PVDF)/dimethylformamide (DMF)/acetone[26]. Ink functions, such as conductivity and mechanical properties, are created by adding micro- or nano- fillers including carbon nanotubes (CNTs)[23-25,27], nano-clays[28] and metal microparticles[29,30]. Woo Jin Hyun *et al.* reported the screen printing of 2D filaments with metallic ink loaded with silver nanoparticles synthesized from silver nitrate solution. The electrical conductivity of the as-printed ink filament was 1.8×10^{-7} S/m.[30] Eunji Hong *et al.* reported the solvent-cast printing of titanium ink filaments to build two-dimensional (2D) lattices. The as-printed 2D lattices were rolled into scrolls and heat-treated in a vacuum furnace. The compression yield strength of the scrolls after heat-treatments was 735 MPa.[31] These two methods provide structures with good mechanical properties or electrical conductivity, but are mainly limited

to thin 2D geometries. Another work by Skylar-Scott *et al.* presented a laser-assisted sintering of an ink filament to create 3D freeform metallic structures.[32] While this method is used to print complex wire-type geometries, it is limited to a few compatible materials, susceptible to oxidation and porosity, and is unable to fabricate mechanically strong and highly dense structures.[32] The low-cost 3D printing of highly dense metallic structures featuring complex geometries still represent a significant scientific and technological challenge.

To overcome these current limitations, we propose the solvent-cast 3D printing of metallic inks at room temperature, followed by sintering and secondary infiltration (see Figure 4.1). To demonstrate this proposed concept, a metallic ink is prepared by mixing spherical highly alloyed steel (HAS) microparticles, PLA and DCM. In the printing process (Figure 4.1a), an extrusion device is employed to extrude the metallic ink, which includes a pressure dispensing system, a micronozzle and a syringe barrel that contains the metallic ink. It is mounted on the moving head of a computer controlled 3-axis positioning stage, in order to deposit the extruded ink filament layer by layer on a substrate to create 3D structures.[20-23,33] Right after the ink filament is extruded, the solvent in the metallic ink evaporates rapidly at room temperature and the filament becomes solid. The filament layer is then used as a support for subsequent filament layers to create a HAS/PLA composite multi-layer scaffold. In the as-printed scaffold (Figure 4.1b), PLA serves as a binder holding the HAS microparticles together. To directly connect the HAS particles, the polymer binder is removed by heating the printed scaffold in a furnace above the polymer degradation temperature. The temperature is then rapidly raised to slightly below the melting point of the HAS. At this temperature, sintering occurs by creating necking links between neighboring particles.[34] As time elapses, the necks growth effectively reduces the size and the number of the pores within the metallic continuum. Porosity can be reduced to obtain a strong and conductive filament structure. However, the sintering process can be halted at a porosity favorable for melted copper infiltration (Figure 4.1c). Melted copper flows through the pores within filaments to obtain a highly dense metal/metal composite.

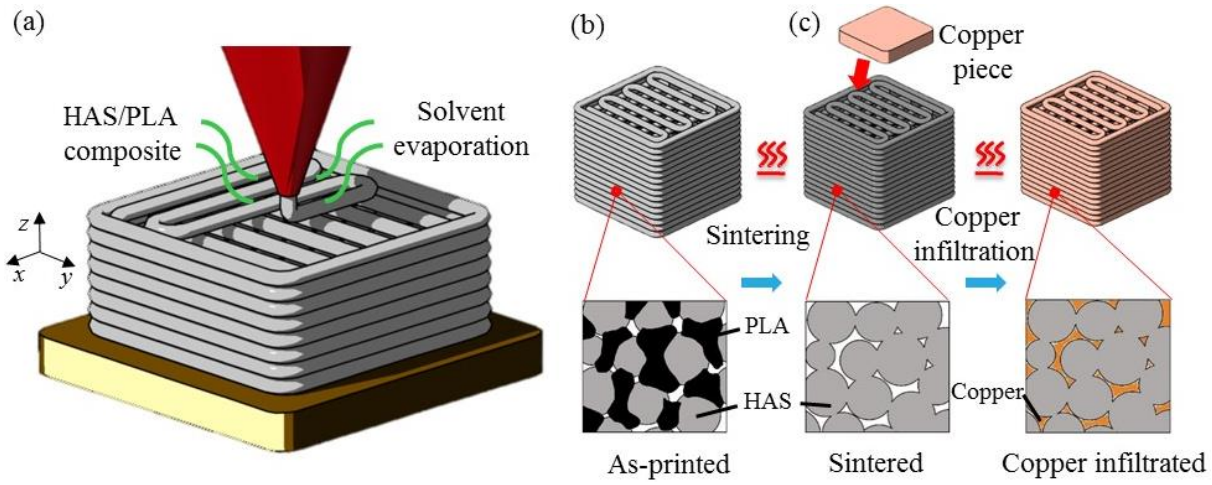

Figure 4.1 Schematic of the fabrication process of a 3D metallic scaffold combining (a) solvent-cast 3D printing: the metallic ink is extruded through a micronozzle and the solvent evaporates right after extrusion at room temperature, (b) sintering: the as-printed scaffold is heated to burn the polymer away and sinter the HAS microparticles, and (c) copper infiltration: the sintered scaffold is heated again with a piece of copper (Cubond IP C-437 infiltration copper) placed on top of it. The melted copper fills the pores within the filament driven mainly by capillary forces.

4.2 Results and discussion

4.2.1 Metallic ink recipe

The HAS powder particles used in this work are fine ($\leq 20\ \mu$m) and have a spherical shape (see Figure 3.S1).[35] The chemistry of this HAS material was designed to replace tool steels and alloyed cast irons in applications requiring high hardness, compression and wear resistance. Regarding the ink extrusion, small particles are desirable in order to avoid clogging in the fine nozzle. Their smooth spherical shape minimizes the area/volume ratio which reduces the friction between the particles and facilitates the extrusion.[36] The PLA solution serves as a lubrication to assist the extrusion of the HAS microparticles through the micronozzle. The solvent is DCM as it efficiently dissolves PLA and rapidly evaporates at room temperature.

The HAS particle concentration within the ink is an important parameter that affects the quality and properties of the fabricated structures. To investigate its influence on as-printed, sintered and copper infiltrated structures, 20-layer scaffolds are printed using HAS/PLA

inks with four different concentrations of HAS particles: 85, 90, 95 and 98 wt.%. The inks are named according to the metal particles weight percentage in the as-printed structure (solid state with no solvent). In the inks, the PLA/DCM weight ratio is 1:4, except for 98 wt.% ink, which is 1:9 (see Table 4.S1 for detailed compositions). The 85 wt.% ink contains the highest amount of solvent, which takes more time to evaporate. As a result, the ink transition from liquid to solid state is slower. This is detrimental to the shape retention of the extruded filament. The surface of the scaffold printed with the 98 wt.% ink is the roughest due to the insufficient amount of PLA (see Figure 3.S2). During sintering, 85 wt.% ink printed scaffolds collapse while the higher concentrated ink successfully preserved their shape during the sintering (Figures 3.S3-S4). Since low concentrated inks contain more polymer, the structure has higher risk to flow and collapse during the heating and removing the polymer binder. Hence, the 95 wt.% ink is selected because it appears to be the best compromise between having a highly concentrated ink for dense sintered structures while ensuring smooth extrusion and low deformation during the solvent evaporation printing.

4.2.2 3D printing of metallic inks

Figure 4.2 shows various 3D structures fabricated using the solvent-cast 3D printing method with the 95 wt.% ink at the printing speed of 10 mm/s, including tensile bars, 20-layer scaffolds, planetary gears and small-scale replicas of Montreal's Olympic stadium. The high flexibility of the technique enables the fabrication of customized structures, such as fully-filled (Figure 4.2a), porous (Figure 4.2b), interlocked (Figure 4.2c), and overhung structures (Figure 4.2d). Figure 4.2a displays the printing process of a tensile bar. The ink uniformly and continuously flows through the micronozzle under a constant pressure. No significant shape distortion is observed. The inset of Figure 4.2a shows several scaffolds and the tensile bar samples next to a Canadian dollar. The fabrication time for the 20-layer scaffold and the fully-filly tensile bar are ~2 min and 30 min, respectively. Figure 4.2b shows the optical images of a 20-layer scaffold from top, side, and oblique views, respectively. The center-to-center distance between neighboring filaments is 0.5 mm and the layer thickness is 0.2 mm. It is observed that the top layer of filaments perpendicularly stacks on the previous layer, by which all subsequent layers are completely overlapped (from top view). The creation of the complete overlap implies the accuracy of the printing. The side view optical image of the structure further shows good layer superposition. It illustrates, additionally,

that the adjacent layers cohere together. A planetary gear consisting of 1 sun gear, 1 ring gear and 4 planet gears is fabricated (Figure 4.2c). The diameter of the ring gear is 30 mm. All the parts of the planetary gear are simultaneously printed and the printed structure requires no assembly. There is an overhung structure in the replica of the Olympic stadium (Figure 4.2d). The overhang part is printed without any additional supporting structures, and it does not bend or deform after printing (tower inclination of ~45°).

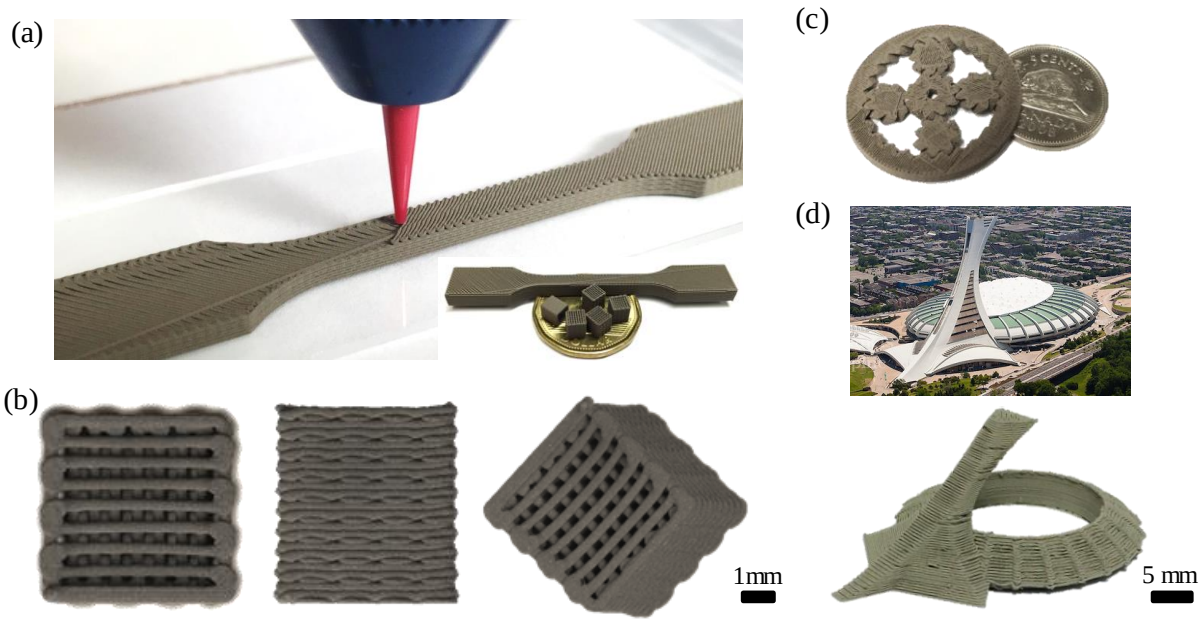

Figure 4.2 Optical images of structures printed with 95 wt.% HAS/PLA ink through 250μm inner diameter tapered nozzle, printing speed of 10 mm/s (a) printing process of a tensile bar sample (inset: a tensile bar and five 20-layer scaffolds placed on a Canadian dollar coin), (b) top, side and oblique views of a 20-layer scaffold (c) a planetary gear with a Canadian 5 cents coin, (d) the Olympic stadium in Montreal[37] and an as-printed replica of the Olympic stadium.

4.2.3 Sintering and secondary metallic infiltration

To improve the mechanical properties and electrical conductivity, the as-printed metal/polymer composite structures are converted to metal and metal composites by sintering and copper infiltration. These heat-treatments are carried out in a laboratory electrical furnace. The heating and cooling rates are adjusted according to the temperature profiles (Shown in Figure 4.S4). To prevent the oxidation of the samples during the heat-treatments, a mixture of H_2 and Ar continuously flows inside the quartz tube of the furnace.

Figure 4.3 presents an optical and SEM images of the as-printed, sintered and copper infiltrated 20-layer scaffolds printed with 95 wt.% ink and 250 μm tapered nozzle. The three types of scaffolds are placed next to each other on a Canadian dollar. The as-printed scaffold has a dark gray color which turns into light gray after sintering. The sintered scaffold shrinks to ~ 84.9% ± 0.6% of the initial size, because the PLA is removed and the HAS particles are brought closer to one another. The copper infiltrated scaffold turns to brown red and its final dimension is reduced to ~ 88.6% ± 0.8% of the as-printed scaffold. The shrinkage observed for the copper infiltrated is slightly less compared to the sintered one probably due to either the shorter duration of the sintering or the extra thickness of copper. No oxidation is observed on the surface of the three scaffolds. No significant distortion happens to the scaffolds after sintering and copper infiltration. The SEM images of the as-printed filaments shows HAS particles are covered and linked together by the PLA binder (Figure 4.3a and Figure 4.1b). Before sintering, a debinding step is required to remove the PLA within the structure. The degradation temperature of the PLA in the samples is around 225 ℃, which is investigated by the thermogravimetric analysis (TGA) on 95 wt.% HAS/PLA sample (See Figure 4.S5). The debinding temperature is set at 300 ℃ to ensure the complete degradation of PLA. After debinding, the structure integrity is held by the friction forces between the HAS microparticles. The low heating rate (60 ℃/h) facilitates the PLA to fully degrade, and prevents the structures from collapsing due to the rapid disappearance of PLA binder. After debinding, the temperature is raised to 1165 ℃ and maintains for 6h. This sintering temperature is set slightly lower than the melting point of HAS for the particles to connect through the apparition of necks between them. The size and amount of the necks increase gradually, which densifies the sintered structure and reduces the pores. A long duration of 6 hours is set to ensure adequate sintering of the HAS particles and obtain a denser structure. In the sintered scaffold (Figure 4.1c and Figure 4.3b), the PLA is completely gone and the HAS particles directly connect with each other through the necks.

If the structure is prepared for copper infiltration, the sintering duration at 1165 ℃ is limited to 1 hour. This shorter sintering duration leave more pores for melted copper to flow through the filaments. A piece of copper is placed on top of the sintered structures inside the furnace (Figure 4.1c). The furnace is heated at 1120 ℃ (see Figure 4.S6). This temperature is higher than the melting point of copper (1085 ℃), but lower than the previously used sintering temperature. The

amount of the copper is calculated by the porosity and the volume of the filaments in the sintered scaffolds. 10 vol.% extra copper is added to ensure that all the pores within the filaments are filled. Mainly driven by capillary forces, the melted copper fills the pores within the filaments of the structure and the sharp corners near connecting filaments (Figure 4.3c).

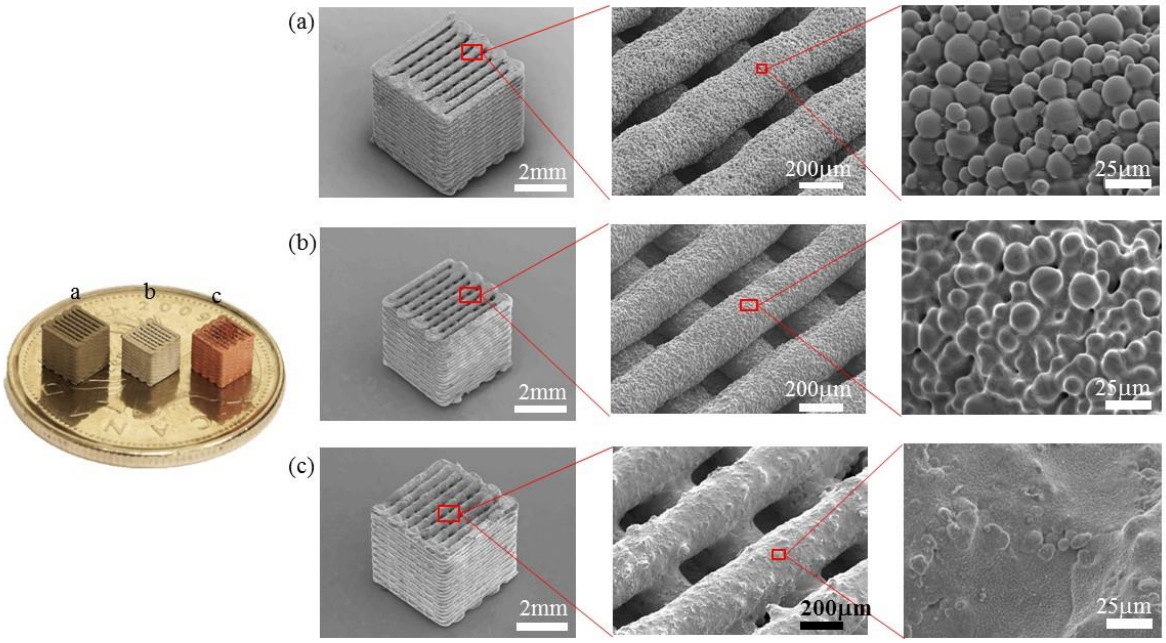

Figure 4.3 Optical and SEM images of 20-layer scaffolds printed using 95 wt.% ink and 250 μm inner tapered nozzle, printing speed of 10 mm/s, (a) as-printed, (b) sintered, (c) copper infiltrated, and their close-up views.

4.2.4 Porosity analysis of sintered and copper infiltrated samples

The filament porosity of sintered and copper infiltrated structures is an important parameter, as it significantly affects the mechanical properties of the structures. To investigate the porosity, each scaffold is polished until reaching three different height positions of 0.2*H*, 0.5*H*, and 0.8*H* (*H* is initial the height of the scaffold). Figure 4.4 shows a Scheme of polishing positions, the representative optical microscope images of the polished cross sections, and the average value of porosities of the sintered (6h) and copper infiltration scaffolds. The first three columns represent the porosities of 90, 95, and 98 wt.% sintered scaffolds, which are 10.4% ± 4.4%, 12.1% ± 5.3% and 12.4% ± 2.0%, respectively. The porosities of 90, 95 and 98 wt.% copper infiltrated scaffolds are extremely low and range from 0.2% to 0.3%, which are presented as the three columns on the right (Table 4.S2). The microscope image of the polished cross section for each type of scaffold is

displayed above each of the column. In the sectional images of sintered scaffolds, we observed that the copper only fills the pores inside the filament, while no large amount copper is outside the filament. Thus, the infiltration flow is limited within the porous filaments rather than empty space between filaments (i.e. interfilamentous pores). The pores have similar sizes and are uniformly distributed within the filament. It is noted that the pores in 98 wt.% sintered scaffold are greater in quantity but smaller in size compared to the others, which results in the smaller error bars. The difference of measured porosities among the three types of sintered scaffolds is lower than 2% despite their different metal to polymer ratios. This can be explained by the densification of the structure at the debinding stage. The polymer is removed and the adjacent HAS particles are brought to similar distances before the sintering is completed. For the copper infiltrated scaffolds, it is observed from the microscope images that the melted copper almost completely fills the porous HAS filaments.

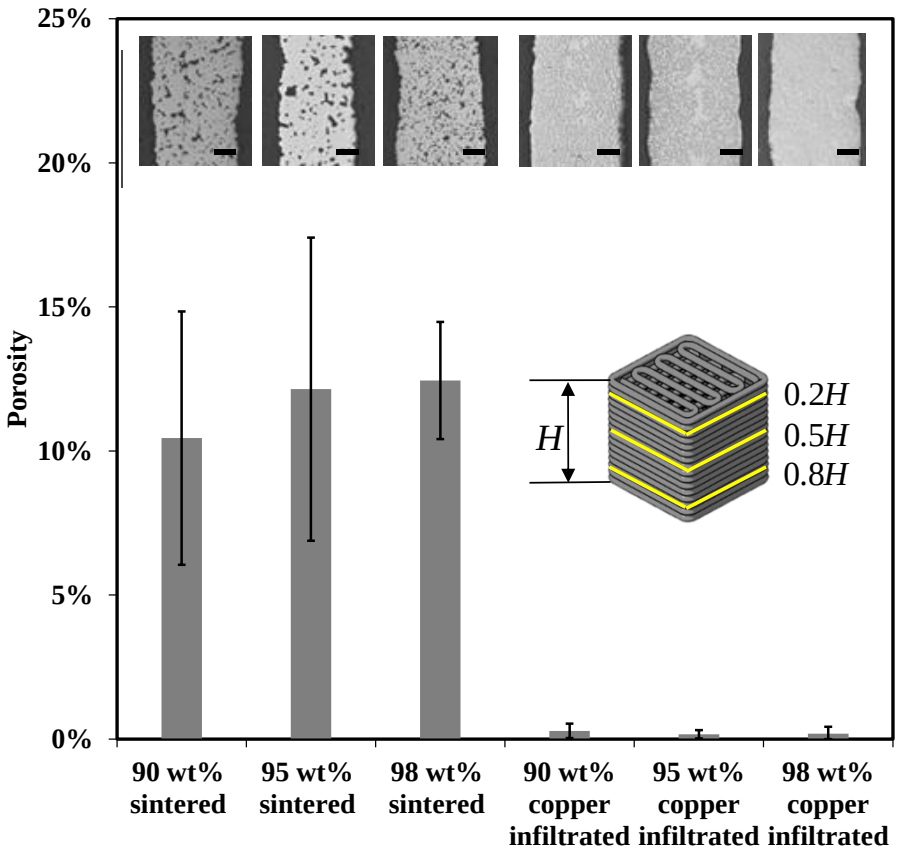

Figure 4.4 Porosity of the filament in the sintered and copper infiltrated 20-layer scaffolds in different ink concentrations, and optical microscope images of the polished cross sections at 0.5*H* (scale bar: 50 μm). Error bars indicate the standard deviations obtained from five samples.

4.2.5 Electrical properties of sintered and copper infiltrated samples

To assess the electrical properties of fabricated structures, the conductivities of sintered and copper infiltrated rods are measured using the four-point probe technique. The conductivity of the sintered samples is $(6.24 \pm 0.18) \times 10^5$ S/m, which is 45% of that of the bulk stainless steel (1.4×10^6 S/m[38]). The relatively lower value is attributed to the pores in the sintered structures. The copper infiltrated sample has a conductivity of $(1.42 \pm 0.32) \times 10^6$ S/m. As copper is more conductive than steel, the conductivity of the sample is further improved after infiltrated with copper.

4.2.6 Mechanical characterization of as-printed, sintered and copper infiltrated samples

Tensile tests are carried out on as-printed, sintered and copper infiltrated tensile bars to evaluate their mechanical properties. Figure 4.5 shows the tensile curves, optical images of representative tested bars and SEM observations of the tensile fracture surfaces. The Young's modulus *E,* Ultimate Tensile Strength (UTS) and Elongation (%) are determined from the tensile curves presented in Fig 3.5a. See Table 4.S3 for more details on the tensile results. The *E* modulus increases (by ~63 times) from 3.1 GPa for the as-printed bars to 196 GPa and 195 GPa after sintering and copper infiltration, respectively. The stiffness achieved is an indication that sintering and copper infiltration are effective and that strong metallic bonds between individual particles are created. The high modulus of the 6h sintered bars is attributed to the dense HAS microstructure. Besides, the copper infiltrated bars are only sintered for 1h creating a porous and more compliant HAS microstructure. However, since the pores were subsequently filled with copper, the effective modulus raised to the same level as the sintered bars. The *E* modulus obtained after sintering and copper infiltration are similar to those of wrought and cast steels.[39] The UTS also increases (by 17 - 18 times) from 28 MPa for the as-printed bars to 485 MPa and 511 MPa after sintering and copper infiltration, respectively. These UTS values are similar to those obtained for carbon steels, stainless steels, tools steels and highly-alloyed cast irons[39]. The rather low ductility of the sintered and copper infiltrated tensile bars is partly explained by the composition of the HAS material. The large volume fraction of carbides results in elongation at break lower than 1 %. Such elongation values are also typical of some tool steels, highly alloyed cast irons (elongation 1 – 10%)[39] and many Powder Metallurgy (PM) steel parts (0 – 3%)[40].

The SEM images of tensile fracture surfaces (Figure 4.5b, c) show the internal structure of the sintered and copper infiltrated tensile bars. The tensile fracture always occurs at the interface of the filaments oriented transverse to the tensile directions, as the stress is maximal at this point. This also explains the lower ε_f value compared to bulk stainless steel (68.2%). The high magnification SEM images (Figure 4.5d, e) reveal the details of tensile fracture surface. There are visible pores, under SEM, within the filaments of sintered tensile bars. In addition, the filament from adjacent layers are bound firmly, while some filaments from the same layer are detached. This is the main reason why the ductility of the samples is lower compared to the bulk stainless steel.

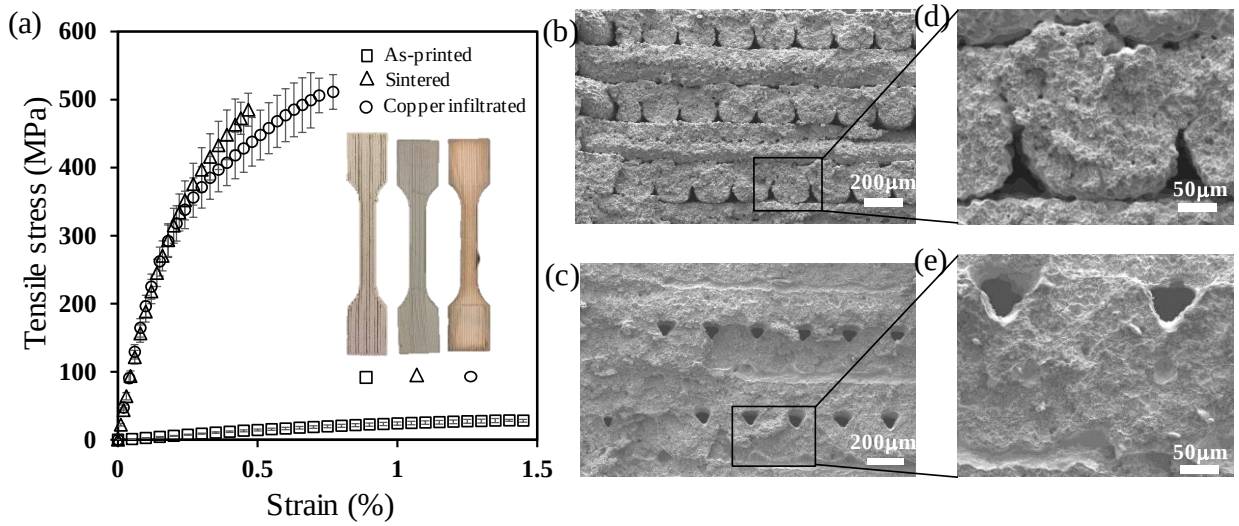

Figure 4.5 (a) Tensile mechanical response for as-printed, sintered and copper infiltrated 3D printed tensile bars. Error bars indicate the standard deviations obtained from three samples. Tensile fracture surfaces of sintered and copper infiltrated tensile bars at (b, c) low and (d, e) high magnification, respectively.

4.3 Experimental

4.3.1 Materials

2g of PLA (4032D, Natureworks LLC, glass transition temperature T_g =50-60 ℃) is dissolved in 8g of DCM (Sigma-Aldrich, boiling point=39.6 ℃) to prepare polymer solutions. After resting for 24h, the solutions are sonicated in an ultrasonic bath (Ultrasonic cleaner 8891, Cole-Parmer) for 5 minutes. The metallic inks are prepared by mixing the

polymer solution and HAS microparticles using a ball mill mixer (8000M Mixer/Mill, SPEX SamplePrep) for 5 minutes.

4.3.2 3D printing

The inks are loaded into 3 cc syringes (EFD) attached to a smooth-flow tapered nozzle (exit inner diameter = 250μm, EFD). Loaded syringes are mounted on a pressure dispensing system (HP-7X, EFD), which is placed on a computer controlled 3-axis positioning stage (I&J2200-4, I&J Fisnar). The ink is printed on a glass slide (PN 16004-422, VWR). The scaffolds, tensile bars and Olympic stadium are printed at a speed of 10 mm/s and under a pressure around 0.7 MPa using the 95 wt.% concentrated ink. These structures are designed by a computer aided design software (i.e. CATIA) and sliced into several layers by a slicing software (i.e. Cura). Each layer is filled by a filament path and the filament path is interpreted to G-code. Then the G-code is converted by a customized python program into a point-to-point program that can be recognized by the JR Points software to control the positioning moving stage.

4.3.3 Sintering and copper infiltration

The as-printed samples are sintered and copper infiltrated in a laboratory electric tubular furnace (59256-P-COM, Lindberg) using a ceramic substrate. A gas mixture of 2.5% H_2/ 97.5% Ar (flow rate=5 ft^2/h) is circulated inside the quartz tube to prevent the oxidation of the samples. The temperature profiles used during the sintering and copper infiltration are provided in Figure 4.S4.

4.3.4 Porosity analysis

Each sintered and copper infiltrated scaffold is sealed in a resin (EpoFix Resin, Struers) block before polishing. The scaffold is polished until reaching 0.2H, 0.5H and 0.8H of the printed structure. The polished cross sections are observed under an optical microscope (Zeiss Axioplan EL-Einsatz). For each cross section, five images are taken at different areas of the cross section and analyzed by an image analyzing software (Clemex, ST-2000). The porosity is calculated as the ratio of voids area over the filament area in the polished cross sections.

4.3.5 Tensile tests

The tensile bars are printed with 95 wt.% ink and 250 μm tapered nozzle, of which the average size of the cross section of the narrow part is ~4.0 × 1.8 mm. The filaments oriented 0°/90° to the tensile direction, i.e. the filaments from same layer are parallel, while adjacent layers are orthogonal. The tensile tests are carried out on a MTS Insight machine with a 50 kN load cell (MTS 569332-01) at a crosshead speed of 1 mm/min and using an extensometer (MTS 632.26, C-20). Three specimens for each sample type are tested.

4.3.6 Electrical conductivity test

The test samples used for the electrical conductivity measurements are sintered and copper infiltrated rods having typical dimensions of 30×1×1 mm. They are printed with the 95 wt.% ink and the 250 μm tapered nozzle. The current values of 1 A, 2 A and 3 A is provided by an EMS 150-33-D-RSTL power supply. A NI 6211 device is employed for the current and voltage acquisition. The control of the power supply and the logging of test data are carried out via a LabVIEW program. Three specimens of each sample type were tested.

4.4 Conclusions

In summary, the fabrication of fully-dense 3D metallic structures consisting of the solvent-cast 3D printing and the following heat-treatments is developed. The Young's modulus of fabricated structures is up to 195 GPa and approaches typical values for similar bulk material while the conductivity is 1.62×10^6 S/m, which are superior to the structures fabricated by most commercial 3D printing techniques.[41-43] This facile technique enables lower-cost 3D printing of high-performance metallic parts compared to SLS and SLM. Various complex 3D structures, including porous, interlocked and overhung structures, can be fabricated. Furthermore, we envision that diverse metallic material such as titanium, silver, copper and zinc, could be employed in this technique. The approach can be applied to fabricate small sized devices (e.g. the artificial bones for human) in the medical field, benefiting from its high resolution and ability to fabricate complex microstructures with desirable mechanical properties. In addition, the method is also suitable to fabricate conductive porous microstructures serving as electromagnetic shields in the microwave field.

Acknowledgement

The authors acknowledge the financial support from NSERC (Natural Sciences and Engineering Research Council of Canada, grant number: RGPIN 312568-2013) and Auto 21 of the Canadian Network of Centers of Excellence (NCE) program. A scholarship for Mr. Xu was also provided by the China scholarship Council (CSC) and the Fonds de recherche du Quebec - Nature et technologies (FRQNT).

References

1 M. Elahinia, N. S. Moghaddam, M. T. Andani, A. Amerinatanzi, B. A. Bimber, R. F. Hamilton, *Prog. Mater. Sci.*, 2016, **83**, 630-663.

2 D. Hong, D. T. Chou, O. I. Velikokhatnyi, A. Roy, B. Lee, I. Swink, I. Issaev, H. A. Kuhn, P. N. Kumta, *Acta Biomater.*, 2016, **45**, 375-386.

3 S. Dadbakhsh, M. Speirs, H. J. Van, J. P. Kruth, *MRS Bull.*, 2016, **41**(10), 765-774.

4 J. Hu, M. F. Yu, *Science*, 2010, **329**(5989), 313-316.

5 C. Ladd, J. H. So, J. Muth, M. D. Dickey, *Adv Mater*, 2013, **25**(36), 5081-5085.

6 Y. S. Rim, S. H. Bae, H. Chen, N. De Marco, Y. Yang, *Adv Mater*, 2016, DOI: 10.1002/adma.201505118

7 B. Y. Ahn, E. B. Duoss, M. J. Motala, X. Guo, S. I. Park, Y. Xiong, J. Yoon, R. G. Nuzzo, J. A. Rogers, J. A. Lewis, *Science*, 2009, **323**(5921), 1590-1593.

8 J. Lessing, A. C. Glavan, S. B. Walker, C. Keplinger, J. A. Lewis, G. M. Whitesides, *Adv. Mater.*, 2014, **26**(27), 4677-4682.

9 M. G. Mohammed, R. Kramer, *Adv. Mater.*, 2017, **29**(19), DOI: 10.1002/adma.201604965

10 L. Thijs, K. Kempen, J. P. Kruth, J. Van Humbeeck, *Acta Mater.*, 2013, **61**(5), 1809-1819.

11 S. Hong, J. Yeo, G. Kim, D. Kim, H. Lee, J. Kwon, H. Lee, P. Lee, S. H. Ko, *ACS Nano*, 2013, **7**(6), 5024-5031.

12 D. D. Gu, W. Meiners, K. Wissenbach, R. Poprawe, *Int. Mater. Rev.*, 2012, **57**(3), 133-164.

13 L. Thijs, F. Verhaeghe, T. Craeghs, J. Van Humbeeck, J. P. Kruth, *Acta Mater.*, 2010, **58**(9), 3303-3312.

14 D. Gu, Y. C. Hagedorn, W. Meiners, G. Meng, R. J. S. Batista, K. Wissenbach, R. Poprawe, *Acta Mater.*, 2012, **60**(9), 3849-3860.

15 S. Van Bael, Y. C. Chai, S. Truscello, M. Moesen, G. Kerckhofs, H. Van Oosterwyck, J. P. Kruth, J. Schrooten, *Acta Biomater.*, 2012, **8**(7), 2824-2834.

16 K. McAleal, Materials and applications for the SLS selective laser sintering process. *Proceedings of the 7th International Conference on Rapid Prototyping,* **1997**, pp 23-33

17 V. Seyda, N. Kaufmann, C. Emmelmann, *Phys. Procedia*, 2012, **39**, 425-431.

18 H. Gong, K. Rafi, H. Gu, G. J. Ram, T. Starr, B. Stucker, *Mater. Des.*, 2015, **86**, 545-554.

19 E. O. T. Olakanmi, R. F. Cochrane, K. W. Dalgarno, *Mater. Sci.*, 2015, **74**, 401-477.

20 J. A. Lewis, G. M. Gratson, *Mater. Today*, 2004, **7**(7), 32-39.

21 D. Therriault, S. R. White, J. A. Lewis, *Nat. Mater.*, 2003, **2**(4), 265-271.

22 D. Therriault, R. F. Shepherd, S. R. White, J. A. Lewis, *Adv. Mater.*, 2005, **17**(4), 395-399.

23 S. Z. Guo, F. Gosselin, N. Guerin, A. M. Lanouette, M. C. Heuzey, D. Therriault, *Small*, 2013, **9**(24), 4118-4122.

24 K. Chizari, M. A. Daoud, A. R. Ravindran, D. Therriault, *Small,* 2016, **12**(44), 6076-6082.

25 S. Z. Guo, M. C. Heuzey, D. Therriault, *Langmuir*, 2014, **30**(4), 1142-1150.

26 S. Bodkhe, G. Turcot, F. P. Gosselin, D. Therriault, *ACS Appl. Mater. Interfaces*, 2017, DOI: 10.1021/acsami.7b04095

27 G. Postiglione, G. Natale, G. Griffini, M. Levi, S. Turri, *Composites, Part A*, 2015, **76**, 110-114.

28 B. G. Compton, J. A. Lewis, *Adv. Mater.*, 2014, **26**(34), 5930-5935.

29 B. Y. Ahn, D. Shoji, C. J. Hansen, E. Hong, D. C. Dunand, J. A. Lewis, *Adv. Mater.*, 2010, **22**(20), 2251-2254.

30 W. J. Hyun, S. Lim, B. Y. Ahn, J. A. Lewis, C. D. Frisbie, L. F. Francis, *ACS Appl. Mater. Interfaces*, 2015, **7**(23), 12619-12624.

31 E. Hong, B. Y. Ahn, D. Shoji, J. A. Lewis, D. C. Dunand, *Adv. Eng. Mater.*, 2011, **13**(12), 1122-1127.

32 M. A. Skylar-Scott, S. Gunasekaran, J. A. Lewis, *Proc. Natl. Acad. Sci.*, 2016, 201525131.

33 L. L. Lebel, B. Aissa, M. A. E. Khakani, D. Therriault, *Adv. Mater.*, 2010, **22**(5), 592-596.

34 I. W. Chen, X. H. Wang, *Nature*, 2000, **404**(6774), 168-171.

35 P. Beaulieu, Ph.D Thesis, Polytechnique Montreal, 2012

36 K. I. Winey, R. A. Vaia, *MRS bull.*, 2007, **32**(04), 314-322.

37 L. Francis, Aerial view of the Montreal's Olympic stadium, http://francislepine.photoshelter.com/image/I00005iyrD3WYZ28, (accessed May 2017)

38 D. Peckner, Handbook of stainless steels.**1977**

39 J. R. Davis, K. M. Mills, S. R. Lampman, Metals handbook. Vol. 1. Properties and selection: Irons, steels, and high-performance alloys. *ASM International, Materials Park, Ohio 44073, USA*, **1990**, *1063.*

40 R. G. P. I. Molding, I. Pressing, Metal Powder Industries Federation, Princeton, NJ, 1990, 3-22.

41 M. M. Dewidar, K. A. Khalil, J. K. Lim, *Trans. Nonferrous Met. Soc. China*, 2007, **17**(3), 468-473.

42 M. M. Dewidar, K. W. Dalgarno, C. S. Wright, *Proc. Inst. Mech. Eng., Part B*, 2003, **217**(12), 1651-1663.

43 K. Kempen, E. Yasa, L. Thijs, J. P. Kruth, J. Van Humbeeck, *Phys. Procedia*, 2011, **12**, 255-263.

4.5 Supporting Information

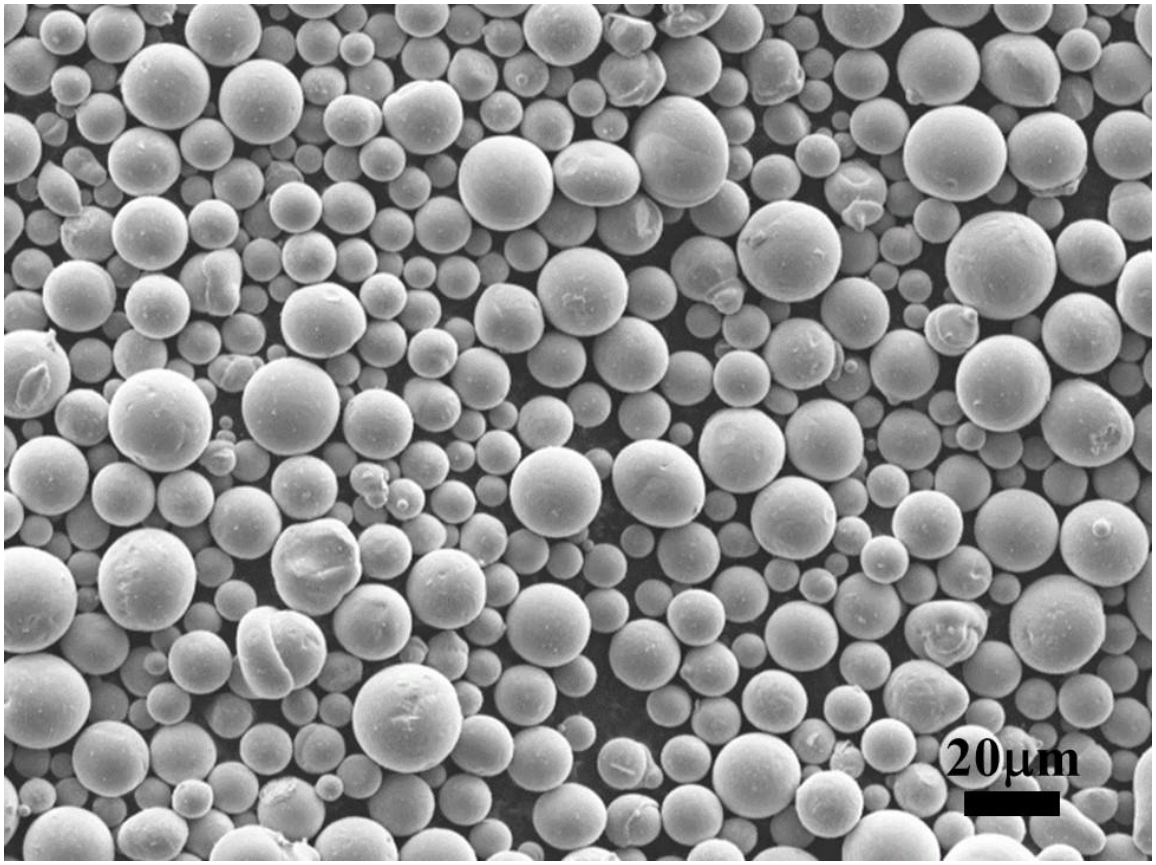

Figure 4.6 Secondary electron micrograph of HAS powder particles (≤ 20 μm).

Table 4.1 Ink formulations created for 3D printing

Ink constituent	**85 wt.% (47 vol.%) HAS/PLA ink [g]**	**90 wt.% (59 vol.%) HAS/PLA ink [g]**	**95 wt.% (75 vol.%) HAS/PLA ink [g]**	**98 wt.% (90 vol.%) HAS/PLA ink [g]**
PLA	15	10	5	2
DCM	60	40	20	18
HAS microparticles	85	90	95	98

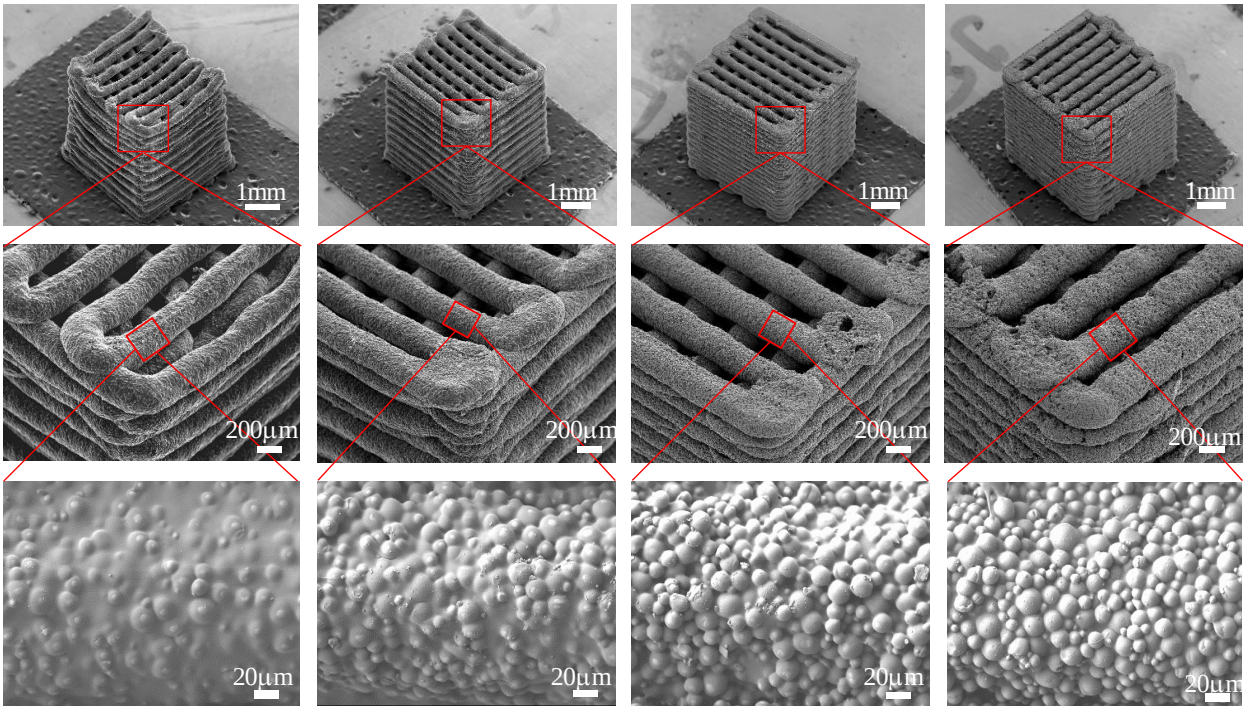

Figure 4.7 SEM images of as-printed 20-layers scaffolds of different concentrated inks (85, 90, 95, 98 wt.%) (first row from left to right) and their close-up view images (middle and bottom rows). The HAS microparticles are covered and bonded by the polymer. The filaments of all four scaffolds align well. However, the 85 wt.% scaffold distorts and the surface of the 98 wt.% scaffold is rough.

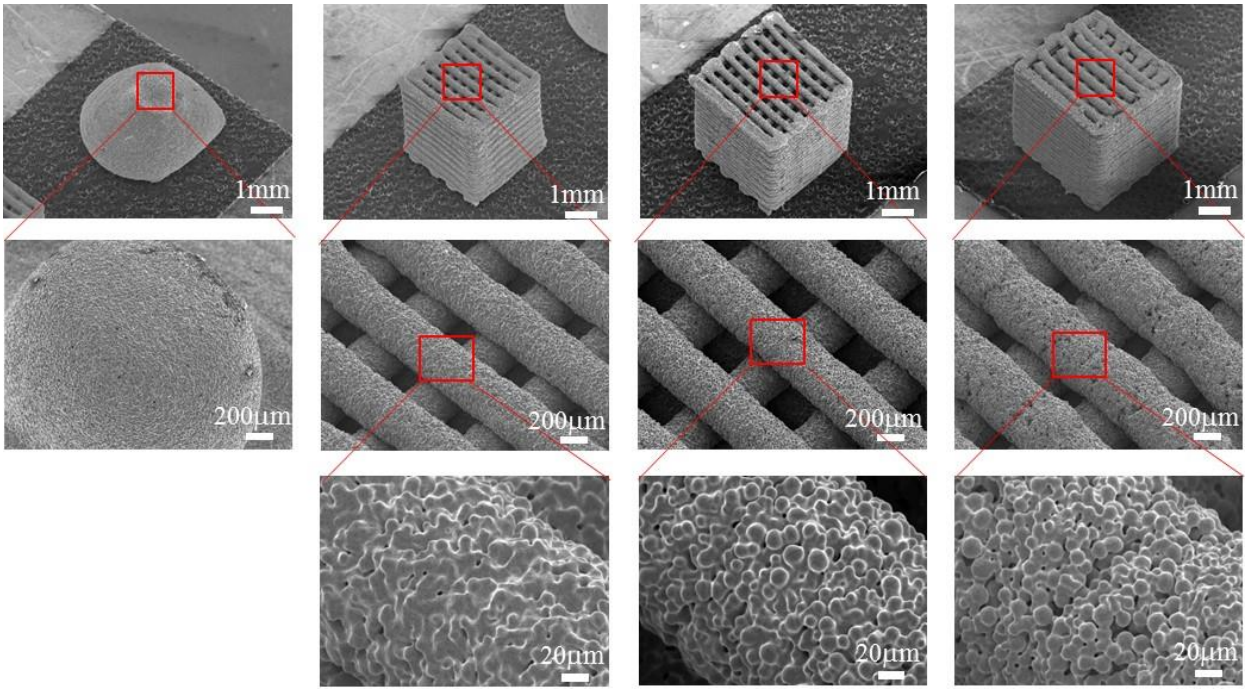

Figure 4.8 SEM images of sintered 20-layers scaffolds of different concentrated inks (85, 90, 95, 98 wt.%) (first row from left to right) and their close-up view images (middle and bottom rows). After sintering, the polymer is burned away and the HAS microparticles are sintered together. The filaments of 90, 95 and 98 wt.% scaffold keep their shapes and align well, while the 85 wt.% ink printed scaffold collapses during sintering and the surface of 98 wt.% scaffold is rough.

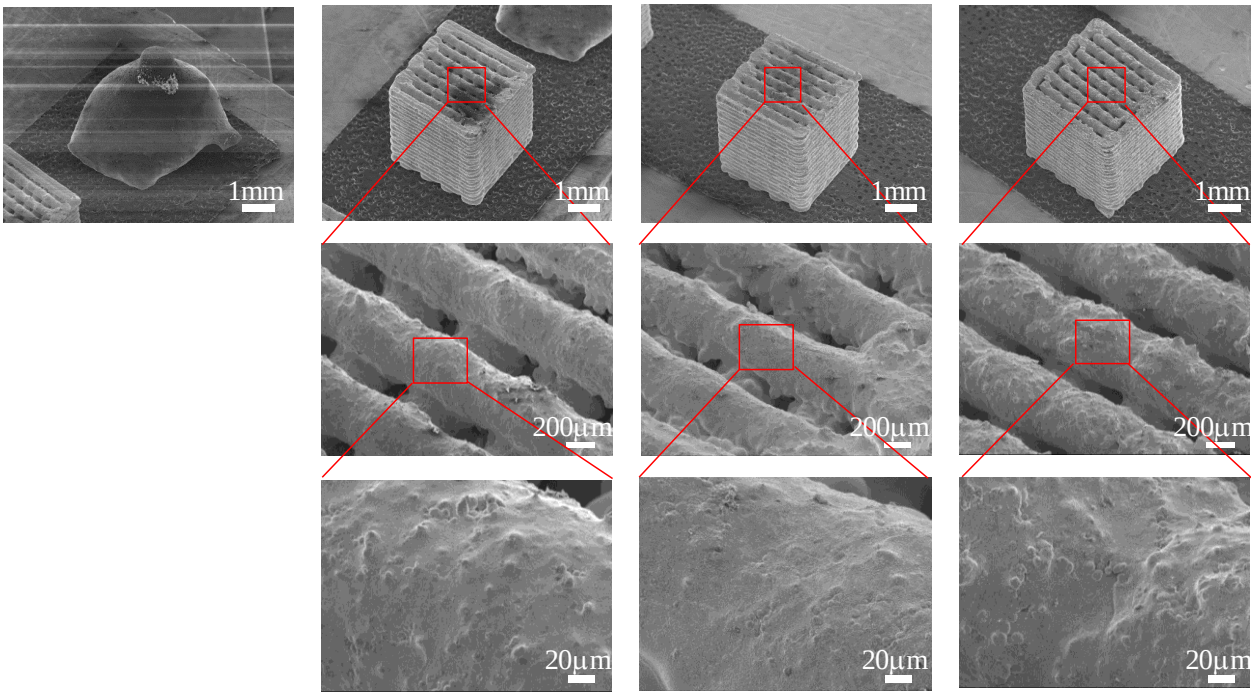

Figure 4.9 SEM images of copper infiltrated 20-layers scaffolds of different concentrated inks (90, 95, 98 wt.%) (first row from left to right) and their close-up view images (middle and bottom rows). Melted copper infiltrated into the sintered filaments. Some excessed copper is left on the top of the scaffold.

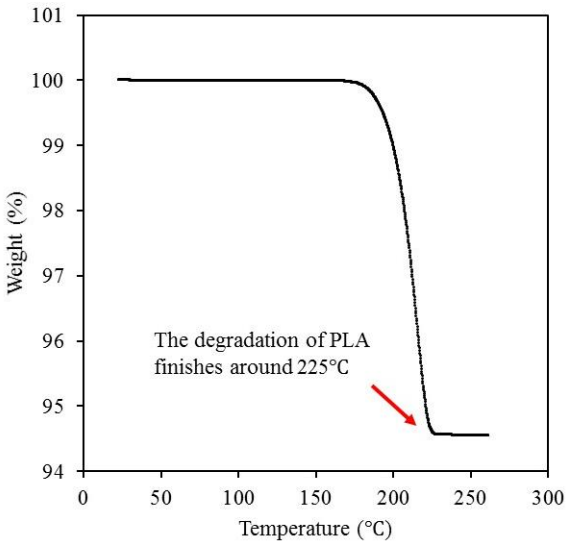

Figure 4.10 TGA results of 95 wt.% HAS/PLA scaffold. The temperature is raised from 20 ℃ to 500 ℃ at a rate of 1 ℃/min (the same heating rate as the sintering process). The degradation of PLA finishes before 225 ℃.

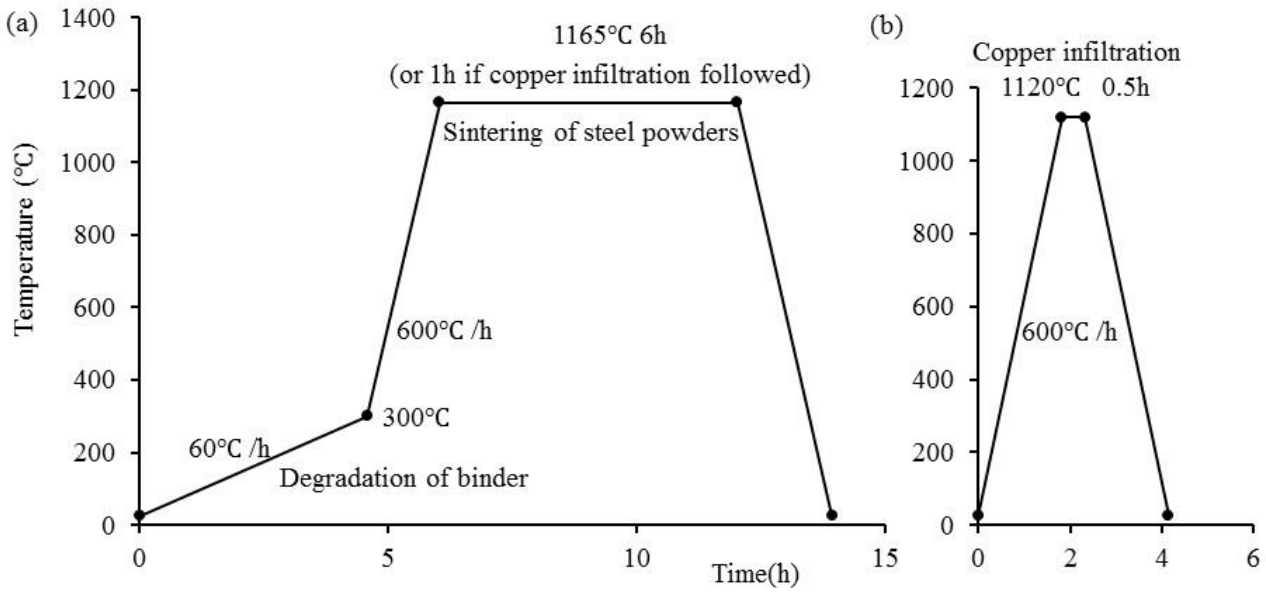

Figure 4.11 Temperature profiles using during sintering and copper infiltration. Debinding starts from 25 ℃ to 300 ℃ with a heating rate of 60 ℃/h. Then the temperature is raised up to 1165 ℃ with a heating rate of 600 ℃/h and held at 1165 ℃ for 6h for sintering. For copper infiltration, the temperature is raised up to 1120 ℃ and held for 0.5 h, then cooled down to the room temperature.

Table 4.2 Porosity analysis results of 90, 95 and 98 wt.% sintered (6h) and copper infiltrated 20-layer scaffolds.

Porosity	**90 wt.%**	**95 wt.%**	**98 wt.%**
Sintered	10.4 % ± 4.4 %	12.1 % ± 5.3 %	12.4 % ± 2.0 %
Copper infiltration	0.3 % ± 0.3 %	0.2 % ± 0.1 %	0.2 % ± 0.2 %

Table 4.3 Tensile test results of 95 wt.% as-printed, sintered and copper infiltrated tensile bars compared with: (1) Wrought stainless steel[38], (2) Nitrogen alloyed, high strength, medium elongation, sintered at 1290 °C (2350 °F) in dissociated ammonia[39], (3) PM steel containing 0.8% carbon and 2% copper[39], and (4) Copper infiltrated steel containing 0.8% carbon[39].

	E [GPa]	**UTS [MPa]**	**Elongation [%]**
As-printed sample	3.1 ± 0.3	28.0 ± 3.0	1.45 ± 0.10
Sintered sample	196 ± 16	485 ± 70	0.47 ± 0.06
Copper infiltrated sample	195 ± 16	511 ± 57	0.77 ± 0.07
Wrought stainless steel: SS-316 (1)	193	515	30
PM steel stainless steel: SS-316N2-38 (2)	140	480	13
PM steel FC-0208-60 (3)	155	520	< 1
Cu infiltrated PM steel: FX-2008-60 (4)	145	550	1

Video 4.1 3D printing of an 8-layers tensile bars with 95 wt.% ink and 250 μm tapered nozzle at a speed of 10 mm/s. http://www.rsc.org/suppdata/c7/tc/c7tc02884a/c7tc02884a2.mov

CHAPTER 5 ARTICLE 2: ENVIRONMENT-FRIENDLY AND REUSABLE INK FOR 3D PRINTING OF METALLIC STRUCTURES

Published in *Materials and Design*, Vol. 160, **2018**, 262-269.

By

Chao Xu, Qinghua Wu, Gilles L'Espérance, Louis Laberge Lebel and Daniel Therriault*

ABSTRACT

There is an increasing need for 3D printing of metallic structures in a green and cost-effective way. Here, an environment-friendly and reusable metallic ink was developed for an economical metal 3D printing method. The metallic ink is composed of steel micro powders, a biodegradable polymer: chitosan, acetic acid and deionized water. The metal 3D printing method consists of: (i) 3D printing of metallic structures using the metallic ink at room temperature, (ii) thermal treatments on the as-printed structures that decompose the polymer binder and sinter the steel powders, and (iii) an optional step: infiltrating melted copper into the sintered structures to achieve fully dense metal/metal hybrid structures. We demonstrate that any incorrectly built as-printed structures and scrap materials can be recycled and reused for 3D printing by dissolving them again in acetic acid. The fabricated structures feature a low filament porosity of 1.0% which enables high properties such as an electrical conductivity of 1.3 × 106 S/m and a Young's modulus of 160 GPa. The metallic ink can be used for the 3D printing of high performance metallic structures while demonstrating a low environmental impact and a very effective utilization of metallic materials.

5.1 Introduction

Additive manufacturing (AM) technologies, which build 3D structures layer-by-layer, provide a cost-effective alternative to create diverse metallic structures.[1-3] 3D printed metallic structures are used in a broad range of applications such as artificial bones as implants[4-6], sensors[7,8], microelectronics[9,10], and batteries for energy storage[11,12]. The most commonly used commercial manufacturing technologies are powder-bed approaches such

as selective laser sintering/melting (SLS/SLM) and electron beam melting (EBM) according to the fusion mechanism and energy source. In these technologies, fine micro scale metal powders are tightly compacted to form a powder bed. A high-intensity laser or electron beam selectively scans the powder particles to fuse them layer-by-layer.[13] Once completed, the fused part is removed from the powder bed and thoroughly cleaned by removing the loose or partially sintered powders. The nature of the powder bed methods prevents themselves from manufacturing various architectures such as enclosed and fine porous structures. The high power intensity laser system can be expensive and a safety hazard. Moreover, the repeated high-intensity scanning beam can cause the loss of alloying elements, a dramatic change in temperature (which can lead to metallurgy defects and residual stresses) and excessive oxidation.[14-16]

Researchers attempted to address the shortcomings of the powder bed processes with direct energy deposition (DED), where a focused energy beam is utilized to fuse the metallic materials as they are being deposited. Skylar-Scott *et al*. sintered water-based silver inks using a focused laser as they were being extruded from the nozzle.[17] High resolution and freeform 3D metallic structures were manufactured using this technique. However, this method was compatible with only a narrow range of low melting point metals such as silver. Although the mechanical properties were not reported in [17], given that water evaporation and the sintering of silver powders had to be accomplished within the limited time of laser scanning, the incomplete sintering might lead to poor mechanical properties of the final product. Furthermore, since this was a laser assisted process, it still suffered from the common laser induced limitations, like excessive oxidation and the loss of alloying elements.

Solvent-cast 3D printing (SC-3DP) consists of an ink paste containing metal powders, polymer and volatile solvent, in which no lasers or power beds are required.[18] The metallic ink is extruded through a micro nozzle under an applied pressure. The volatile solvent evaporates rapidly upon extrusion as a result of the pressure drop. The polymer solidifies and the rigidity of the extruded ink filament increases, which allows it to hold its shape and support the subsequent layers.[18] The result is a metal/polymer composite 3D structure. It is transformed into a metal structure through subsequent thermal treatments where the polymer is thermally decomposed and the metal powders are sintered. Xu *et al*.

demonstrated the method using a metallic ink comprised of steel powders, polylactic acid (PLA) and dichloromethane (DCM), to create steel 3D structures.[19] Various structures were printed and they exhibited high mechanical and electrical performances, which were comparable with bulk materials. Jakus *et al.* reported the fabrication of metallic 3D structures employing metal oxides (i.e. Fe_2O_3, NiO and CuO) as the metal precursors.[12] The metal oxides were thermochemically reduced into sintered metal 3D structures in a reducing atmosphere of H_2. Although these processes are useful, like the majority of the SC-3DP approaches, the toxic and volatile DCM is used as the organic solvent. As a result, those processes have to be performed under a ventilation device because the toxic solvent can be harmful to the operator and the environment. Peng *et al*. introduced a water-based polymer solution to prepare metallic inks for SC-3DP, which is comprised of deionized water, polyvinyl alcohol (PVA) binder and polyethylene glycol (PEG) plasticiser.[20] Ferrite magnetic structures were fabricated by SC-3DP following by a series of thermal treatments. However, the printed structures have a low resolution of 0.41 mm with important shape deformation. As the volatility of the solvent and the pressure drop upon extrusion are the only triggers of solvent evaporation, the relatively long solidification time results in excessive sagging and deformation of the ink filament.

Driven by the aforesaid challenges, we developed an environment-friendly and reusable metallic ink compatible with the SC-3DP approach and subsequent thermal treatments (see Figure 5.1). Highly alloyed steel (HAS) powders are uniformly mixed with a water-based polymer solution using a ball mill machine. The metallic paste, referred to the ink, is loaded into a syringe barrel and extruded through a tapered micro nozzle under a specific pressure at room temperature. A fan blows air over the extruded ink filament to accelerate solvent evaporation during the extrusion. The ink filament is then deposited using a 3-axis robot at the specific coordinates according to the CAD model to create a 3D object. The as-printed sample is a hybrid metal/polymer 3D structure. After the part is left to dry at ambient conditions for four hours, it is thermally treated in an atmosphere containing Ar and H_2. The final product is a metal structure where the filament porosity can be tailored by the sintering duration.[20] A fully dense metallic structure is obtained by a copper infiltration process where the melted copper fills the pores inside the sintered filaments driven by capillary forces.

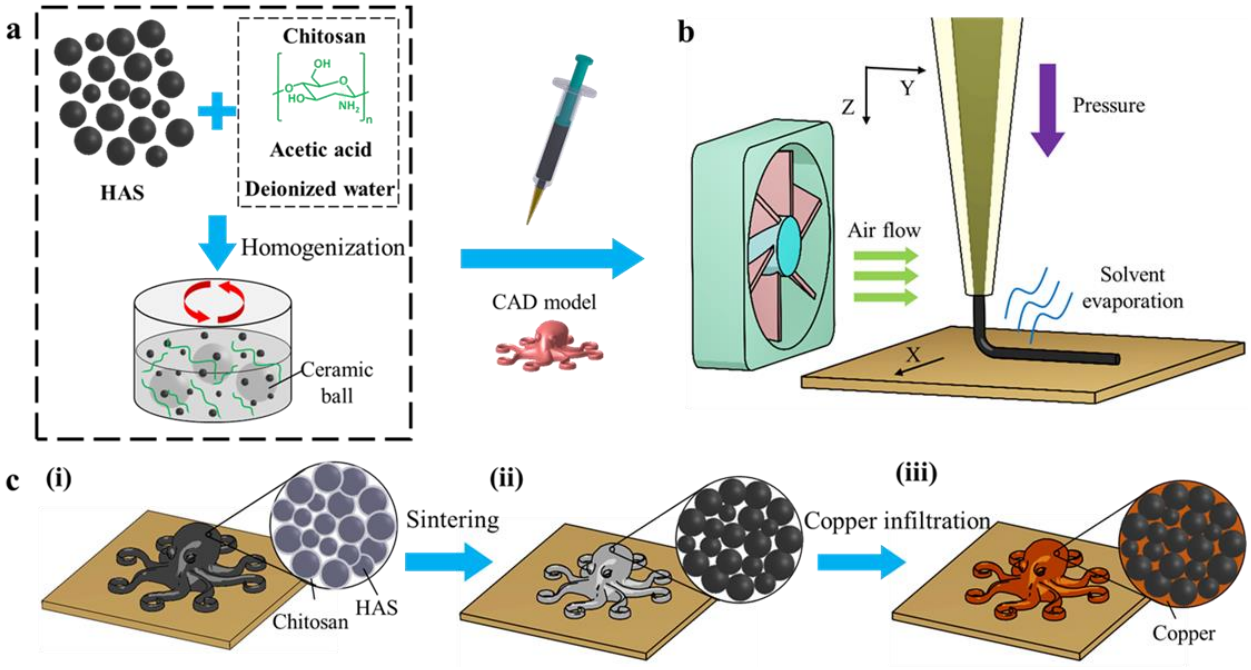

Figure 5.1 Schematic of the fabrication process of a 3D metallic structure combining the following steps. (a) Metallic ink preparation: HAS powders are mixed with chitosan/acetic acid solution using a ball mill machine. (b) Solvent-cast 3D printing: the metallic ink is loaded in a syringe and extruded through a micro nozzle under a certain pressure at room temperature. The solvent content evaporates upon extrusion assisted by the flow of air. (c) Subsequent thermal treatments under Ar/H_2: (i) the dried as-printed sample is thermally treated in a furnace. (ii) The polymer is thermally decomposed and the HAS powders are sintered. (iii) After sintering, the sintered sample is infiltrated with melted copper, which fills the pores in the sintered filaments driven mainly by capillary forces.

5.2 Experimental section

5.2.1 Ink preparation

Chitosan is dissolved in an acetic acid water solution (80 vol.% acetic acid and 20 vol.% deionized water). The chitosan is 90% deacetylated with an average molecular weight of 207 kDa, from Biolog in Germany. The acetic acid is purchased from Sigma-Aldrich and used as received. The chitosan solution is mixed using a ball mill mixer (8000M mixer/Mill, SPEX samplePrep) for 10 min. After mixing, it is sealed and stored in the fridge. The

metallic ink is prepared by mixing HAS powders and chitosan solution using the ball mill for 5 min.

5.2.2 3D printing

3D printing is performed using a computer-controlled 3-axis positioning robot (I&J2200-4, I&J Fisnar) and a pressure dispensing system (HP-7X, EFD). The metallic ink is loaded into a syringe (3 mL, Nordson EFD) attached with a smooth-flow tapered nozzle (exit inner diameter = 250 μm). The structures are printed on a glass slide (PN 16004-422, VWR) with a thin layer of petroleum jelly (VSL-32600) as releasing agent. All the structures in this work are printed at a linear printing speed of 7 mm/s and under a pressure around 0.7 MPa, with an airflow system (a computer cooling fan, DC 12V, 0.44A, 20 cm from the deposition nozzle). The layer height is 200 μm, 80% of the nozzle inner diameter. The layer thickness compensates the filament reduction induced by solvent evaporation and guarantees secure, tight bonding between neighboring layers. The CAD models are either designed by a CAD software (CATIA) or downloaded from internet (thingiverse.com). They are sliced into several layers and interpreted into G-code by a slicing software (Simplify3D). Then the G-code is converted into a point-to-point program that can be read by the JR Points software to control the positioning robot.

5.2.3 Thermal treatments

The as-printed samples are thermally treated in a laboratory electric tubular furnace (59256-P-COM, Lindberg) on a ceramic substrate. The samples are prevented from oxidation by a circulated gas flow (97.5% Ar and 2.5% H_2, flow rate = 2 L/min) inside the quartz tube. The samples are heated to 400 °C at a rate of 60 °C/h, held for 1h for debinding, and then heated to 1165 °C at a rate of 600 °C/h, held for 3h for sintering. If needed, the sintered samples are then copper infiltrated at 1120 °C for 1h at a heating rate of 600 °C/h by placing a piece of infiltrating copper on the top. The amount of the copper is determined by the filament porosity and filament volume.

5.2.4 Porosity analysis

The sintered and copper infiltrated scaffolds are sealed in a resin (EpoFix resin, Struers) block. The resin block is polished until the horizontal cross section is visible. The cross section is observed in an optical microscope (Zeiss Axioplan EL-Einsatz) and the amount of porosity is determined by

an image analysis software (Clemex, ST-2000). The filament porosity is calculated as the ratio of void area inside the filament over the filament area. Ten cross sections of each sample are analysed.

5.2.5 Electrical conductivity measurement

The electrical conductivities of the sintered and copper infiltrated samples are measured using four-point probes method. The devices, circuit diagram and representative sample are shown in Figure 5.S4. A constant voltage of 0.1 V is provided by a power supply (Agilent, E3633A). The current and voltage are acquired by two multimeters (HP, 3457A). Five specimens of each sample type are tested.

5.2.6 Tensile test

The samples are sintered and copper infiltrated tensile bars, of which the cross section of the neck is ≈ 3.6 × 1.6 mm. The tensile tests are carried out on a MTS Insight machine with a 50 kN load cell (MTS 569332-01) at a crosshead speed of 1 mm/min and using an extensometer (gauge length = 8 mm, MTS 632.26, C-20). Five specimens for each sample type are tested.

5.3 Results and Discussion

The metallic material is a highly alloyed steel (HAS) micro powder with a spherical shape and a diameter less than 20 μm, which is the same powder as previously described in [19]. The spherical shape and the relatively small size can enable low frictional forces between the micro powders and prevent the metallic ink from clogging the micro nozzle. Chitosan, a biocompatible polymer, can be dissolved in an acidic solution. Its solution was previously used to 3D print microstructures for guided cell growth.[21] Acetic acid is a volatile, organic, weak acid. Chitosan can be dissolved in an acetic acid water solution as a viscous hydrogel. Acetic acid is bio-compatible and evaporates rapidly in ambient conditions. Those features make chitosan/acetic acid a great candidate as a binder system for metal 3D printing.

0.8g chitosan is dissolved in 10 mL 80 vol.% acetic acid/deionized water. The chitosan/acid solution is mixed with HAS powders at a weight ratio of 1:6.5. The detailed ink composition is summarized in Table 5.1. In unpublished results, the addition of excessive polymer binder results in incomplete dissolution. Part of the chitosan remains solid, which causes clogging of the micro nozzle. On the other hand, insufficient amounts of polymer binder leads to brittle as-printed

samples. The amount of deionized water is also an important parameter. Excessive water can increase the duration of solidification and result in sagging and shape deformation of the extruded ink filament mostly due to the slower evaporation rate of water compared to acetic acid. Nevertheless, insufficient water prevents the ionization of hydrogen ions from acetic acid, which can cause the incomplete dissolution of polymer.

Table 5.1 Metallic ink composition for accurate printing

Constituent	Density (g/ml)	Mass fraction	Volume fraction
Chitosan	1.4*	1.0%	2.9%
Acetic acid	1.05	10.0%	40.8%
Deionized water	1	2.4%	10.2%
HAS powders	8.05	86.7%	46.1%
Total	4.28	100.0%	100.0%

*The density of chitosan is the apparent density of chitosan in the as-printed sample.

The metallic ink is printed while a fan is blowing air on the ink filament upon extrusion. As the air flow speed on the surface of the extruded ink filament is increased, the solvent evaporation is expedited and the solidification time of the extruded ink filament is shortened. The airflow setup, the influence of the airflow on the solvent evaporation speed and the printing quality are shown in Figure 5.S1 and Video 5.S1. The solvent evaporation speed is investigated by weighing the extruded ink filaments printed with and without the airflow. Half of the solvent content (acetic acid and deionized water) evaporates within 2.8 minutes after extrusion without airflow. On the other hand, it only takes 1.1 minutes assisted by the airflow, which improves the solvent evaporation speed by 255%. Due to the short solidification time, the ink filament does not sag, flow or merge with neighboring filaments. By comparing the printing process and the as-printed scaffolds, it is clearly observed that the one printed with airflow assistance proves to be more reliable. The one printed without airflow, however, has merged filaments and loses its shape. To ensure the printing

quality, all the structures in this work are printed with a tapered nozzle (tip inner diameter: 250 μm) at a linear printing speed of 7 mm/s with the airflow assisted.

During printing the samples, it was difficult to release the sample from the substrate. For the releasing purpose, a thin layer of Petroleum jelly is applied on the substrate prior to printing. Once the printing is completed, the sample along with the substrate is placed in a vacuum oven at 50 °C for 2 h. The petroleum jelly melts and acts as a lubrication between the bottom of the sample and the substrate. The sample can be easily released from the substrate. After drying in the vacuum oven, the diameter of the filament is around 220 μm, which is 88% of the nozzle inner diameter. Figure 5.2a-e shows scanning electron microscope (SEM) images of a dried as-printed scaffold, including the structure, the filament and the HAS micro particles. The images of the as-printed samples demonstrate the versatility of our 3D printing method to fabricate well-organized structures from the metallic ink. The structure is qualitatively ordered (Figure 5.2a). The filaments from neighboring layers are perpendicularly stacked without shape deformation (Figure 5.2b). As the metal content is up to 94.1 vol.% in the dried as-printed sample, the filament is comprised of mainly HAS powders covered and bound by a thin layer of chitosan (Figure 5.2c-d). There are small fragments ($\approx$ 0.5 μm) randomly distributed on the surface of the HAS particle (Figure 5.2e). The HAS particle retains its spherical shape without visible chemical corrosion induced pits on the surface. To investigate the composition of the small fragments, an energy dispersive X-ray spectroscopy analysis (EDS) is carried out on the HAS particle (Figure 5.2f). The small fragments on the HAS particle surface contain more carbon and oxygen compared to the rest of the area on the HAS particle surface. It suggests that they should be the aggregates of the precipitated chitosan after the solvent evaporates. As a result, although the metallic ink contains metal powders and weak acid, it is chemically stable at room conditions.

The 3D structures printed from the metallic ink are reusable (Figure 5.S2). Any incorrectly printed structures and scrap materials can be dissolved in the acid solvent in a proportion according to the ink recipe (Table 5.1) and then mixed using the ball mill. After homogenization, the recycled metallic ink can be reused for 3D printing. In addition, the manufacturing efficiency can be improved by using multiple print-heads (including a pressure dispensing system, syringe holder, syringe and micro nozzle) (Video 5.S2). By adjusting the nozzle tips to the same height, multiple

copies of the structures can be printed at the same time. If different inks are loaded in different syringe, multiple copies of the structures made in different materials can be printed at one time.

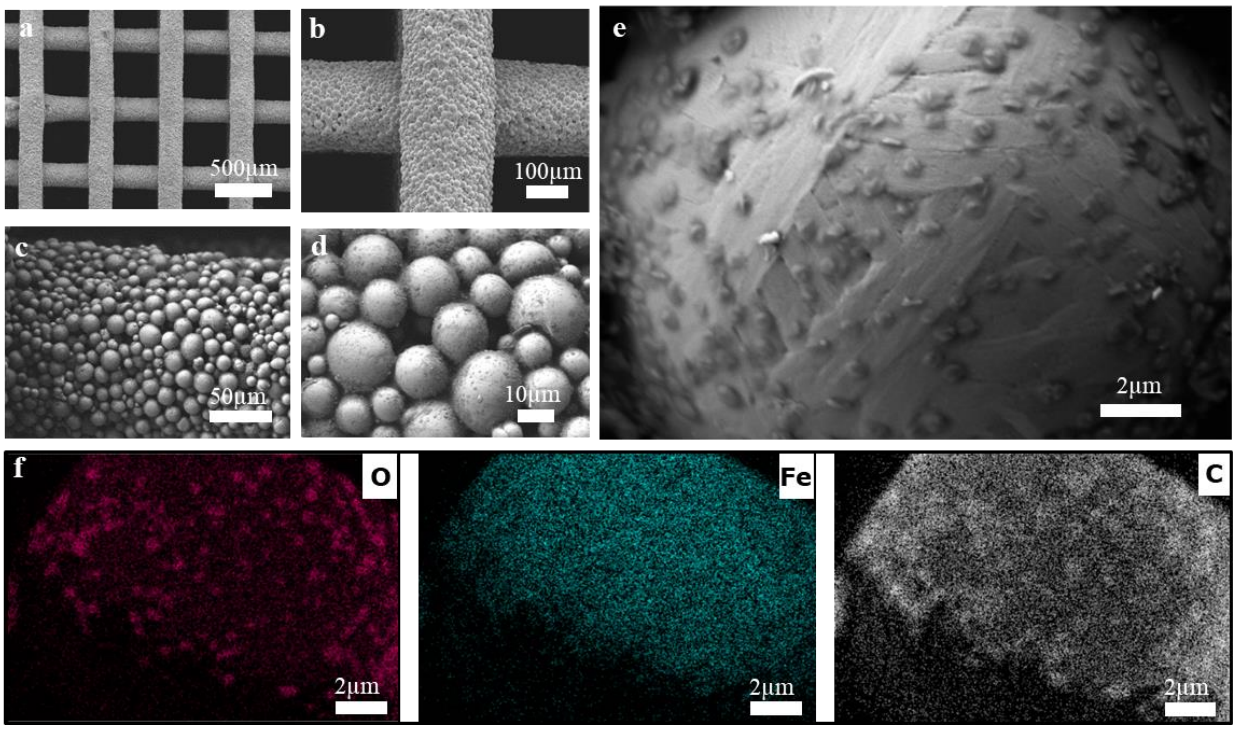

Figure 5.2 Scanning Electron Microscopy (SEM) images of as-printed scaffolds (tapered nozzle: 250µm in diameter) at different magnifications: (a), (b), (c), (d) and (e), and (f) Energy Dispersive X-ray Spectroscopy (EDS) results of oxygen, iron and carbon on a signal HAS particle of the dried as-printed scaffold.

To determine the temperature profile of the thermal treatments, the decomposition temperatures of the polymer binders are investigated by conducting thermal gravity analysis (TGA) in a nitrogen atmosphere (Figure 5.3a). The commonly used polymer binder, PLA, degrades below 400 °C. Chitosan loses 10% of its weight under 100 °C due to loss of moisture. It partially decomposes at around 300 °C where the weight drops by another 40%. Then the decomposition speed slows down and around 30 % of the weight is left until 800 °C. It coincides with the results reported by the previous researcher.[22] The residues (Figure 5.3b) contains mainly carbon according to the elemental test result. The carbon can diffuse into the HAS powders during the thermal treatments, hardening the sintered steel.[23] The petroleum jelly, which acts as the releasing agent, completely decomposes at around 400 °C. Figure 5.3b shows the sintering temperature profile which consists

of a polymer debinding plateau at 400 °C for 1h and a metal sintering plateau at 1165 °C for 3h. An optional copper infiltration can be conducted on the sintered structures at 1120 °C for 1h (Figure 5.3c). Figure 5.3d shows the as-printed, sintered and copper infiltrated scaffolds thermally treated following this temperature profile.

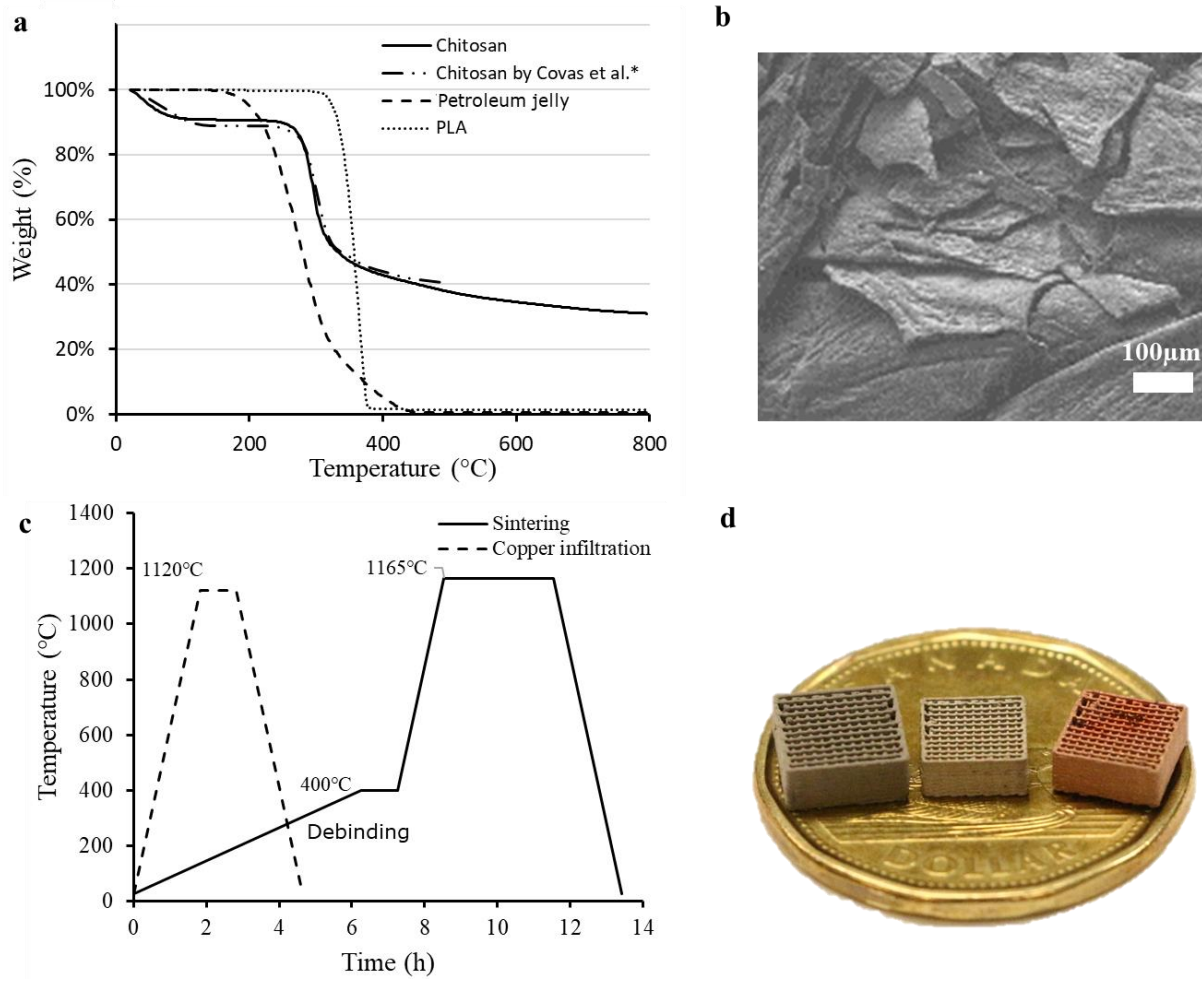

Figure 5.3 (a) TGA results of chitosan[22], PLA and petroleum jelly in nitrogen up to 800 °C, (b) the SEM image of the chitosan thermal decomposition residues, (c) temperature profiles of the thermal treatment processes, and (d) the optical image of the as-printed, sintered and copper infiltrated scaffolds.

To determine the performance of chitosan/acetic acid as a polymer binder solution, the properties of sintered and copper infiltrated samples (printed from chitosan/acetic acid based metallic ink, hereafter referred to CHI) and samples (printed from PLA/DCM based metallic ink, hereafter

referred to PLA) are compared. The comparison is based on the optimized ink recipes (CHI and PLA) for best printing quality. The results of ink filament morphology, size reduction, filament porosity and electrical properties are shown in Figure 5.4. The SEM images of sintered and copper infiltrated scaffolds (CHI) reveal the finer details of the structure, filaments and fused metal powders (Figure 5.4a-b). Both scaffolds keep the shape from the as-printed scaffold (Figure 5.2a) without distortion and the filaments are aligned uniformly and well organized. The individual filament has cylindrical shape. No obvious deformation is observed even for spanning structure. In Figure 5.4c-d, the filaments of the copper infiltrated scaffold show better bonding between neighboring layers than those from sintered ones. It is observed that the melted copper only fills the pores inside the filament instead of spacing between deposited filaments. By properly tailoring the amount of copper, the copper infiltration can be applied to enhance the fine porous structure.[19]

The metal powders fuse together through the sintering, but there are some pores left in the sintered filaments due to the removal of the polymer binder and sintering itself. The pores can be filled by melted copper and the filament surface becomes smoother. The filament porosity is studied by analyzing the optical microscope images of the cross section of the sintered and copper infiltrated scaffolds (Figure 5.4c-d). Pores of similar sizes are uniformly scattered inside the sintered filament. In the copper infiltrated scaffold, melted copper fills most of the pores in the filaments and the gap between contacting filaments. The porosity significantly decreases after copper infiltration. The filament porosities of sintered and copper infiltrated samples are 6.8% ± 1.2% and 1.0% ± 0.2% respectively (Figure 5.4d and Table 5.S1). Compared to the structures (PLA) in our previous work[19], the sintered scaffold (CHI) has less porosity, while the copper infiltrated one exhibits slightly higher porosity. The reason is that the polymer content of the as-printed samples (CHI) (6 vol.%) is much lower than that of the as-printed samples (PLA) (25 vol.%[19]). After polymer decomposition, there are less pores resulting from removing the polymer. The sintered filament (CHI) achieves less porosity after sintering at the same conditions and duration. Less porosity hinders the melted copper from infiltrating into the sintered filaments in the subsequent copper infiltration. It results in higher porosity than the one printed from PLA based ink, but it is still under 1% porosity.

Figure 5.4c shows the linear size reduction of the as-printed, sintered and copper infiltrated samples (CHI and PLA) compared to the designed size. The size changes are caused by the expansion upon extrusion, solvent evaporation, polymer decomposition, sintering and copper infiltration. Table

5.S2 summarizes the linear size reduction values. The extruded ink filament expands because of the pressure drop and then shrinks due to the solvent evaporation. The dried as-printed sample has similar size as designed (0.3% ± 1.4% linear expansion). After polymer decomposition and metal sintering, the sintered structure exhibits a linear reduction of 12.8% ± 2.1% compared to the designed size. The copper infiltrated sample has a sintering duration for 1 h instead of 3-6 h for the sintered samples. More pores are left to allow the melted copper to infiltrate into the sintered filament easily. As a result, the copper infiltrated sample exhibits less size reduction (8.9% ± 2.1% linear reduction) than the sintered one. The samples (CHI) have less size change compared to the samples (PLA) in every stage, as they contain less polymer contents. The size reduction in three dimensions are also studied. The results (Figure 5.S3 and Table 5.S3) indicate that the size reduction does not show significant differences along the directions.

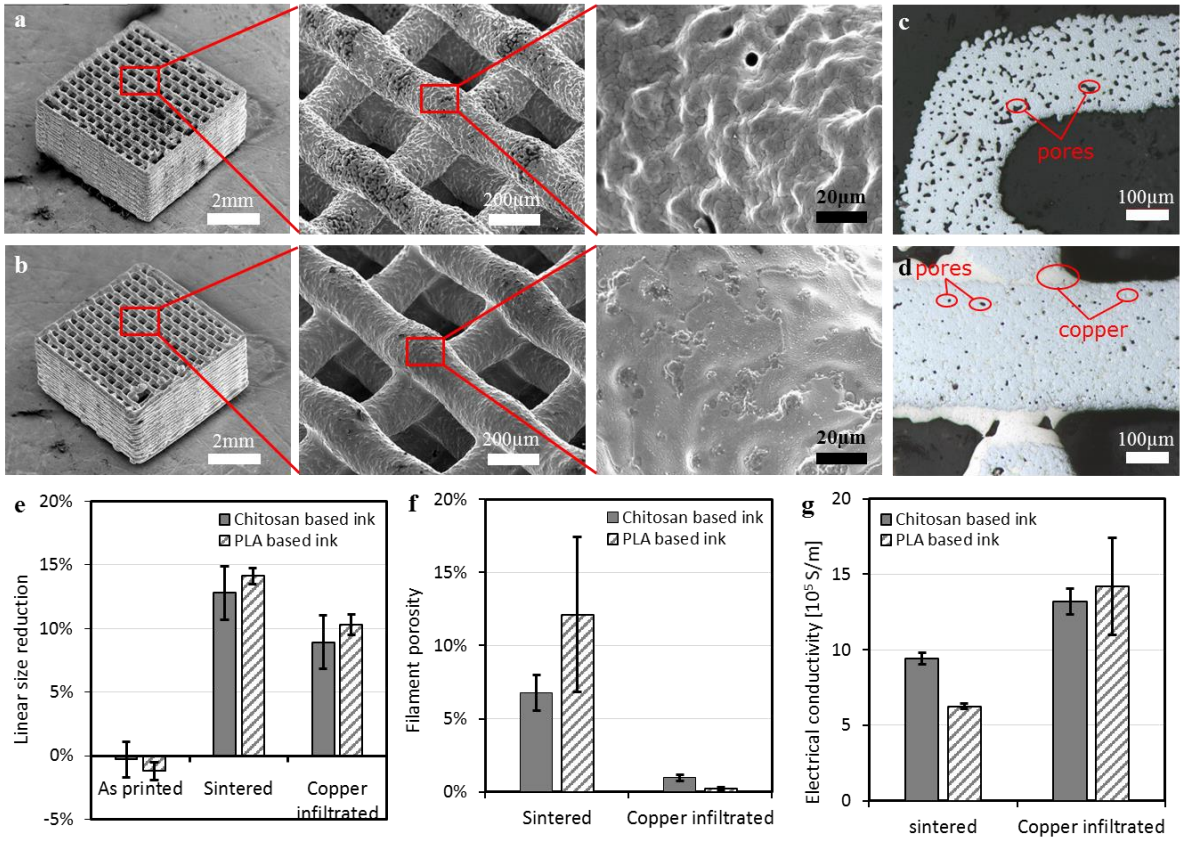

Figure 5.4 SEM images of (a) sintered and (b) copper infiltrated CHI scaffolds at different magnifications and optical image of polished filament cross section of (c) sintered and (d) copper infiltrated samples. (e) The linear size reduction, (f) filament porosity and (g) electrical conductivity of sintered and copper infiltrated scaffolds printed from chitosan based metallic ink and PLA based metallic ink.[19]

The sintered and copper infiltrated samples (CHI) have the electrical conductivity of (9.4 ± 0.4) × 10^5 S/m and (1.3 ± 0.9) × 10^6 S/m, respectively (Figure 5.4e and Table 5.S4). Compared to the samples (PLA), the sintered samples (CHI) are 51% more conductive, while the copper infiltrated samples (CHI) are 7% less conductive. In CHI ink, the polymer volume fraction is lower. As a result, the sintered sample (CHI) has denser structure resulting in a higher electrical conductivity. The copper infiltrated sample (CHI) contains less copper, as its low porosity hinders the copper infiltration. Since copper is more conductive than steel, the copper infiltrated sample (CHI) is slightly less conductive than the one printed from PLA based ink.

Tensile tests are conducted on the sintered and copper infiltrated tensile bars to investigate their mechanical properties. Figure 5.5 shows the representative tensile stress-strain curves, optical images of representative tensile bars and SEM images of the tensile fracture surfaces. The observed Young's modulus *E*, ultimate tensile strength (UTS) and elongation at breakage (%) are summarized in Table 5.S5. The previous tensile test results of the samples printed from PLA base ink are also listed for comparison.[19] The *E* modulus of the sintered samples (CHI) is ~205 GPa, which is improved by 5% when compared with the samples printed from PLA based ink. The UTS and elongation at break, however, are decreased by 32% and 60% respectively. The stiffness (*E*) is increased, while the ductility (UTS and elongation at break) is sacrificed. Compared to the sintered samples, the copper infiltrated samples (CHI) exhibit better UTS (522 MPa) and elongation at break (0.69%). The infiltrated copper improves the ductility of the sintered samples. As the copper infiltrated samples go through a shorter sintering duration (1h), the *E* modulus (160 GPa) is lower than the sintered ones. As the chitosan binder can introduce extra carbon to the sintered metal structure, it hardens the structure. It is more suitable for low carbon content metal alloys, where it can improve the stiffness without sacrificing the ductility.

The tensile fracture surfaces of the sintered and copper infiltrated samples are studied for better understanding the mechanism (Figure 5.5b-e). In the sintered sample (Figure 5.5b), most of the filaments from the same and different layers merge together, although some tiny pores are left in the structure. The copper infiltrated sample (Figure 5.5c) has a denser structure. The high magnification SEM images (Figure 5.5d-e) show the details of the tensile fracture surface. All the metal powders fuse and merge together. No individual metal particle is visible under SEM. The structure is a single entity with a few tiny pores.

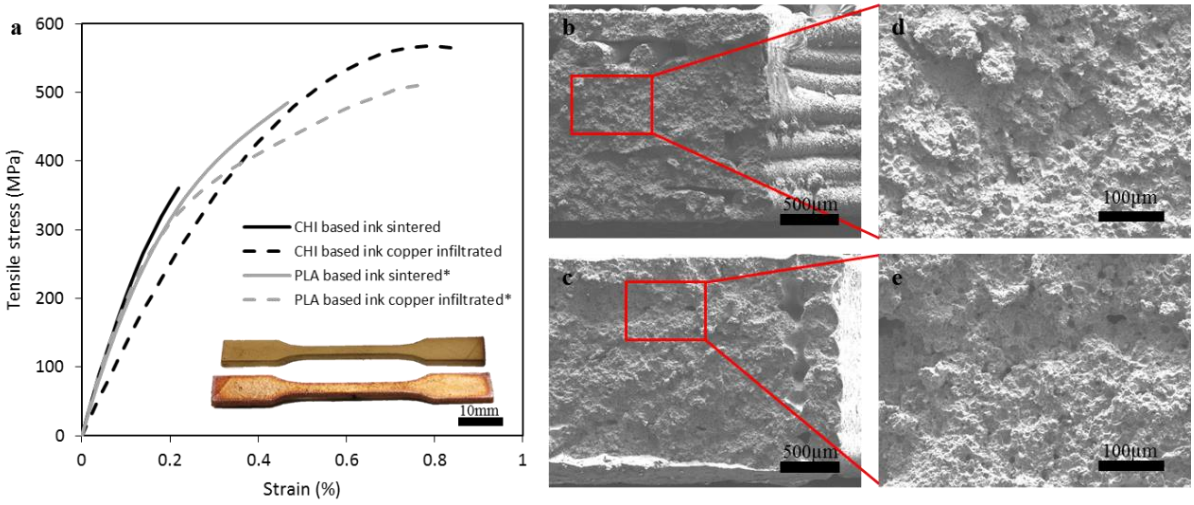

Figure 5.5 (a) Tensile stress versus strain curves for sintered and copper infiltrated tensile samples printed using chitosan based ink and PLA based ink[19] and optical image of sintered and copper infiltrated tensile samples (inset). SEM images of tensile fracture surfaces of sintered and copper infiltrated tensile bars at (b,c) low and (d,e) higher magnification, respectively.

Figure 5.6 presents various 3D metallic structures fabricated using our green ink and Video 5.S3 shows the printing process in motion. As-printed and sintered 3D structures are shown in Figure 5.6a. Relatively complex structures, such as the octopus and skull, can be easily printed and maintain their fine features after sintering in spite of a size reduction. The size reduction appears to be reproducible for a specific temperature profile and could be compensated by introducing an offset in the design stage. Figure 5.6b shows fully dense sintered structures including a replica of Mayan pyramid and a pair of elliptical gears. The steps along the side of the pyramid are clear and the corners are relatively sharp. The elliptical gears mesh well with each other without any post sintering surface treatments. Our extrusion-based approach is also compatible with the fabrication of porous metallic structures, not always possible with power-bed methods. A fine porous femur bone with a designed porosity of 50% is fabricated (see Figure 5.6c). The pores and tunnels in the structure are designed in the CAD model. The filling density can be tailored from 20% to 100% using the slicing software, achieving a porous structure with desired effective stiffness and weight. The porous structures are printed at room-temperature and can withstand subsequent sintering. 3D twisted vases with a porous infill and a solid surface layer are shown in Figure 5.6c. Their surface is smoother than porous structures and they weigh less than fully dense structures. However, the

structures without a flat bottom surface have to be printed with the assistance of supporting structures (e.g. the femur bone in Figure 5.6c).

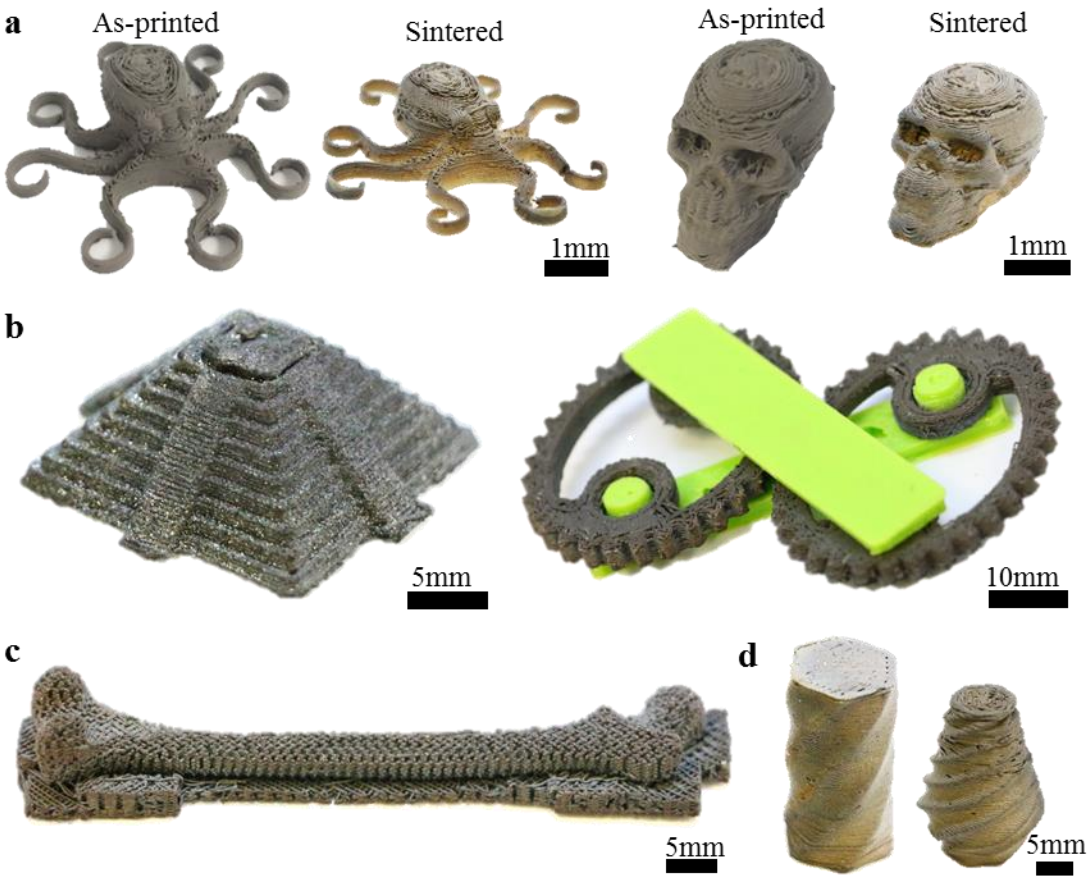

Figure 5.6 Various 3D printed structures, including (a) as-printed and sintered octopus and skull, (b) fully dense sintered structures: a replica of Mayan pyramid and a pair of elliptical gears, (c) a porous femur bone with a designed porosity of 50%, and (d) twisted vases with a porous infill and a solid surface layer.

5.4 Conclusion

We have developed an environment-friendly and reusable metallic ink for 3D printing of highly dense metallic structures. The metallic ink contains steel micro powders, a biodegradable polymer: chitosan, acetic acid and deionized water. It can be applied in a low-cost SC-3DP method to fabricate metallic structures and overcome the use of toxic solvent. The ink is reusable which improves the metallic materials utilization. An airflow system is used to counterbalance the shortcomings of SC-3DP methods by accelerating solvent evaporation and shortening the

solidification duration of the extruded ink filament, reducing the sagging and the shape deformation. The morphology, size reduction, filament porosity, electrical conductivity and mechanical properties of the fabricated structures are characterized. Comparing with commonly used more toxic PLA/DCM based metallic ink, our ink produces 3D metal structures with less size reduction, lower filament porosity while demonstrating comparable electrical and mechanical performances. We envision that the chitosan polymer solution system could apply to diverse metallic materials, metal oxides and ceramics to obtain green and reusable 3D-printable inks. The structures built using this approach can be potentially used in biomedical and aerospace fields since geometrically complex shapes are porous configurations are often preferred. We foresee that artificial bone implants with fine and uniform pores, as well as complex 3D porous aerospace structures featuring light weight and high mechanical performance can be fabricated using this ink in a very economical fashion.

Acknowledgements

The authors acknowledge the financial support from NSERC (Natural Sciences and Engineering Research Council of Canada, grant number: RGPIN 312568-2013) and Auto 21 of the Canadian Network of Centers of Excellence (NCE) program. A scholarship for Mr. Xu was also provided by the China scholarship Council (CSC) and the Fonds de recherche du Quebec - Nature et technologies (FRQNT).

Data availability

The raw/processed data required to reproduce these findings can’t be shared at this time as the data also forms part of an ongoing study.

References

1. J. H. Martin, B. D. Yahata, J. M. Hundley, J. A. Mayer, T. A. Schaedler, T. M. Pollock, 3D printing of high-strength aluminium alloys, *Nature*, 2017, 549, 365-369.
2. J. R. Greer, J. Park, Additive Manufacturing of Nano-and Microarchitected Materials, *Nano Lett.*, 2018, **4**, 2187-2188.

3. T. DebRoy, H. L. Wei, J. S. Zuback, T. Mukherjee, J. W. Elmer, J. O. Milewski, A. M. Beese, A. Wilson-Heid, A. De, W. Zhang, Additive manufacturing of metallic components–process, structure and properties, *Prog. Mater. Sci.*, 2018, **92**, 112-224.
4. S. Bose, D. Ke, H. Sahasrabudhe, A. Bandyopadhyay, Additive manufacturing of biomaterials, *Prog. Mater. Sci.*, 2018, **93**, 45-111.
5. X. Wang, S. Xu, S. Zhou, W. Xu, M. Leary, P. Choong, M. Qian, M. Brandt, Y. M. Xie, Topological design and additive manufacturing of porous metals for bone scaffolds and orthopaedic implants: a review, *Biomaterials*, 2016, **83**, 127-141.
6. A. Basalah, Y. Shanjani, S. Esmaeili, E. Toyserkani, Characterizations of additive manufactured porous titanium implants, *J. Biomed. Mater. Res., Part B*, 2012, **100**, 1970-1979.
7. R. Bernasconi, F. Cuneo, E. Carrara, G. Chatzipirpiridis, M. Hoop, X. Chen, B. J. Nelson, S. Pané, C. Credi, M. Levi, L. Magagnin, Hard-magnetic cell microscaffolds from electroless coated 3D printed architectures, *Mater. Horiz.*, 2018, **5**, 699-707.
8. Y. S. Rim, S. H. Bae, H. Chen, N. D. Marco, Y. Yang, Recent progress in materials and devices toward printable and flexible sensors, *Adv. Mater.*, 2016, **28**, 4415-4440.
9. A. Vyatskikh, S. Delalande, A. Kudo, X. Zhang, C. M. Portela, J. R. Greer, Additive manufacturing of 3D nano-architected metals, *Nat. Commun.*, 2018, **9**, 593.
10. D. W. McOwen, S. Xu, Y. Gong, Y. Wen, G. L. Godbey, J. E. Gritton, T. R. Hamann, J. Dai, G. T. Hitz, L. Hu, Eric. D. Wachsman, 3D-Printing Electrolytes for Solid-State Batteries, *Adv. Mater.*, 2018, 1707132.
11. B. M. Sánchez, Y. Gogotsi, Synthesis of Two-Dimensional Materials for Capacitive Energy Storage, *Adv. Mater.*, 2016, **28**, 6104-6135.
12. A. E. Jakus, S. L. Taylor, N. R. Geisendorfer, D. C. Dunand, R. N. Shah, Metallic architectures from 3D-printed powder-based liquid inks, *Adv. Funct. Mater.*, 2015, **25**, 6985-6995.
13. R. D. Farahani, M. Dubé, D. Therriault, Three-dimensional printing of multifunctional nanocomposites: manufacturing techniques and applications, *Adv. Mater.*, 2016, **28**, 5794-5821.

14. H. Gong, K. Rafi, H. Gu, G. D. J. Ram, T. Starr, B. Stucker, Influence of defects on mechanical properties of Ti–6Al–4 V components produced by selective laser melting and electron beam melting, *Mater. Des.*, 2015, **86**, 545-554.
15. E. O. Olakanmi, R. F. Cochrane, K. W. Dalgarno, A review on selective laser sintering/melting (SLS/SLM) of aluminium alloy powders: Processing, microstructure, and properties, *Prog. Mater. Sci.*, 2015, **74**, 401-477.
16. R. Chou, J. Milligan, M. Paliwal, M. Brochu, Additive manufacturing of Al-12Si alloy via pulsed selective laser melting, *JOM*, 2015, **67**, 590-596.
17. M. A. Skylar-Scott, S. Gunasekaran, J. A. Lewis, Laser-assisted direct ink writing of planar and 3D metal architectures, *Proc. Natl. Acad. Sci.*, 2016, **113**, 6137-6142.
18. A. B. Yeop, D. Shoji, C. J. Hansen, E. Hong, D. C. Dunand, J. A. Lewis, Printed origami structures, *Adv. Mater.*, 2010, **22**, 2251-2254.
19. C. Xu, A. Bouchemit, G. L'Espérance, L. L. Lebel, D. Therriault, Solvent-cast based metal 3D printing and secondary metallic infiltration, *J. Mater. Chem. C*, 2017, **5**, 10448-10455.
20. E. Peng, X. Wei, T. S. Herng, U. Garbe, D. Yu, J. Ding, Ferrite-based soft and hard magnetic structures by extrusion free-forming, *RSC Adv.*, 2017, **7**, 27128-27138.
21. Q. Wu, M. Maire, S. Lerouge, D. Therriault, M. C. Heuzey, 3D printing of microstructured and stretchable chitosan hydrogel for guided cell growth, *Adv. Biosyst.*,2017, **1**, 1700058.
22. C. Peniche-Covas, W. Argüelles-Monal, J. S. Román, A kinetic study of the thermal degradation of chitosan and a mercaptan derivative of chitosan, *Polym. Degrad. Stab.*, 1993, **39**, 21-28.
23. E. P. DeGarmo, J. T. Black, R. A. Kohser, B. E. Klamecki, Materials and process in manufacturing. Prentice Hall, 1997.

5.5 Supporting information

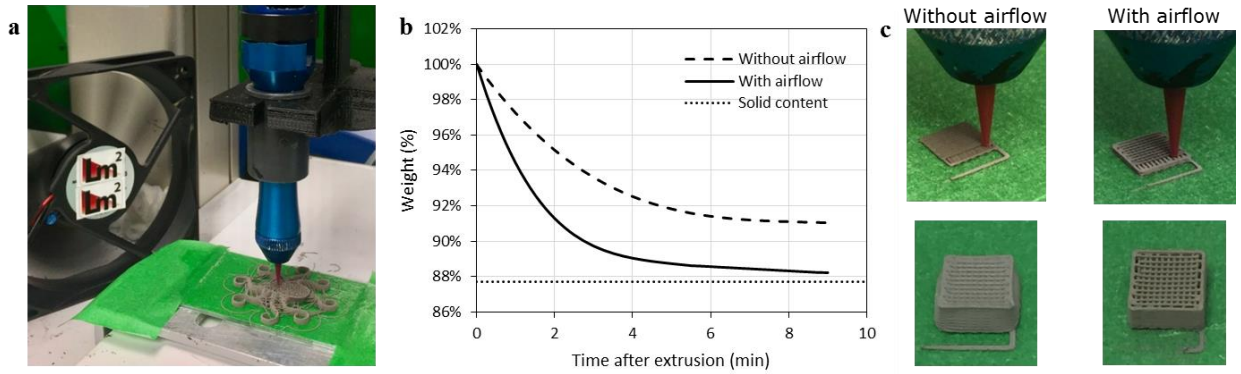

Figure 5.7 (a) Printing process with an airflow system, (b) Investigation on solvent evaporation rate: the weight of the extruded filament as a function of time after extrusion with and without the airflow, (c) Comparison of the printing process and as-printed scaffolds with and without airflow system**.**

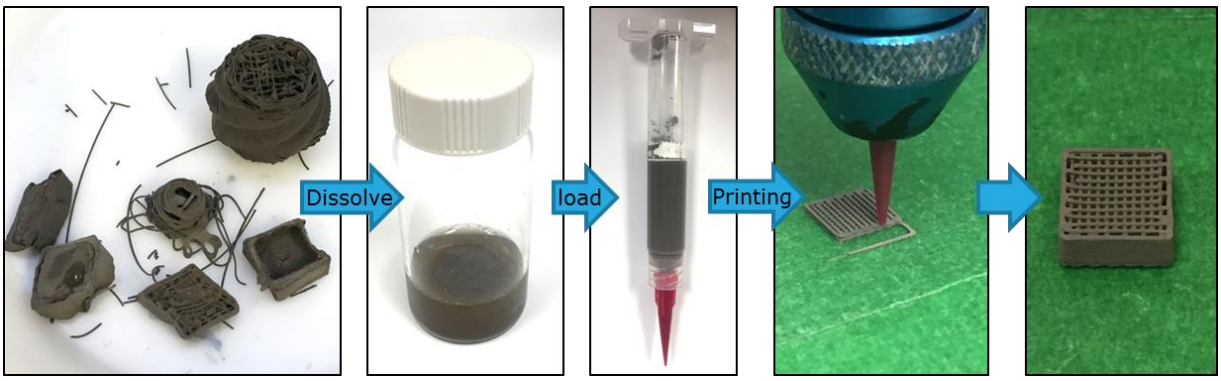

Figure 5.8 3D printed metal/polymer hybrid structures and scrap materials can be recycled to generate new 3D-printable metallic ink. They are dissolved in the acid solvent in proportion according to the ink recipe (Table 5.1) and then mixed using the ball mill. After homogenization, the metallic ink is loaded in a syringe barrel for printing. New structures can be printed with the recycled metallic ink.

Table 5.2 Filament porosity of the sintered and copper infiltrated samples printed from chitosan based ink and PLA based ink[19]

	Sintered	Copper infiltrated
CHI based ink	6.8% ± 1.2%	1.0% ± 0.2%
PLA based ink*	12.1% ± 5.3%	0.2% ± 0.1%

Table 5.3 Compared to the designed size, linear shrinkage of the as-printed, sintered and copper infiltrated samples printed from CHI based ink and PLA based ink[19]

	As-printed	Sintered	Copper infiltrated
CHI based ink	-0.3% ± 1.4%	12.8% ± 2.1%	8.9% ± 2.1%
PLA based ink*	-1.2% ± 0.7%	14.1% ± 0.6%	10.3% ± 0.8%

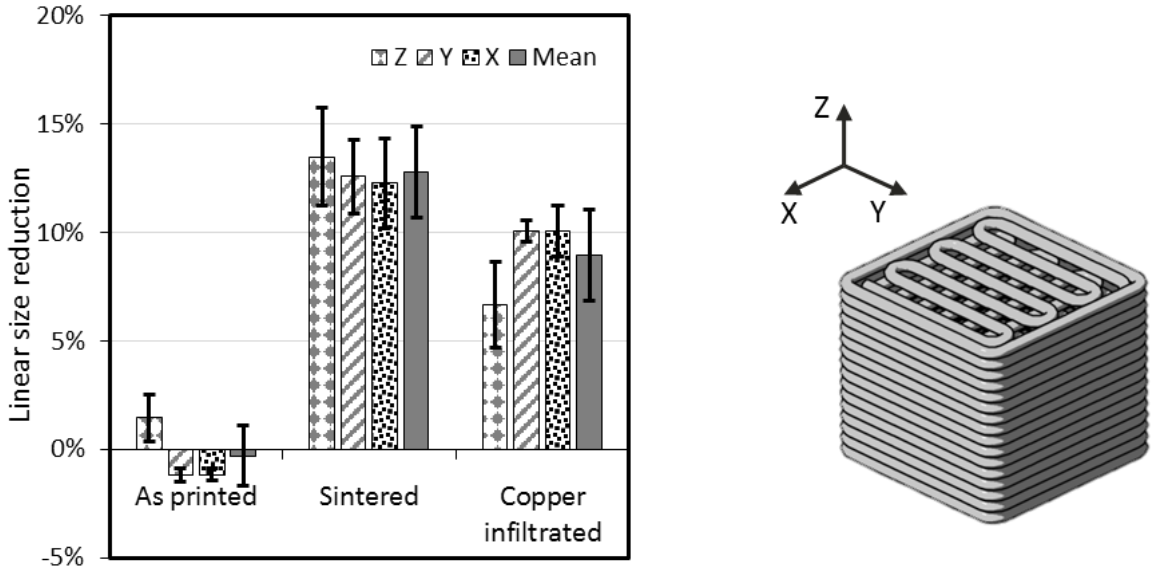

Figure 5.9 Linear size reduction of the as-printed, sintered and copper infiltrated samples compared to the designed size in x, y, z axis and the average and a schematic of the scaffold indicating the three axes

Table 5.4 Electrical conductivity of the sintered and copper infiltrated samples printed from chitosan based ink and PLA based ink[19]

Electrical conductivity [S/m]	Sintered	Copper infiltrated
CHI based ink	$(9.4 \pm 0.4) \times 10^5$	$(1.3 \pm 0.9) \times 10^6$
PLA based ink*	$(6.2 \pm 0.2) \times 10^5$	$(1.4 \pm 0.3) \times 10^6$

Table 5.5 Tensile test results of the sintered and copper infiltrated samples printed from CHI based ink and PLA based ink[19]

	Young's modulus (GPa)	Ultimate tensile stress (MPa)	Elongation at break (%)
CHI based ink sintered	205 ± 22	329 ± 35	0.19 ± 0.03
CHI based ink copper infiltrated	160 ± 29	522 ± 83	0.69 ± 0.13
PLA based ink sintered*	196 ± 16	485 ± 70	0.47 ± 0.06
PLA based ink copper infiltrated*	195 ± 16	511 ± 57	0.77 ± 0.07

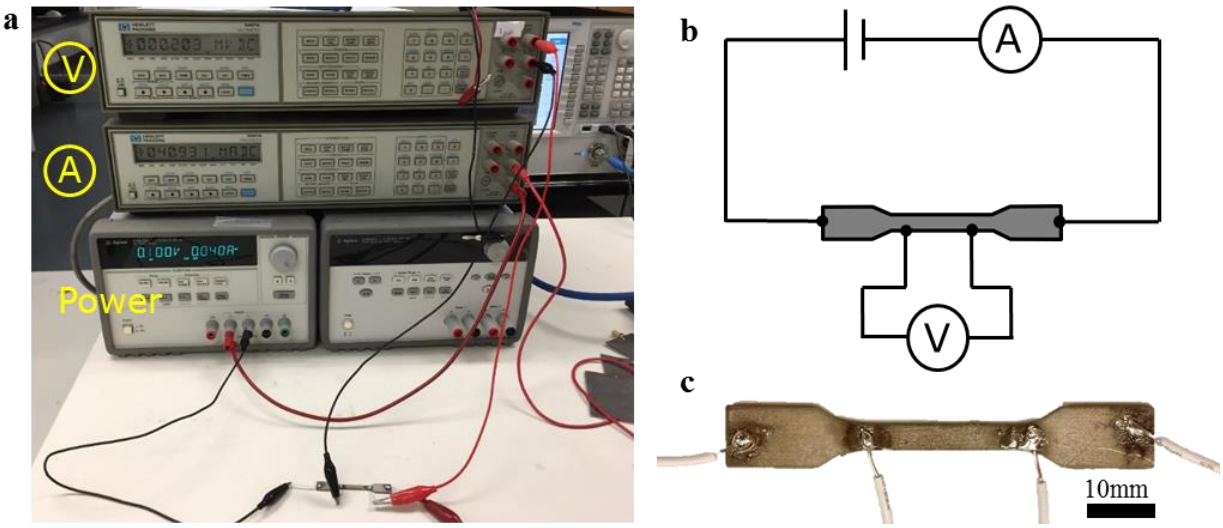

Figure 5.10 Electrical conductivity measurement using four-point probes method. (a) The experimental devices, (b) the circuit diagram, and (c) the representative sample

Video 5.1 https://www.sciencedirect.com/science/article/pii/S0264127518307184#ec0005

Video 5.2 https://www.sciencedirect.com/science/article/pii/S0264127518307184#ec0010

Video 5.3 https://www.sciencedirect.com/science/article/pii/S0264127518307184#ec0015

CHAPTER 6 ARTICLE 3: MULTI-MATERIAL DIRECT INK WRITING (DIW) FOR COMPLEX 3D METALLIC STRUCTURES WITH REMOVABLE SUPPORTS

Submitted to *Small*, November 2018

By

Chao Xu, Bronagh Quinn, Gilles L'Espérance, Louis Laberge Lebel and Daniel Therriault*

ABSTRACT

Direct ink writing (DIW) combined to post-deposition thermal treatments is a safe, cheap and accessible additive manufacturing (AM) method for the creation of metallic structures. Single material DIW enables the creation of complex metallic 3D structures featuring overhangs, lengthy bridges or enclosed hollows, but requires the printing supporting structures. However, the support printed from the same material becomes inseparable from the building structure after the thermal treatment. Here, a multi-material DIW method is developed to fabricate complex three-dimensional (3D) steel structures by creating a removable support printed from a lower melting temperature metal (i.e., copper) or a ceramic (i.e., alumina). The lower melting temperature metal completely infiltrates the porous steel structures for a hybrid configuration, while the ceramic offers a brittle support that can be easily removed. The influence of the support materials on the steel structure properties is investigated by the characterizing the dimensional shrinkage, surface roughness, filament porosity, electrical conductivity and tensile properties. The hybrid configuration (i.e., copper infiltrated steel structures) improves the electrical conductivity of the fabricated steel structure by 400% and the mechanical stiffness by 34%. The alumina support is physically and chemically stable during the thermal treatment, bringing no significant contamination to the steel structure.

6.1 Introduction

Metallic structures fabricated through Additive manufacturing (AM), also referred to as three-dimensional (3D) printing, have been used as batteries,[1-2] medical implants,[3-4] and sensors[5-6]

due to their key advantages, i.e., high mechanical and electrical properties, complex geometries, and mold-free manufacturing processes. The most established metal AM approaches are powder-bed based methods such as selective laser melting (SLM) and electron beam melting (EBM).[7-9] They use a laser beam or electron beam to locally fuse metallic particles in a powder bed to build a 3D object layer-by-layer. These methods feature short manufacturing time, high mechanical performance of the fabricated parts and very few restrictions on the printed geometry. However, they are limited by high cost, laser induced excessive oxidation, and residual stresses in the fabricated parts.[10-12]

Direct ink writing (DIW) is an AM method, which usually relies on the extrusion of polymer solution (or melt), known as ink, through a micro-nozzle and the deposition of the extruded ink on a substrate layer by layer to create a 3D object.[13-14] Researchers adapted it to metal AM to overcome some of the shortcomings of the powder-bed methods.[15-18] Metallic inks are prepared by adding metal micro- or nano- particles to the polymer solution (or melt), which are used in DIW to build a metal-polymer composite 3D structure. To achieve a metallic structure featuring high mechanical and electrical performances, a post-deposition thermal treatment is performed to pyrolyze the polymer and to sinter the metal particles.

DIW of polymer can create complex 3D structures with large overhangs or lengthy bridges by printing support underneath them to hold the structures. Once the printing is completed, the sacrificial support is removed.[19-20] However, the utilization of a support does not work for DIW of metal, where a post-deposition thermal treatment is performed. If the support is removed before the thermal treatment at a moment when the polymer binder is pyrolyzed before the sintering of the metallic particles, the overhang features will collapse. Whereas, if the support printed from the same material is not removed before the thermal treatment, the support and the building structure will fuse together and become inseparable after the thermal treatment. Thus, the existed DIW methods are unable to fabricated complex 3D metallic structures featuring overhangs, length bridges or enclosed hollows.

6.2 Results and discussion

Here, we propose a multi-material DIW method to fabricate complex 3D metallic structures with removable supports. This method consists of two steps: (a) room-temperature DIW of metal-

polymer composite structures with metal- (or ceramic-) polymer composites supports, and (b) a post-deposition thermal treatment turning the as-printed metal-polymer composite structures to metal structures. **Figure 6.1a** shows a schematic of the multi-material DIW system and as-printed hollow sphere structures. The multi-material DIW system includes three major components: (i) a computer controlled 3-axis robot, (ii) a pressure dispenser, and (iii) multiple ink syringes containing steel, copper and alumina inks. The inks are concentrated steel, copper and alumina microparticle suspensions dispersed in a polymer solution (i.e., polylactic acid / dichloromethane, referred to as PLA/DCM), respectively. The scanning electron microscope (SEM) images of the microparticles are shown in **Figure 6.S1**. To fabricate a 3D metallic structure, e.g., a hollow sphere as shown in **Figure 6.1a**, supports are generated inside the hollow sphere to support the top overhang part and underneath the sphere to create a flat bottom which is compatible with the geometry of the substrate. Here, as a proof of concept, the supports are built using a secondary material (i.e., copper or alumina ink), while the building structure is printed with the primary material (i.e., steel ink). The steel-PLA composite structure with copper-PLA composite support is referred to as as-printed S-Cu, while the one with alumina-PLA composite support is referred to as as-printed S-Al_2O_3. These two types of supports are differently removed through the post-deposition thermal treatment. The lower melting temperature metallic support (i.e., copper) could be completely melted and infiltrated into the pores of the structural part to achieve a hybrid configuration. The ceramic support (i.e., ceramic) survives the temperature cycle without any significant sintering and can be easily removed without affecting the metallic structure.

Figure 6.1b presents the temperature profile of the thermal treatment, the thermal gravity analysis (TGA) result of the polymer binder PLA under this temperature profile, the sintering temperature range and melting temperature of stainless steel 316L and copper.[21-22] In addition, a schematic is shown in **Figure 6.1b** illustrating the microstructure variations of the two-phase interface in the as-printed structures at five different stages during the thermal treatment. For S-Cu structures, Stage (I) is an as-printed structure at room temperature, where the steel and copper particles are bound by the PLA binder, respectively. Stage (II) consists of a one-hour plateau at 400°C for debinding. PLA binder is completely pyrolyzed as shown in the TGA curve, where the weight of the PLA binder rapidly drops within 7 min. The structure is held by the friction forces among the steel particles and among copper particles, respectively. The temperature then is increased to reach a temperature plateau at 950°C for one hour (Stage III). This plateau temperature is selected to be

in the sintering temperature range of S316L and copper, but is lower than their melting temperatures. The S-Cu structure is mechanically enhanced by initial sintering, where the necks appear among steel particles and among copper particles, respectively. After this stage, even if the support is removed, the bonding between the steel particles is strong enough to hold the building structure. During Stage (IV), the temperature increases from 950°C to 1165°C, surpassing the melting temperature of copper (i.e. 1085°C). The copper support starts melting, while the steel structure is held in its original geometry by the sintering bonds generated during Stage (III). Stage (V) is a four-hour plateau at 1165°C, where the steel particles are further sintered and the melted copper completely infiltrates the pores of the sintered steel structure by capillary forces. After this temperature profile, the as-printed S-Cu is turned into a steel structure infiltrated by the copper.

For S-Al_2O_3 structures, Stages (I) and (II) are the as-printed structure at room temperature and the debinding process respectively, like those of the S-Cu structures. Since both the melting temperature of alumina (2040°C) and the lower limit of alumina sintering temperature (1800°C)[23] are much higher than the maximum imposed temperature (1165°C), the alumina particles are neither melted nor sintered, but remain as individual particles during the whole thermal treatment. Therefore, in Stages (III) to (V), the alumina support preserves its shape mostly due to the friction forces among the alumina particles. The steel particles are sintered and form a strong steel keeping the original geometry. As the alumina support is weakly held by the friction forces, it does not fuse with the building structure and can be easily removed by hand after the thermal treatment.

Figure 6.1c shows the as-printed and sintered S-Cu and S-Al_2O_3 printed using this method as a structure shaped as a human thigh bones at a scale of 1:7. The steel bone structure is 50% of volume filled, while the support structure is 30% of volume filled. The supports provide a flat bottom and hold up the overhang features for the bone to facilitate the printing on a flat substrate. After the thermal treatment, the copper support melts and infiltrates into the sintered steel structure, while the alumina support is removed easily by hand. Both sintered structures preserve the original geometry of the human thigh bone with a uniform linear dimensional shrinkage of 11%.

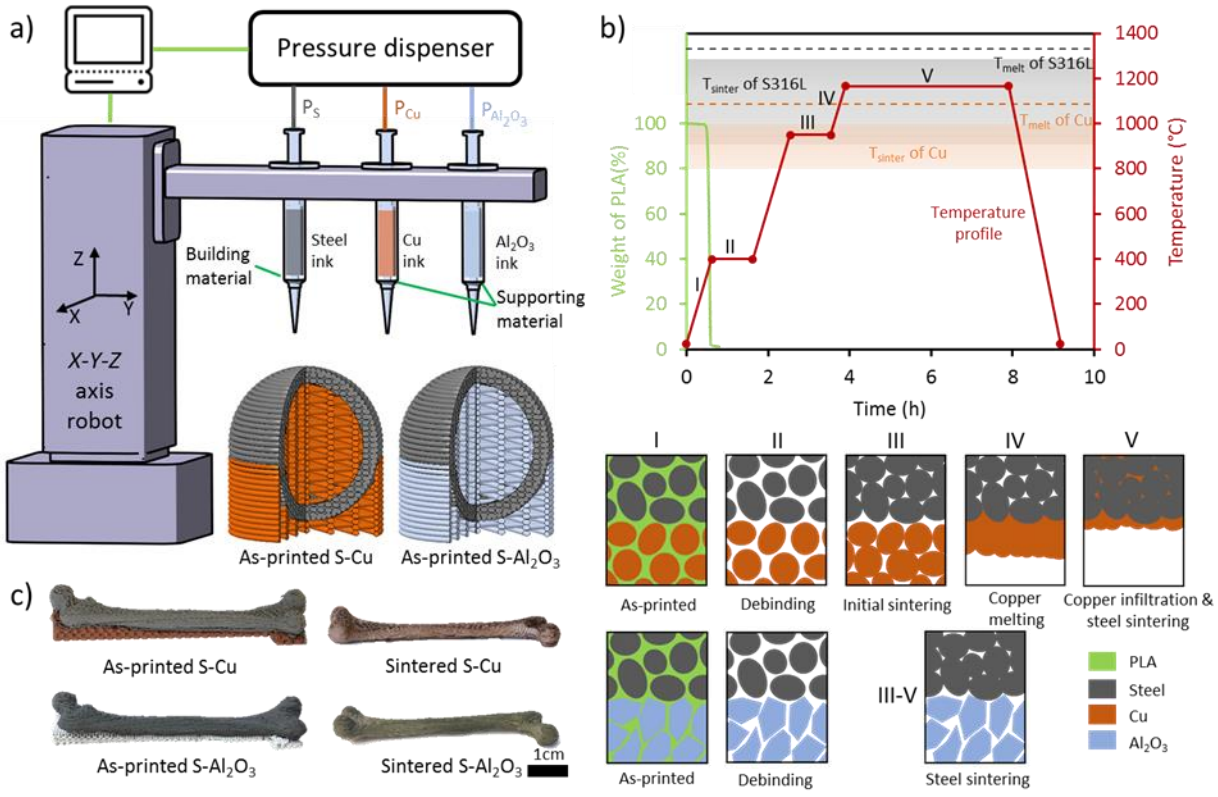

Figure 6.1 Multi-material DIW for complex 3D metallic structures with removable supports consists of two steps: (a) room-temperature DIW of metal-polymer composite structures with metal- (or ceramic-) polymer composites supports and (b) a post-deposition thermal treatment turning the as-printed metal-polymer composites structures to metal structures. (c) An optical image of as-printed and sintered S-Cu and S-Al_2O_3 thigh bones fabricated using this method. Multi-material DIW for complex 3D metallic structures with removable supports consists of two steps: (a) room-temperature DIW of metal-polymer composite structures with metal- (or ceramic-) polymer composites supports, and (b) a post-deposition thermal treatment turning the as-printed metal-polymer composites structures to metal structures, and a schematic shows the two-phase interface microstructures variations of the as-printed structures at five different stages during the thermal treatment. (c) Optical images of as-printed and sintered S-Cu and S-Al2O3 structures printed as a human thigh bones at a scale of 1:7.

Steel scaffolds (S), steel scaffolds with copper support (S-Cu) and steel scaffolds with alumina support (S-Al_2O_3) are printed and thermally treated to investigate the influence of the support materials to the building structures. **Figure 6.2a** shows optical and SEM images of as-printed and

sintered (thermally treated) S, S-Cu and S-Al_2O_3 scaffolds. The as-printed steel scaffolds supported by copper and alumina are as neat and orderly structured as the as-printed steel scaffold without support. The steel, copper and alumina particles are bound by the PLA binder to hold the structures, respectively. After the thermal treatment, the steel scaffolds retain their geometry, but exhibit some dimensional shrinkage. The SEM images of the sintered (thermally treated) scaffolds at different magnifications are presented in **Figure 6.S2**. They have similar linear size reduction ranging from 10.7% to 11.2% (**Figure 6.2b**). Each type of steel scaffolds has a small size deviation of ≤1.3% (**Figure 6.2b**). The small deviation guarantees the reproducibility of this method in terms of dimensional accuracy of the fabricated structures. The steel particles of the S-Al_2O_3 scaffold are just as sintered as those in the S scaffold, but the S-Al_2O_3 scaffold has a rougher surface. The steel particles in S-Cu scaffold are sintered as well. In addition, the copper support melts and infiltrates into the sintered steel structure, leading to a smoother surface.

Figure 6.2c shows the single filament surface roughness (named as micro R_a) and the inter-filament surface roughness (termed as meso R_a) of the sintered steel scaffolds, and SEM images of the measured surfaces serving as an example of the micro and meso R_a. The profilometer probe traveling direction (measuring direction) is perpendicular to the filament longitudinal axis. The micro R_a of sintered S-Al_2O_3 (4.1μm) is greater than that of sintered S (2.5μm), while the micro R_a of sintered S-Cu (1.6μm) is smaller than that of sintered S. The meso R_as of sintered S and sintered S-Cu are similar (~5μm), which are smaller than that of sintered S-Al_2O_3 (13.9μm). The thermally treated alumina scaffold is so fragile that the shrinkage and surface roughness could not be measured. The shrinkage difference between the thermally treated ceramic particles and the sintered steel particles leads to a rougher surface. According to our observations, the support materials have little influence on the dimensional shrinkage of the steel scaffolds. The alumina support appears to increase the micro and meso surface roughness of the sintered steel structure by 1.6μm and 9μm, respectively.

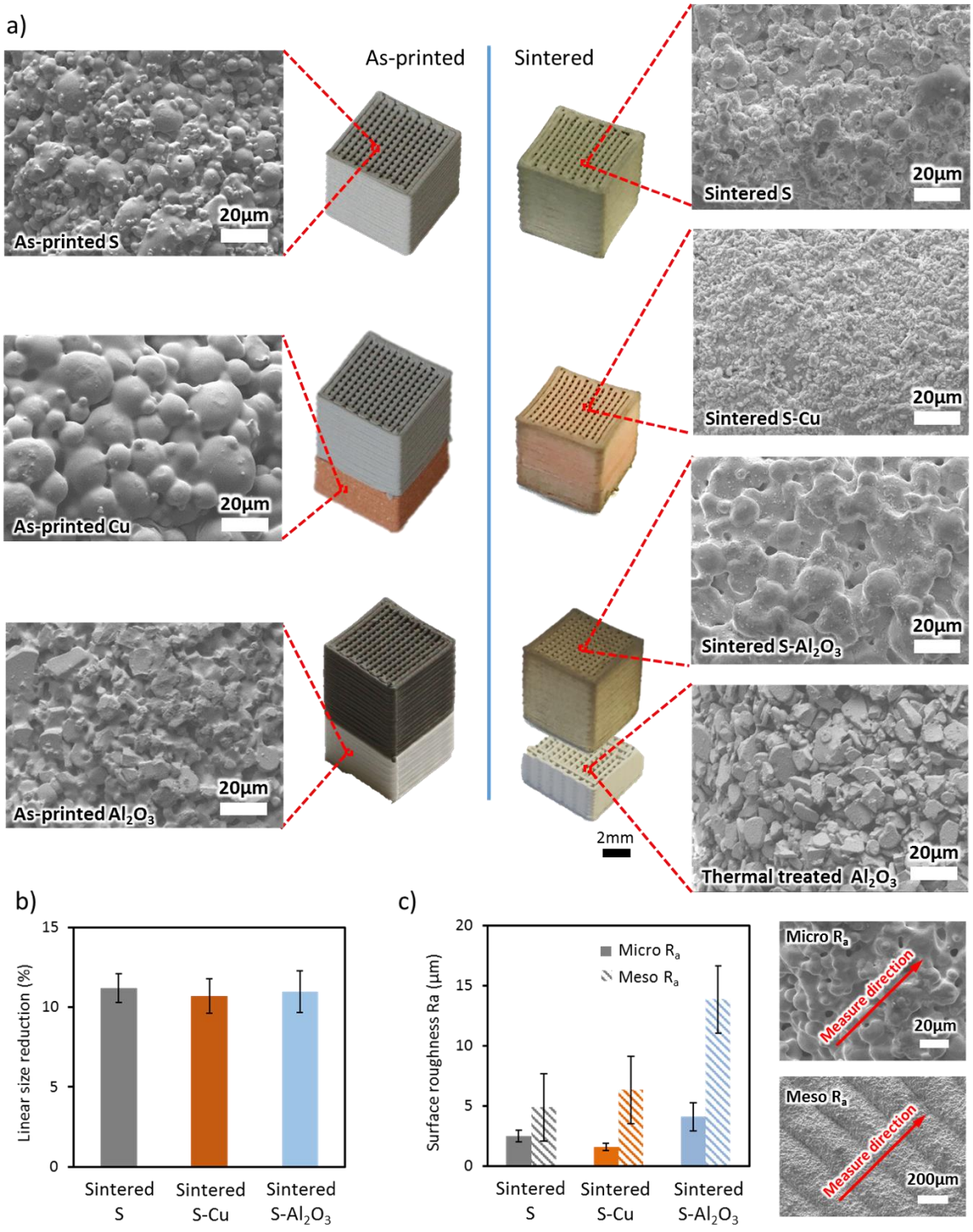

Figure 6.2 (a) Optical and SEM images of as-printed and sintered (thermal treated) scaffolds. (b) Linear size reduction of the sintered steel structures. (c) Single filament surface roughness (micro R_a) and inter-filament surface roughness (meso R_a) of the sintered steel structures, and SEM images of the measured surfaces serving as an example of the micro and meso R_a.

The influence of the support materials to the elemental composition and porosity of the building structures is studied through SEM and elemental analysis. **Figure 6.3a** shows SEM images and Energy-dispersive X-ray spectroscopy (EDS) elemental mappings of the cross sections of sintered S, sintered S-Cu, and sintered S-Al_2O_3 structures. The cross sections of the three types of sintered steel structures are characterized by the strong presence of iron. Copper is detected only in the sintered S-Cu structures as expected. The detection of copper is located in the regions between the iron rich zones. Aluminum and oxygen (i.e., the elements contained in the alumina support) are not detected in the sintered S-Al_2O_3 structures. Neither in the sintered S and sintered S-Cu structures. The elemental analysis result shows that: (i) the copper support infiltrates into the building structure and fills the majority of the pores in the sintered steel structure during the thermal treatment, and (ii) the alumina support is chemically stable during the thermal treatment and does not contaminate the steel structure. The volume fractions of the solid phases (iron for S and S-Al_2O_3, iron and copper for S-Cu) are similar in all three types of sintered steel structures at ~ 98% (**Figure 6.3b**). In the sintered S-Cu structure, the iron phase takes up about 87.2% and the copper phase accounts for around 10.4%. This value can be controlled by the volume ratio of the support and building structure, which will be studied in the future work. All the three types of sintered steel structures have similar and low porosity (~2%), and small pore size between 2 and 3 μm (Figure 6.3c-d). The supports do not have an obvious influence on the porosity and pore size to the building structure.

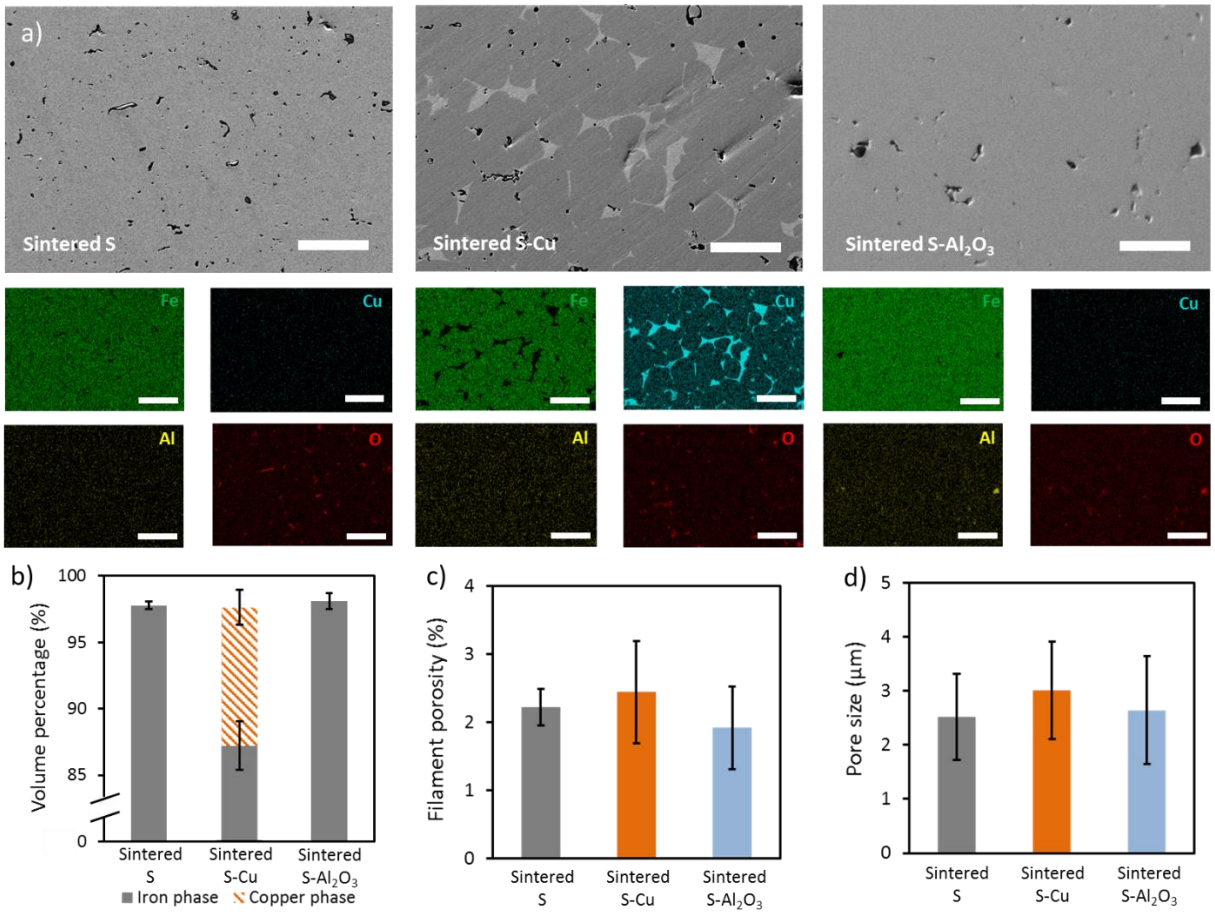

Figure 6.3 Elemental and porosity analysis of the sintered steel structures. (a) SEM images and EDS elemental mappings of the cross sections of sintered S, sintered S-Cu, and sintered S-Al_2O_3 structures. Scale bar = 50μm. (b) Volume percentage of iron and copper phase, (c) filament porosity, and (d) filament pore size of the various sintered steel structures.

Figure 6.4 shows the results for the electrical and tensile tests conducted on the sintered steel structures manufactured using different support materials.. **Figure 6.4a** presents typical tensile stress-strain curves and representative optical image of the sintered S, S-Cu and S-Al_2O_3 tensile bars in the inset. **Figure 6.S3** presents the SEM images of the sintered S, S-Cu and S-Al_2O_3 fully dense tensile bars. Stereoscopic digital image correlation (DIC) technique is used to measure the strain in the tensile bars during the tensile tests (**Figure 6.S4**). The measured tensile properties of the sintered steel structures are shown in **Figure 6.4b**. Sintered S-Cu exhibits higher Young's modulus *E* (174 ± 10 GPa), yield strength (*YS*) (284 ± 16 MPa) and ultimate tensile strength (*UTS*) (521 ± 57 MPa) and elongation at failure (11.3% ± 3.6%) compared to those of sintered S (~30%

- 45% superior). This increase in tensile properties is the result of copper infiltration of the sintered steel structure. Sintered S-Al_2O_3 has weaker tensile properties compared to the sintered S. The *E* (108 ± 6 GPa), the *YS* (165 ± 8 MPa) and the *UTS* (304 ± 18 MPa) of sintered S-Al_2O_3 are 15% - 21% less than those of sintered S. The elongation at failure (10.1% ± 1.4%) of sintered S-Al_2O_3 is similar to that of sintered S. We believe that the dimensional shrinkage difference between the steel structure and the alumina support might affect the sintering of the steel structure and lead to weaker tensile properties. **Figure 6.4c** shows the SEM images of the tensile fracture surfaces of the sintered steel tensile bars. More SEM images of the tensile fracture surfaces at different magnification are presented in **Figure 6.S5**. The tensile fracture surface of the sintered S shows the shape and orientation of individual filaments at 45° relative to the tensile direction and orthogonal with the filaments from adjacent layers. Each individual filament is dense and the filaments from the same and the neighboring layers are fused together. The individual filament shape and orientation are recognizable but not very clear in the sintered S-Al_2O_3. The filaments in sintered S-Cu are completely fused together with the presence of copper, making a fully dense structure. The electrical conductivity of the sintered S-Al_2O_3 is (6.9 ± 3.4) × 10^5 S/m and the sintered S, (7.4 ± 0.4) × 10^5 S/m are similar (**Figure 6.4d**). The electrical conductivity of sintered S-Cu, (27.9 ± 4.2) × 10^5 S/m, is approximately four times higher than the value measure for the sintered S due to the presence of copper (**Figure 6.4d**). The properties of the sintered steel structures are summarized in **Table 6.S1**. The overall electrical and mechanical properties of the sintered S-Cu are superior to those of the sintered S. Sintered S-Al_2O_3 has comparable electrical properties, but slightly weaker mechanical properties compared to the sintered S.

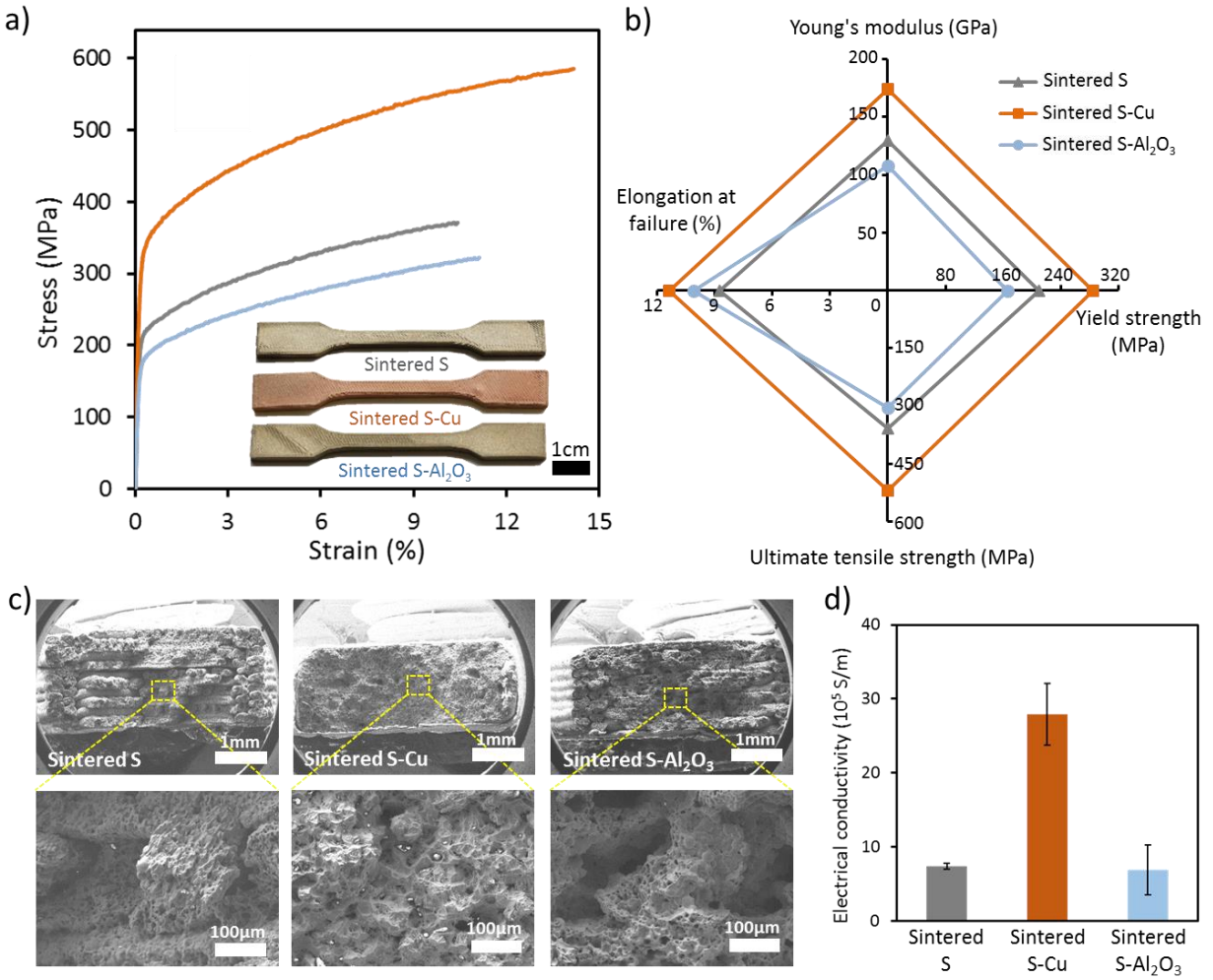

Figure 6.4 Electrical and mechanical characterizations of the sintered steel structures. (a) Typical tensile stress-strain curves of sintered steel structures and representative optical image of the different sintered steel tensile bars (inset). (b) Young's modulus, yield strength, ultimate tensile strength and elongation at failure of the sintered steel structures. (c) SEM images of the tensile fracture surfaces of the sintered steel structures. (d) Electrical conductivity of the sintered steel structures.

6.3 Conclusion

In conclusion, a multi-material direct ink writing method is developed to fabricate complex 3D metallic structures by printing removable supports using two different secondary materials. As a proof of concept, steel structures are fabricated through this method with the help of copper and alumina supports, respectively. The influence of the support materials on the steel structure is

investigated. The supports lead to no significant difference to the building structures on the dimensional shrinkage, surface roughness and porosity of the building structure. The copper support brings a hybrid metallic composition to the steel structure and improves its electrical conductivity by four times and stiffness by 34%. Although the alumina supports lower the stiffness of the building structure by 17%, it brings no contamination to the steel structure. It is worth mentioning that the support materials are not only limited to copper or alumina. Any desired alloying metal with a lower melting point than the building material can be the metal support material, e.g., zinc and aluminum. Any ceramic material that is physically and chemically stable during the thermal treatment can be the ceramic support materials such as tungsten carbide. The proposed method broadens the geometry possibilities of metallic 3D structures that DIW can create. It provides the metal additive manufacturing of medical implants, sensors and batteries featuring complex geometries a readily accessible choice.

6.4 Experimental Section

6.4.1 Ink preparation

The steel particles are stainless steel 316L with a spherical shape and a diameter less than 20μm. The copper particles are spherical and less than 20μm in diameter. The steel and copper particles are purchased from US Research Nanomaterials, Inc. The alumina particles are irregular in shape and less than 10μm in size (265497, Sigma-Aldrich). The SEM images of the three types of particles are presented in **Figure 6.S1**. The polymer binder solution is produced by adding 2g polylactic acid (PLA, 4032D, Natureworks LLC) to 8g dichloromethane (DCM, Sigma-Aldrich) and left to dissolve for 24 h to ensure homogenization. The steel, copper and alumina inks are prepared by mixing the corresponding particles with the polymer solution at a weight ratio of 3:1, 3:1, and 1.2:1, respectively, using a ball mill mixer (8000M Mixer/Mill, SPEX SamplePrep) for 15 min.

6.4.2 Multi-material DIW

The CAD model of the building structure is either designed in a computer aided design software (CATIA) or downloaded from internet (thingerverse.com). The support is generated where it is needed to hold building structure through a software, Simplify 3D (version 4.0). Both the building and support structures are converted into a G-code using Simplify 3D. Then the G-code is

converted into a point-to-point program that can be read by the JR Point software to control the 3-axis positioning robot (I&J2200-4, I&J Fisnar). The ink is loaded in a syringe (3mL, Nordson EFD) attached with a smooth-flow tapered nozzle (exit inner diameter = 250μm, Nordson EFD). DIW is performed using the positioning robot and pressure dispensing systems (HP-7X, Nordson EFD). The structures are deposited on a glass slide (PN 16004-422, VWR) at room temperature. All the structures in this work are deposited at a linear printing speed of 15mm/s and under an applied pressure of 0.7 - 1.2 MPa. The spacing between each layer is 80% of the nozzle inner diameter to compensate the solvent evaporation induced filament shrinkage and ensure tight bonding between the adjacent layers.

6.4.3 Post-deposition thermal treatments

The as-printed structures are thermal treated in a laboratory electric tubular furnace (59256-P-COM, Lindberg) on a ceramic substrate. To prevent oxidation, a gas flow (97.5% Ar and 2.5% H_2, flow rate = 5 L/min) is circulated inside the quartz tube. The temperature profile is presented in **Figure 6.1b**, wherein all the heating rates are 600°C/h and the cooling rate is 900°C/h.

6.4.4 Surface roughness measurement

The roughness of the top surface of the sintered steel structures is measured using a profilometer (SV-C4000, Mitutoyo) following the AISI standard in accordance with ASME B.46.1-2002. The measuring direction is perpendicular to the filament orientation. The sampling length of meso R_a is 7.5mm, while the sampling length of micro R_a is 0.1mm. Ten specimens are measured for each sample type.

6.4.5 Porosity analysis

The sintered steel scaffold is cut parallel to the *Z* direction to observe the vertical cross section. The sliced steel scaffold is sealed in a resin (EpoFix resin, Struers) block and the cross section is polished for observation under an optical microscope (Zeiss Axioplan EL-Einsatz). The porosity is determined using an image analysis software (ImageJ). The filament porosity is calculated as the ratio of void area inside the filament over the filament area. Ten cross sections of each sample are analyzed.

6.4.6 Electrical conductivity analysis

The electrical conductivity of the sintered steel structures is measured using the four-point probes method. A constant current of 1A is provided by a power supply (Agilent, E3633A). The voltage is acquired by a multimeter (HP, 3457A). Five specimens of each sample type are tested.

6.4.7 Tensile test and DIC

The samples are sintered steel tensile bars, of which the cross-section of the neck is ~3.6 × 1.8 mm. The tensile tests are carried out in a MTS Insight machine with a 50 kN load cell (MTS 569332-01) at a crosshead speed of 1 mm/min and using DIC to measure the strain of the tensile bars. The tensile bars are polished on both sides for a smooth surface. A thin layer of white acrylic spray paint (Ultra 2X spray paint, Painter's Touch) is applied on the surface. The speckle pattern (black dots of ~0.4mm) is painted on the white paint with a roller brush to ensure the tracking of displacement. The images of the sample are taken by two long range focus stereo microscopes at a frequency of 4Hz during the tensile test. The images are analyzed by VIC3D micro (Correlated solutions, version 7.2.4) and the strain is calculated by the displacement of the speckle pattern. The tensile test process with DIC measured strain showing on the sample is presented in **Video 6.S1**. Five specimens for each sample type are tested.

References

1. M. Cheng, Y. Jiang, W. Yao, Y. Yuan, R. Deivanayagam, T. Foroozan, Z. Huang, B. Song, R. Rojaee, T. Shokuhfar, Y. Pan, J. Lu, R. Shahbazian-Yassar, *Adv. Mater.* **2018**, 30, 1800615.
2. M. Finsterbusch, T. Danner, C. L. Tsai, S. Uhlenbruck, A. Latz, O. Guillon, *ACS Appl. Mater. Interfaces* **2018**, 10, 22329.
3. M. Elahinia, N. S. Moghaddam, M. T. Andani, A. Amerinatanzi, B. A. Bimber, R. F. Hamilton, *Prog. Mater. Sci.* **2016**, 83, 630.
4. S. A. Yavari, L. Loozen, F. L. Paganelli, S. Bakhshandeh, K. Lietaert, J. A. Groot, A. C. Fluit, C. H. E. Boel, J. Alblas, H. C. Vogely, H. Weinans, A. A. Zadpoor, *ACS Appl. Mater. Interfaces* **2016**, 8, 17080.
5. Y. S. Rim, S. H. Bae, H. Chen, N. D. Marco, Y. Yang, *Adv. Mater.* **2016**, 28, 4415.

6. L. Xu, S. R. Gutbrod, A. P. Bonifas, Y. Su, M. S. Sulkin, N. Lu, H. J. Chung, K. I. Jang, Z. Liu, M. Ying, C. Lu, R. C. Webb, J. S. Kim, J. I. Laughner, H. Cheng, Y. Liu, A. Ameen, J. W. Jeong, G. T. Kim, Y. Huang, I. R. Efimov, J. A. Rogers, *Nat. Commun.* **2014**, 5, 4329.
7. D. D. Gu, W. Meiners, K. Wissenbach, R. Poprawe, *Int. Mater. Rev.* **2012**, 57, 133.
8. D. Herzog, V. Seyda, E. Wycisk, C. Emmelmann, *Acta Mater.* **2016**, 117, 371.
9. J. H. Martin, B. D. Yahata, J. M. Hundley, J. A. Mayer, T. A. Schaedler, T. M. Pollock, *Nature* **2017**, 549, 365.
10. H. Gong, K. Rafi, H. Gu, G. D. J. Ram, T. Starr, B. Stucker, *Mater. Des.* **2015**, 86, 545.
11. E. O. Olakanmi, R. F. Cochrane, K. W. Dalgarno, *Prog. Mater. Sci.* **2015**, 74, 401.
12. R. Chou, J. Milligan, M. Paliwal, M. Brochu, *JOM* **2015**, 67, 590.
13. J. A. Lewis, *Adv. Funct. Mater.* **2006**, 16, 2193.
14. D. Therriault, S. R. White, J. A. Lewis, *Nat. Mater.* **2003**, 2, 265.
15. B. Y. Ahn, D. Shoji, C. J. Hansen, E. Hong, D. C. Dunand, J. A. Lewis, *Adv. Mater.* **2010**, 22, 2251.
16. A. E. Jakus, S. L. Taylor, N. R. Geisendorfer, D. C. Dunand, R. N. Shah, *Adv. Funct. Mater.* **2015**, 25, 6985.
17. C. Xu, A. Bouchemit, G. L'Espérance, L. L. Lebel, D. Therriault, *J. Mater. Chem. C* **2017**, 5, 10448.
18. C. Xu, Q. Wu, G. L'Espérance, L. L. Lebel, D. Therriault, *Mater. Des.* **2018**, 160, 262.
19. C. W. Ziemian, P. M. Crawn III, *Rapid Prototyp J* **2001**, 7, 138.
20. S. Waheed, J. M. Cabot, N. P. Macdonald, T. Lewis, R. M. Guijt, B. Paulland, M. C. Breadmore, *Lab Chip* **2016**, 16, 1993.
21. D. Peckner, I. M. Bernstein, *Handbook of Stainless Steels*, McGraw-Hill Book Company, New York, NY, USA, 1997.
22. J. R. Davis, *Copper and copper alloys*, ASM international, 2001.
23. P. Pradyot. *Handbook of inorganic chemicals*. McGraw-Hill, New York, USA, 2003.

6.5 Supporting information

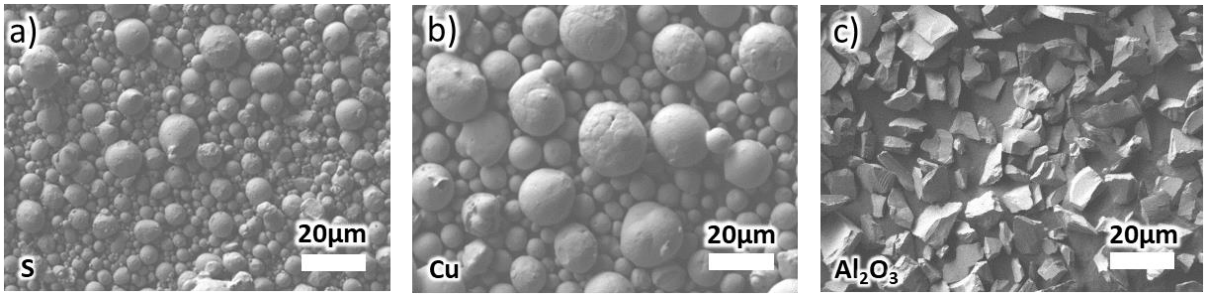

Figure 6.5 SEM images of a) steel, b) copper and c) alumina micro particles.

The steel and copper particles are spherical, while the alumina particles are irregular in shape featuring sharp corners.

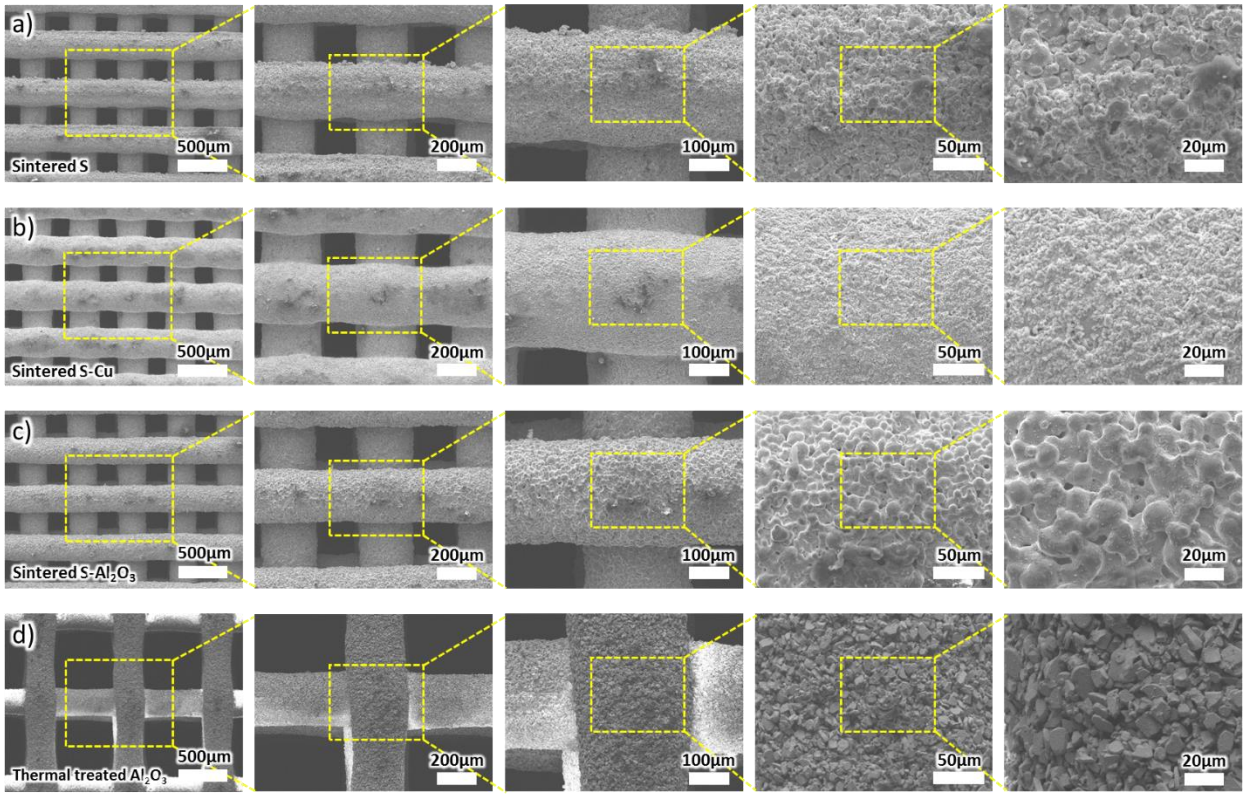

Figure 6.6 SEM images of the top layer of the sintered (thermally treated) scaffolds at different magnifications: (a) sintered S, (b) sintered S-Cu, (c) sintered S-Al_2O_3, and (d) thermal treated Al_2O_3.

The sintered (thermally treated) scaffolds preserve the original structure and the filaments are orderly structured. The metallic particles in the sintered steel structures (S, S-Cu and S- Al_2O_3) are fused, while the ceramic particles remain as individual particles and hold the structure by capillary forces.

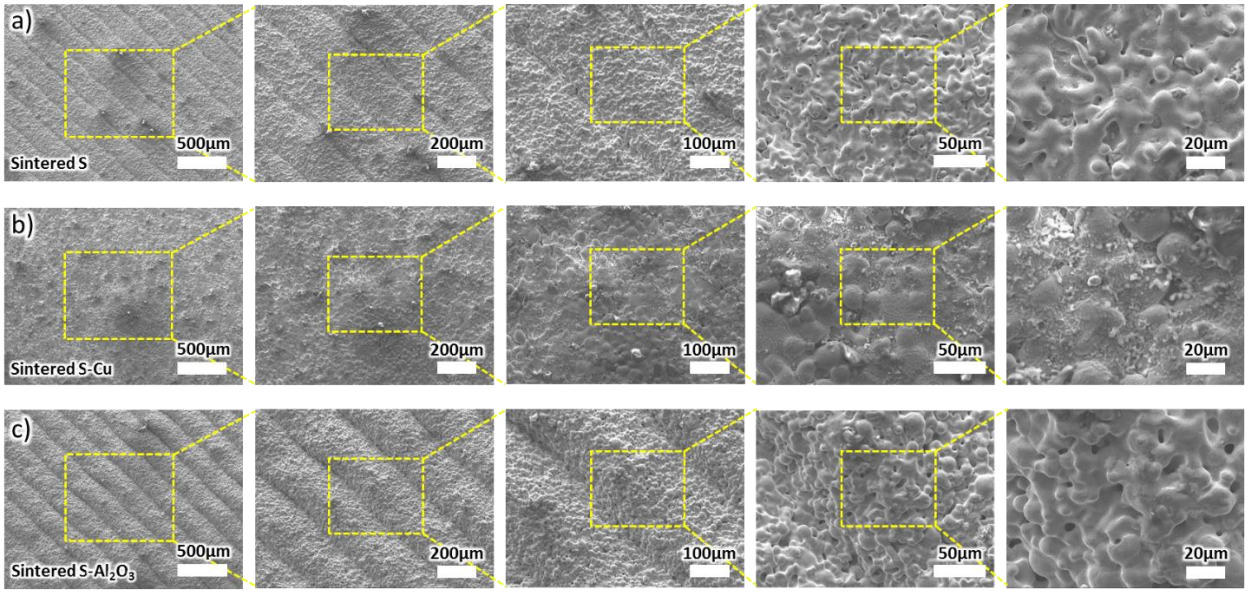

Figure 6.7 SEM images of the sintered steel tensile bars: (a) sintered S, (b) sintered S-Cu, and (c) sintered S-Al_2O_3

The sintered steel tensile bars are fully dense. The surface of sintered S-Cu is smoother than that of sintered S and sintered S-Al_2O_3.

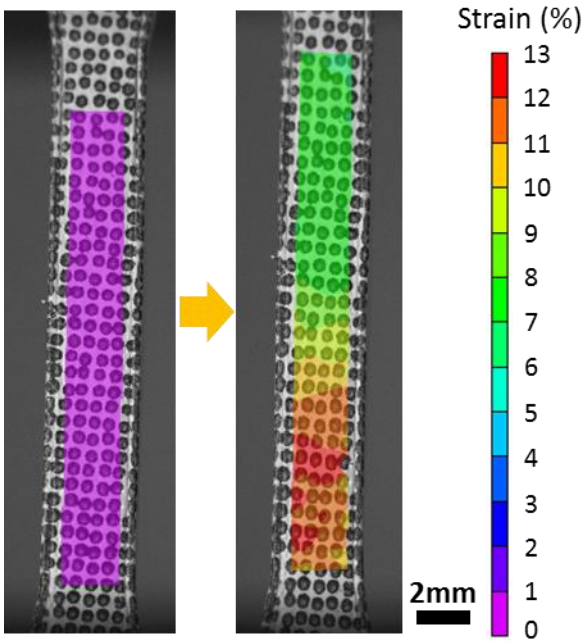

Figure 6.8 The strain distribution in the sintered steel tensile bars during tensile tests are measured through DIC. The tensile bar at the beginning of the tensile test (left) and close to failure (right).

Compared to extensometer, DIC can measure the strain more accurately. In addition, it is able to measure the strain distribution.

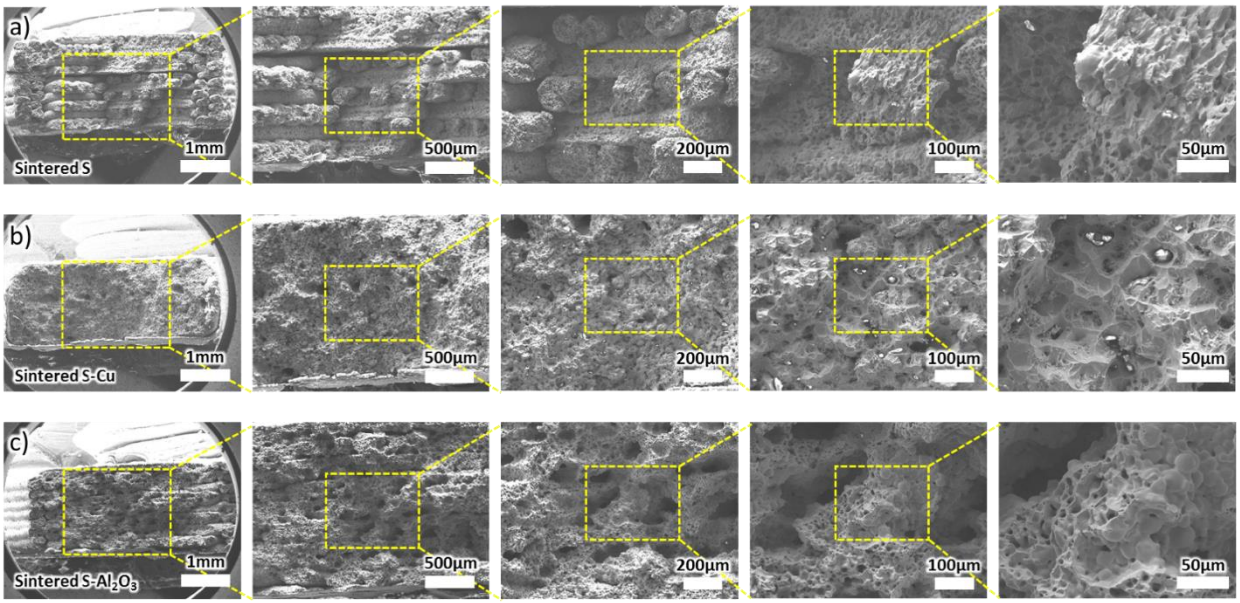

Figure 6.9 SEM images of the tensile fracture surfaces at different magnifications of (a) sintered S, (b) sintered S-Cu, and (c) sintered S-Al_2O_3.

The sintered S-Cu are denser and the filaments bond better than sintered S and S-Al_2O_3.

Table 6.1 Summary of the properties of the sintered steel structures

	Sintered S	Sintered S-Cu	Sintered S-Al_2O_3
Linear size reduction (%)	11.2 ± 0.9	10.7 ± 1.1	11.0 ± 1.3
Micro surface roughness *Ra* (μm)	2.5 ± 0.5	1.6 ± 0.3	4.1 ± 1.2
Macro surface roughness *Ra* (μm)	4.9 ± 2.9	6.3 ± 2.5	13.9 ± 2.2
Volume percentage of iron (%)	97.8 ± 0.3	87.2 ± 1.8	98.1 ± 0.6
Volume percentage of copper (%)	0	10.4 ± 1.3	0
Filament porosity (%)	2.2 ± 0.3	2.4 ± 0.8	1.9 ± 0.6
Pore size (μm)	2.5 ± 0.8	3.0 ± 0.9	2.6 ± 1.0
Electrical conductivity (10^5 S/m)	7.4 ± 0.4	27.9 ± 4.2	6.9 ± 3.4
Young's modulus (GPa)	130 ± 6	174 ± 10	108 ± 6
Yield tensile strength (MPa)	210 ± 4	284 ± 16	165 ± 8
Ultimate tensile strength (MPa)	359 ± 8	521 ± 57	304 ± 18
Elongation at break (%)	8.7 ± 1.2	11.3 ± 3.6	10.1 ± 1.4

Video 6.1 The tensile test process with DIC measured strain showing on the sample.

CHAPTER 7 GENERAL DISCUSSION

This chapter discusses unpublished experimental results and the research results of the three peer reviewed articles.

7.1 Discussions on unpublished results

7.1.1 Metallic ink recipe

The physical properties of the metallic inks play an important role in SC-DIW of metallic structures. The metallic ink is usually composed of metallic micro- or nano- particles, a thermoplastic polymer and a volatile solvent. Among different influencing parameters, the metallic concentration is a key parameter to the metallic ink. To find the optimum metallic ink recipe for SC-DIW, four highly alloyed steel / PLA / DCM inks of different metallic concentrations are prepared and used to build 3D periodic structures (scaffolds) through the proposed method for comparison on the printing quality. The metallic concentrations of the four inks from low to high are 47 vol.% (85 wt.%), 59 vol.% (90 wt.%), 75 vol.% (95 wt.%) and 90 vol.% (98 wt.%).

The low metallic concentrated ink contains a significant portion of polymer (PLA) and solvent (DCM). Upon extrusion, the solvent evaporates and the ink filaments shrink. Since 85 wt.% ink contains the most solvent, the scaffold printed using 85 wt.% ink exhibits severe shape deformation. When the metallic concentration increases, the extent of shape deformation in the as-printed structures decreases. No significant shape deformation is observed in the as-printed scaffolds made of 95 wt.% and 98 wt.% inks.

The high metallic concentration leads to a high viscosity of the ink. The viscous ink tends to clog the nozzle during the extrusion process, which hinders the printing process. Even though successfully extruded, the ink filament is very fragile and breaks. It causes defects in the fabricated structures and leads to lower mechanical properties. The clogging problem and filament breakage are observed only during the printing of the 98 wt.% ink.

The four scaffolds made of different ink concentrations are sintered for further comparison. During the debinding of the low metallic concentration ink, the metallic particles appear to be too far from each other, which leads to a risk that the structures collapse. The scaffolds printed using the 85 wt.% ink collapses during sintering, while the other three scaffolds are successfully sintered.

In summary, the utilization of a low metallic concentration leads to solvent evaporation induced shape deformation of the as-printed structures and a higher risk of collapsing during the post-deposition thermal treatments. On the other hand, the high very metallic concentration leads to the high viscosity of the ink, which causes defects in the fabricated structures. As a result, the 95 wt.% metallic concentration is selected as the optimum ink.

7.1.2 Printing parameters

The most important printing process parameters are nozzle tip diameter, printing speed and extrusion pressure. Firstly, the nozzle tip diameter determines the printing layer thickness and the printing resolution. Small nozzle tip diameter enables higher printing resolution, but lower volume building speed. As higher resolution is preferred over higher volume printing speed in this work, the smallest nozzle tip diameter as possible is chosen. The minimum nozzle tip diameter directly depends on the metallic particles size. To avoid nozzle clogging, the nozzle tip diameter can be as small as approximately ten times of the diameter of the metallic particles according to our experiments. The metallic particles used are spherical to reduce the friction forces and facilitate the extrusion. Secondly, the linear printing speed is set to be as high as possible for shorter manufacturing time. However, the solvent evaporation speed is a limiting factor to the printing speed. Whenever a new layer is deposited, it is recommended that the previous layer is mostly dried and rigid. Otherwise, the newly deposited ink filament will interfere with the previous layers, which reduces the printing quality. As a result, the printing speed is set to 15 mm/s as the maximum value for short manufacturing time. Finally, the extrusion pressure determines the extrusion speed. The extrusion speed should be equal to the motion of the substrate to guarantee a uniform ink filament.

7.2 Discussions on the published results

A novel metal additive manufacturing method was developed by combining SC-DIW and post-deposition thermal treatments. The simple setup for SC-DIW does not require expensive laser setups as laser-based metal AM techniques need. It dramatically reduces the cost for additive manufacturing of metallic structures. In addition to the conventional post-deposition thermal treatments (i.e., debinding and sintering), a secondary metallic infiltration was performed to further improve the mechanical and electrical performances of fabricated structures. An environment-friendly binder system was developed to make reusable and green metallic inks for SC-DIW. To

realize the fabrication of complex 3D metallic structures through SC-DIW, a multi-material SC-DIW method was developed to enable the printing of support structures, which can be removed after the thermal treatment. The results that achieve the specific objectives are discussed below:

(1) Fabricate 3D metallic structures through SC-DIW and post-deposition thermal treatments featuring high mechanical and electrical performances.

As illustrated in Chapter 4 (Article 1), a highly concentrated metallic ink (metallic load up to 98 wt.%) consisting of HAS microparticles, PLA and dichloromethane DCM was printed at room temperature through SC-DIW to build a metal-polymer composite 3D structures. The as-printed composite structure was thermally treated (i.e., debinding and sintering) in a furnace protected by a mixture of 97.5% Ar and 2.5% H_2 against oxidation, resulting in a pure metal structure preserving the original geometry. Various metallic structures, such as porous, interlocked and overhung structures, were fabricated to demonstrate the building capability of this method. Electrical conductivity measurements and tensile tests were carried out to investigate the electrical and mechanical properties of the fabricated structures. The electrical conductivity is 6.24×10^5 S/m, which is 45% of that of the bulk material. The tensile Young's modulus reaches up to 196 GPa, which is 89% of that of the bulk material.

(2) Develop a secondary metallic infiltration method for the thermally treated structures to further improve the mechanical and electrical performances.

Chapter 4 (Article 1) demonstrated a novel post-deposition thermal treatment, secondary metallic infiltration, to further improve the mechanical and electrical properties of the sintered structures. The sintered steel structure was porous featuring relatively lower electrical and mechanical properties compared to the bulk material. A piece of copper was placed on top of the sintered structures. They were heated over the melting temperature of copper protected by inner gas. The copper melted and infiltrated into the sintered steel structure driven by the capillary forces. The copper filled the pores in the sintered steel structures and improved their mechanical and electrical properties. The filament porosity is reduced from 12% to 0.2%. The ultimate tensile stress is improved from 485MPa to 511MPa. The electrical conductivity is increased by 2.3 times, from 6.24×10^5 S/m to 1.42×10^6 S/m.

(3) Develop a green and environment-friendly polymer solution system, which can be used for the metallic ink of SC-DIW.

The polymer solution system, PLA/DCM, is widely used in most metallic inks for SC-DIW. However, the organic solvent, DCM, is volatile and hazard, which is harmful to the environment. It is also harmful to the human beings. Long term inhaling DCM can cause cancer. As described in Chapter 5 (Article 2), a green and environment-friendly polymer solution system was developed. It consists of a biodegradable polymer: Chitosan, acetic acid and deionized water. Metallic particles can be mixed with this polymer solution to make the metallic ink for SC-DIW. Diverse metallic 3D structures (e.g., octopus, skull, pyramid and elliptical gears, etc.) were fabricated through SC-DIW using this environmental metallic ink. The electrical and mechanical properties of the fabricated structures are characterized and compared with those of the structures fabricated from PLA/DCM based metallic ink. The electrical conductivity is 9.4×10^5 S/m, which is improved by 52%. The Young's modulus reaches up to 205 GPa, which is increased by 5%.

(4) Develop a reusable metallic ink for SC-DIW.

The chitosan-based metallic ink presented in Chapter 5 (Article 2) is recyclable and can be reused for 3D printing. Any incorrectly built as-printed structures and scrap materials can be dissolved again in acetic acid and reused for SC-DIW. It demonstrated a very effective utilization of metallic materials and a sustainable metal AM method. However, as acetic acid and water evaporates much slower than DCM at ambient conditions, it requires additional setup to the increase the evaporation speed during printing. It also restricts the printing speed and resolution.

(5) Develop a multi-material SC-DIW method to fabricate complex 3D metallic structures by creating removable support structures using a secondary material.

Polymeric SC-DIW can print complex 3D structures featuring large overhangs or lengthy bridges by building a support underneath them to hold the structures. Once the printing is completed, the support structure is removed. But it does not work for metallic SC-DIW, where a post-deposition thermal treatment is performed. If the support is removed prior to the thermal treatment, when the polymer binder is removed while the metal particles are not sintered yet, the overhang features will fall in apart due to lack of support. While, if the support is not removed before the thermal treatment, the support and the building structure will fuse together and become inseparable after the thermal

treatment, as they are printed from the same material. To solve this problem, a multi-material SC-DIW method was developed to fabricate complex 3D metallic structures by creating removable support structures using a secondary material, as introduced in Chapter 6 (Article 3). There are two types of support materials: copper and alumina. They can be selected according to the desired properties of the fabricated structure. The copper support is melted and completely infiltrates into the building structure during the thermal treatment. It improves the electrical conductivity of the fabricated steel structure by four times and the stiffness by 34%. The alumina support is physically and chemically stable during the thermal treatment, bringing no contamination to the building structure. It can be easily removed by hand after the thermal treatment.

CHAPTER 8 CONCLUSION AND RECOMMENDATIONS

8.1 Conclusion

In this dissertation, a novel, low-cost and practical solvent cast direct ink writing (SC-DIW) method was established to fabricate 3D metallic structures. The dimensional shrinkage induced by thermal treatment, surface roughness, filament porosity, pore size, electrical conductivity and tensile properties of the fabricated structures were characterized. A reusable and environment-friendly metallic ink was developed for SC-DIW. It enables SC-DIW of metallic structures to be performed with a low environmental impact and an effective utilization of metallic materials. In addition, multi-material SC-DIW was investigated to enable the fabrication of complex 3D metallic structures featuring overhangs by printing removable support structures using a secondary material. The following conclusions are drawn from this work:

- The metallic ink made up of steel micro particles, PLA and DCM can be printed through SC-DIW at room temperature to build metal-polymer composite structures. The as-printed structures can be turned into pure metal structures through thermal treatments. The fabricated steel structures show high mechanical and electrical performances, e.g., an electrical conductivity of 6.24×10^5 S/m and a tensile Young's modulus of 196 GPa.
- The volume metallic load in the metallic ink is an important parameter. Low metallic concentration leads the structures to collapse during the post-deposition thermal treatments. Whereas, high metallic concentration results in a high viscosity of the metallic ink. The metallic ink clogs the micro nozzle and stops the printing process. Based on the research results, steel particles loaded in PLA/DCM solution ranging 47 – 90 vol.% make a printable metallic ink for SC-DIW. The 95 vol.% ink makes a reasonable balance between 3D printing and post-deposition thermal treatments.
- Copper infiltration can readily fill the pores in the sintered steel structures driven by the capillary forces. If the amount of copper is carefully adjusted, the copper will only fill the pores created by sintering, but not the structural pores. Copper infiltration improves the electrical conductivity of the sintered steel structures by 2.3 times and the ultimate tensile stress by 5.4%.
- The water soluble polymer solution, consisting of chitosan, acetic acid and deionized water, can be mixed with metallic particles to make a reusable and green metallic ink for SC-DIW.

The fabricated structures have comparable electrical and mechanical performances as the structures fabricated from conventional (i.e., PLA/DCM based) metallic ink.

- Complex 3D steel structures with overhang features can be fabricated through a multi-material SC-DIW method by printing removable support using a secondary material (copper or alumina). The copper can improve the electrical conductivity of the fabricated steel structure by four times and the stiffness by 34%. The alumina support is physically and chemically stable during the thermal treatment, bringing no contamination to the building structure.

8.2 Recommendations

The following aspects are recommended for more exploration in future work:

- The modeling and simulation of the SC-DIW process and post-deposition thermal treatments should be conducted, which could be helpful in deeply understanding the process and the microstructure variations during the thermal treatments.
- Diverse metallic materials, such as titanium, aluminum, zinc and nickel, should be printed through the presented SC-DIW method to demonstrate its material compatibility. The mechanical and electrical properties should be characterized and compared with the bulk materials, respectively.
- The relations between the sintering temperature and metallic particles size should be investigated, which could help to predict the temperature profile of the thermal treatment for a specific particle size.
- The microstructures of the fabricated parts should be characterized at every stage of the thermal treatments, which could provide a better understanding of the sintering and secondary metallic infiltration processes.
- More applications featuring complex geometries, high mechanical and electrical performances should be explored for the metallic structures fabricated through the presented SC-DIW method.
- The metallic particle size determines the printing resolution. The nozzle tip diameter can be as small as approximately ten times of the metallic particle parameter. For example, if spherical metallic particles with an average diameter of 20 μm are used, the resolution (the nozzle tip diameter) can be as small as 200 μm. To achieve higher

resolution, metallic ions solution can be used to replace metallic polymer solution. The nozzle tip with a diameter of tens of nanometers could be used for higher resolution. The metallic ions solution can be turned into metallic structures through the thermal treatments.

- More theoretical calculations should be included in this research for the deeper understanding of the processes, including the kinetic energy of the metallic atoms during the sintering, the shear thinning phenomena, the viscosity of the metallic ink, the radius curvature of sintering metallic particles and the capillary forces during copper infiltration.

REFERENCES

[1] Elahinia, M., Moghaddam, N. S., Andani, M. T., Amerinatanzi, A., Bimber, B. A., & Hamilton, R. F. (2016). Fabrication of NiTi through additive manufacturing: A review. *Progress in Materials Science*, *83*, 630-663.

[2] Cheng, M., Jiang, Y., Yao, W., Yuan, Y., Deivanayagam, R., Foroozan, T., Huang, Z., Song, B., Rojaee, R., Shokuhfar, T. & Pan, Y. (2018). Elevated-Temperature 3D Printing of Hybrid Solid-State Electrolyte for Li-Ion Batteries. *Advanced Materials*, *30*(39), 1800615.

[3] Ahn, B.Y., Duoss, E.B., Motala, M.J., Guo, X., Park, S.I., Xiong, Y., Yoon, J., Nuzzo, R.G., Rogers, J.A. & Lewis, J.A. (2009). Omnidirectional printing of flexible, stretchable, and spanning silver microelectrodes. *Science*, *323*(5921), 1590-1593.

[4] Rim, Y. S., Bae, S. H., Chen, H., De Marco, N., & Yang, Y. (2016). Recent progress in materials and devices toward printable and flexible sensors. *Advanced Materials*, *28*(22), 4415-4440.

[5] Van Noort, R. (2012). The future of dental devices is digital. *Dental Materials*, *28*(1), 3-12.

[6] Mueller, B. (2012). Additive manufacturing technologies–Rapid prototyping to direct digital manufacturing. *Assembly Automation*, *32*(2).

[7] Herzog, D., Seyda, V., Wycisk, E., & Emmelmann, C. (2016). Additive manufacturing of metals. *Acta Materialia*, *117*, 371-392.

[8] Martin, J. H., Yahata, B. D., Hundley, J. M., Mayer, J. A., Schaedler, T. A., & Pollock, T. M. (2017). 3D printing of high-strength aluminium alloys. *Nature*, *549*(7672), 365.

[9] Gong, H., Rafi, K., Gu, H., Ram, G. J., Starr, T., & Stucker, B. (2015). Influence of defects on mechanical properties of Ti–6Al–4 V components produced by selective laser melting and electron beam melting. *Materials & Design*, *86*, 545-554.

[10] Olakanmi, E. O. T., Cochrane, R. F., & Dalgarno, K. W. (2015). A review on selective laser sintering/melting (SLS/SLM) of aluminium alloy powders: Processing, microstructure, and properties. *Progress in Materials Science*, *74*, 401-477.

[11] Chou, R., Milligan, J., Paliwal, M., & Brochu, M. (2015). Additive manufacturing of Al-12Si alloy via pulsed selective laser melting. *JOM*, *67*(3), 590-596.

[12] Lewis, J. A. (2006). Direct ink writing of 3D functional materials. *Advanced Functional Materials*, *16*(17), 2193-2204.

[13] Hong, E., Ahn, B. Y., Shoji, D., Lewis, J. A., & Dunand, D. C. (2011). Microstructure and mechanical properties of reticulated titanium scrolls. *Advanced Engineering Materials*, *13*(12), 1122-1127.

[14] Taylor, S. L., Jakus, A. E., Shah, R. N., & Dunand, D. C. (2017). Iron and Nickel Cellular Structures by Sintering of 3D-Printed Oxide or Metallic Particle Inks. *Advanced Engineering Materials*, *19*(11), 1600365.

[15] Hu, J., & Yu, M. F. (2010). Meniscus-confined three-dimensional electrodeposition for direct writing of wire bonds. *Science*, *329*(5989), 313-316.

[16] Seol, S. K., Kim, D., Lee, S., Kim, J. H., Chang, W. S., & Kim, J. T. (2015). Electrodeposition-based 3D printing of metallic microarchitectures with controlled internal structures. *Small*, *11*(32), 3896-3902.

[17] Lee, D. Y., Shin, Y. S., Park, S. E., Yu, T. U., & Hwang, J. (2007). Electrohydrodynamic printing of silver nanoparticles by using a focused nanocolloid jet. *Applied Physics Letters*, *90*(8), 081905.

[18] Gupta, A., Seifalian, A. M., Ahmad, Z., Edirisinghe, M. J., & Winslet, M. C. (2007). Novel electrohydrodynamic printing of nanocomposite biopolymer scaffolds. *Journal of bioactive and compatible polymers*, *22*(3), 265-280.

[19] Hirt, L., Ihle, S., Pan, Z., Dorwling-Carter, L., Reiser, A., Wheeler, J. M., Spolenak, R., Vörös, J. & Zambelli, T. (2016). Template-free 3D microprinting of metals using a force-controlled nanopipette for layer-by-layer electrodeposition. *Advanced materials*, *28*(12), 2311-2315.

[20] Momotenko, D., Page, A., Adobes-Vidal, M., & Unwin, P. R. (2016). Write–Read 3D Patterning with a Dual-Channel Nanopipette. *ACS nano*, *10*(9), 8871-8878.

[21] Kruth, J. P., Froyen, L., Van Vaerenbergh, J., Mercelis, P., Rombouts, M., & Lauwers, B. (2004). Selective laser melting of iron-based powder. *Journal of materials processing technology*, *149*(1-3), 616-622.

[22] Kruth, J. P., Mercelis, P., Van Vaerenbergh, J., Froyen, L., & Rombouts, M. (2005). Binding mechanisms in selective laser sintering and selective laser melting. *Rapid prototyping journal*, *11*(1), 26-36.

[23] Vandenbroucke, B., & Kruth, J. P. (2007). Selective laser melting of biocompatible metals for rapid manufacturing of medical parts. *Rapid Prototyping Journal*, *13*(4), 196-203.

[24] Materialgeeza, retrieved from https://en.wikipedia.org/wiki/Selective_laser_melting#/media/File:Selective_laser_melting_system_schematic.jpg

[25] SLM solutions, Inc. Retrieved from https://slm-solutions.com/sites/default/files/downloads/101en171016-01-004-slm500_web.pdf

[26] Bossuyt, T., & Fournier, S. A Few Basic Design Rules for Metal 3D Printed Parts, Retrieved from https://medium.com/@makernest/a-few-basic-design-rules-for-metal-3d-printed-parts-1eec4980bb24

[27] Truscott, M., De Beer, D., Vicatos, G., Hosking, K., Barnard, L., Booysen, G., & Ian Campbell, R. (2007). Using RP to promote collaborative design of customised medical implants. *Rapid Prototyping Journal*, *13*(2), 107-114.

[28] Zhou, X., Wang, D., Liu, X., Zhang, D., Qu, S., Ma, J., London, G., Shen, Z. & Liu, W. (2015). 3D-imaging of selective laser melting defects in a Co–Cr–Mo alloy by synchrotron radiation micro-CT. *Acta Materialia*, *98*, 1-16.

[29] Gong, H., Rafi, K., Gu, H., Starr, T., & Stucker, B. (2014). Analysis of defect generation in Ti–6Al–4V parts made using powder bed fusion additive manufacturing processes. *Additive Manufacturing*, *1*, 87-98.

[30] Vilaro, T., Colin, C., & Bartout, J. D. (2011). As-fabricated and heat-treated microstructures of the Ti-6Al-4V alloy processed by selective laser melting. *Metallurgical and materials transactions A*, *42*(10), 3190-3199.

[31] Seagle, S. R., Martin, R. L., & Bertea, O. (1962). Electron-Beam Melting. *JOM*, *14*(11), 812-820.

[32] Agarwala, M., Bourell, D., Beaman, J., Marcus, H., & Barlow, J. (1995). Direct selective laser sintering of metals. *Rapid Prototyping Journal*, *1*(1), 26-36.

[33] Parthasarathy, J., Starly, B., Raman, S., & Christensen, A. (2010). Mechanical evaluation of porous titanium (Ti6Al4V) structures with electron beam melting (EBM). *Journal of the mechanical behavior of biomedical materials*, *3*(3), 249-259.

[34] Arcam EBM, Inc. Retrieved from http://www.arcam.com/wp-content/uploads/arcameb m-corp-brochure-fnlv3.pdf

[35] Harrysson, O. L., Cansizoglu, O., Marcellin-Little, D. J., Cormier, D. R., & West II, H. A. (2008). Direct metal fabrication of titanium implants with tailored materials and

mechanical properties using electron beam melting technology. *Materials Science and Engineering: C*, *28*(3), 366-373.

[36] Murr, L. E., Gaytan, S. M., Ceylan, A., Martinez, E., Martinez, J. L., Hernandez, D. H., Machado, B.I., Ramirez, D.A., Medina, F., Collins, S. & Wicker, R. B. (2010). Characterization of titanium aluminide alloy components fabricated by additive manufacturing using electron beam melting. *Acta materialia*, *58*(5), 1887-1894.

[37] Biamino, S., Penna, A., Ackelid, U., Sabbadini, S., Tassa, O., Fino, P., Pavese, M., Gennaro, P. & Badini, C. (2011). Electron beam melting of Ti–48Al–2Cr–2Nb alloy: Microstructure and mechanical properties investigation. *Intermetallics*, *19*(6), 776-781.

[38] Arcam EBM, Inc. Retrieved from http://www.arcam.com/technology/electron-beam-melting/hardware/

[39] Petch, M. Retrieved from https://www.autodesk.com/redshift/electron-beam-melting/

[40] 3D Print Expo, Retrieved from https://3d-expo.ru/en/article/elektronno-luchevaya-plavka-kak-promishlennaya-additivnaya-tehnologiya-78927

[41] Dinda, G. P., Dasgupta, A. K., & Mazumder, J. (2009). Laser aided direct metal deposition of Inconel 625 superalloy: Microstructural evolution and thermal stability. *Materials Science and Engineering: A*, *509*(1-2), 98-104.

[42] Zhang, K., Liu, W., & Shang, X. (2007). Research on the processing experiments of laser metal deposition shaping. *Optics & Laser Technology*, *39*(3), 549-557.

[43] Lewis, G. K., & Schlienger, E. (2000). Practical considerations and capabilities for laser assisted direct metal deposition. *Materials & Design*, *21*(4), 417-423.

[44] Nowotny, S., Scharek, S., Beyer, E., & Richter, K. H. (2007). Laser beam build-up welding: precision in repair, surface cladding, and direct 3D metal deposition. *Journal of Thermal Spray Technology*, *16*(3), 344-348.

[45] Graf, B., Gumenyuk, A., & Rethmeier, M. (2012). Laser metal deposition as repair technology for stainless steel and titanium alloys. *Physics Procedia*, *39*, 376-381.

[46] Frazier, W. E. (2014). Metal additive manufacturing: a review. *Journal of Materials Engineering and Performance*, *23*(6), 1917-1928.

[47] Graf, B., Ammer, S., Gumenyuk, A., & Rethmeier, M. (2013). Design of experiments for laser metal deposition in maintenance, repair and overhaul applications. *Procedia CIRP*, *11*, 245-248.

[48] Retrieved from http://www.fabricatingandmetalworking.com/2016/07/additive-manufacturing-making-sense-laser-metal-deposition-3d-printing/

[49] Mahamood, R. M., & Akinlabi, E. T. (2015). Laser metal deposition of functionally graded Ti6Al4V/TiC. *Materials & Design*, *84*, 402-410.

[50] Zhang, K., Wang, S., Liu, W., & Shang, X. (2014). Characterization of stainless steel parts by laser metal deposition shaping. *Materials & Design*, *55*, 104-119.

[51] Pinkerton, A. J., Wang, W., & Li, L. (2008). Component repair using laser direct metal deposition. *Proceedings of the Institution of Mechanical Engineers, Part B: Journal of Engineering Manufacture*, *222*(7), 827-836.

[52] Optomec Inc., retrieved from https://www.optomec.com/wp-content/uploads/2014/04/LENS_850-R_Web_0716.pdf

[53] Qi, H., Mazumder, J., & Ki, H. (2006). Numerical simulation of heat transfer and fluid flow in coaxial laser cladding process for direct metal deposition. *Journal of applied physics*, *100*(2), 024903.

[54] Gasser, A., Backes, G., Kelbassa, I., Weisheit, A., & Wissenbach, K. (2010). Laser Additive Manufacturing: Laser Metal Deposition (LMD) and Selective Laser Melting (SLM) in Turbo-Engine Applications. *Laser Technik Journal*, *7*(2), 58-63.

[55] Gaytan, S. M., Cadena, M. A., Karim, H., Delfin, D., Lin, Y., Espalin, D., MacDonald, E. & Wicker, R. B. (2015). Fabrication of barium titanate by binder jetting additive manufacturing technology. *Ceramics International*, *41*(5), 6610-6619.

[56] Gonzalez, J. A., Mireles, J., Lin, Y., & Wicker, R. B. (2016). Characterization of ceramic components fabricated using binder jetting additive manufacturing technology. *Ceramics International*, *42*(9), 10559-10564.

[57] Bai, Y., & Williams, C. B. (2015). An exploration of binder jetting of copper. *Rapid Prototyping Journal*, *21*(2), 177-185.

[58] ExOne Inc., retrieved from https://www.exone.com/

[59] Gokuldoss, P. K., Kolla, S., & Eckert, J. (2017). Additive manufacturing processes: Selective laser melting, electron beam melting and binder jetting—Selection guidelines. *Materials*, *10*(6), 672.

[60] Bai, Y., Wagner, G., & Williams, C. B. (2015). Effect of bimodal powder mixture on powder packing density and sintered density in binder jetting of metals. In *2015 Annual International Solid Freeform Fabrication Symposium* (Vol. 62, pp. 758-771).

[61] Paranthaman, M. P., Shafer, C. S., Elliott, A. M., Siddel, D. H., McGuire, M. A., Springfield, R. M., Martin, J., Fredette, R. & Ormerod, J. (2016). Binder Jetting: A Novel NdFeB bonded magnet fabrication process. *Jom*, *68*(7), 1978-1982.

[62] Lee, J. Y., An, J., & Chua, C. K. (2017). Fundamentals and applications of 3D printing for novel materials. *Applied Materials Today*, *7*, 120-133.

[63] Gibson, I., Rosen, D., & Stucker, B. (2015). Binder jetting. In *Additive Manufacturing Technologies* (pp. 205-218). Springer, New York, NY.

[64] Sculpteo, retrieved from https://www.sculpteo.com/en/materials/binder-jetting-material/

[65] 3D printing media network, retrieved from https://www.3dprintingmedia.network/hoganas-installs-first-external-p2000-metal-binder-jetting-3d-printer-cetim/

[66] Melchels, F. P., Feijen, J., & Grijpma, D. W. (2010). A review on stereolithography and its applications in biomedical engineering. *Biomaterials*, *31*(24), 6121-6130.

[67] Zhang, X., Jiang, X. N., & Sun, C. (1999). Micro-stereolithography of polymeric and ceramic microstructures. *Sensors and Actuators A: Physical*, *77*(2), 149-156.

[68] Griffith, M. L., & Halloran, J. W. (1996). Freeform fabrication of ceramics via stereolithography. *Journal of the American Ceramic Society*, *79*(10), 2601-2608.

[69] Hemmer, W., Focke, M., Wantke, F., Götz, M., & Jarisch, R. (1996). Allergic contact dermatitis to artificial fingernails prepared from UV light-cured acrylates. *Journal of the American Academy of Dermatology*, *35*(3), 377-380.

[70] Goss, B. (2002). Bonding glass and other substrates with UV curing adhesives. *International Journal of Adhesion and Adhesives*, *22*(5), 405-408.

[71] Lan, P. T., Chou, S. Y., Chen, L. L., & Gemmill, D. (1997). Determining fabrication orientations for rapid prototyping with stereolithography apparatus. *Computer-Aided Design*, *29*(1), 53-62.

[72] Bartolo, P. J., & Gaspar, J. (2008). Metal filled resin for stereolithography metal part. *CIRP Annals-Manufacturing Technology*, *57*(1), 235-238.

[73] Lee, J. W., Lee, I. H., & Cho, D. W. (2006). Development of micro-stereolithography technology using metal powder. *Microelectronic engineering*, *83*(4-9), 1253-1256.

[74] Yarlagadda, P. K., Ilyas, I. P., & Christodoulou, P. (2001). Development of rapid tooling for sheet metal drawing using nickel electroforming and stereolithography processes. *Journal of Materials Processing Technology*, *111*(1-3), 286-294.

[75] Custompart.net. Retrieved from https://www.custompartnet.com/wu/stereolithography

[76] Lee, J. W., Lee, I. H., & Cho, D. W. (2006). Development of micro-stereolithography technology using metal powder. *Microelectronic engineering*, *83*(4-9), 1253-1256.

[77] Attanasio, D. C., Hopkinson, N., Kehrberger, R., Sridhar, A., & Witt, G. (2006). Application and modelling of hybrid stereolithography injection mould tooling. *Virtual and Physical Prototyping*, *1*(3), 197-206.

[78] Formlabs Inc., retrieved from https://formlabs.com/3d-printers/form-2/

[79] Corcione, C. E., Greco, A., & Maffezzoli, A. (2006). Temperature evolution during stereolithography building with a commercial epoxy resin. *Polymer Engineering & Science*, *46*(4), 493-502.

[80] Melchels, F. P., Feijen, J., & Grijpma, D. W. (2010). A review on stereolithography and its applications in biomedical engineering. *Biomaterials*, *31*(24), 6121-6130.

[81] Bens, A., Seitz, H., Bermes, G., Emons, M., Pansky, A., Roitzheim, B., ... & Tille, C. (2007). Non-toxic flexible photopolymers for medical stereolithography technology. *Rapid Prototyping Journal*, *13*(1), 38-47.

[82] Lewis, J. A., Smay, J. E., Stuecker, J., & Cesarano, J. (2006). Direct ink writing of three-dimensional ceramic structures. *Journal of the American Ceramic Society*, *89*(12), 3599-3609.

[83] Fu, Q., Saiz, E., & Tomsia, A. P. (2011). Direct ink writing of highly porous and strong glass scaffolds for load-bearing bone defects repair and regeneration. *Acta biomaterialia*, *7*(10), 3547-3554.

[84] Lewis, J. A., & Gratson, G. M. (2004). Direct writing in three dimensions. *Materials today*, *7*(7-8), 32-39.

[85] Costakis Jr, W. J., Rueschhoff, L. M., Diaz-Cano, A. I., Youngblood, J. P., & Trice, R. W. (2016). Additive manufacturing of boron carbide via continuous filament direct ink writing of aqueous ceramic suspensions. *Journal of the European Ceramic Society*, *36*(14), 3249-3256.

[86] Lebel, L. L., Aissa, B., Khakani, M. A. E., & Therriault, D. (2010). Ultraviolet-Assisted Direct-Write Fabrication of Carbon Nanotube/Polymer Nanocomposite Microcoils. *Advanced Materials*, *22*(5), 592-596.

[87] Walker, S. B., & Lewis, J. A. (2012). Reactive silver inks for patterning high-conductivity features at mild temperatures. *Journal of the American Chemical Society*, *134*(3), 1419-1421.

[88] Han, J. W., Kim, B., Li, J., & Meyyappan, M. (2014). Carbon nanotube ink for writing on cellulose paper. *Materials Research Bulletin*, *50*, 249-253.

[89] Huang, S., Zhao, C., Pan, W., Cui, Y., & Wu, H. (2015). Direct writing of half-meter long CNT based fiber for flexible electronics. *Nano letters*, *15*(3), 1609-1614.

[90] Therriault, D., Shepherd, R. F., White, S. R., & Lewis, J. A. (2005). Fugitive Inks for Direct-Write Assembly of Three-Dimensional Microvascular Networks. *Advanced Materials*, *17*(4), 395-399.

[91] Smay, J. E., Gratson, G. M., Shepherd, R. F., Cesarano III, J., & Lewis, J. A. (2002). Directed colloidal assembly of 3D periodic structures. *Advanced Materials*, *14*(18), 1279-1283.

[92] Therriault, D., Shepherd, R. F., White, S. R., & Lewis, J. A. (2005). Fugitive inks for direct-write assembly of three-dimensional microvascular networks. *Advanced Materials*, *17*(4), 395-399.

[93] Farahani, R. D., Chizari, K., & Therriault, D. (2014). Three-dimensional printing of freeform helical microstructures: a review. *Nanoscale*, *6*(18), 10470-10485.

[94] Chen, R., retrieved from https://www.llnl.gov/news/3d-printed-aerogels-improve-energy-storage

[95] Guo, S. Z., Gosselin, F., Guerin, N., Lanouette, A. M., Heuzey, M. C., & Therriault, D. (2013). Solvent-cast three-dimensional printing of multifunctional microsystems. *Small*, *9*(24), 4118-4122.

[96] Klein, F., Richter, B., Striebel, T., Franz, C. M., Freymann, G. V., Wegener, M., & Bastmeyer, M. (2011). Two-component polymer scaffolds for controlled three-dimensional cell culture. *Advanced materials*, *23*(11), 1341-1345.

[97] Berry, Scott M., et al. "Endothelial cell scaffolds generated by 3D direct writing of biodegradable polymer microfibers." Biomaterials 32.7 (2011): 1872-1879.

[98] Leong, T. G., Zarafshar, A. M., & Gracias, D. H. (2010). Three-dimensional fabrication at small size scales. *Small*, *6*(7), 792-806.

[99] Farahani, R. D., Dalir, H., Le Borgne, V., Gautier, L. A., El Khakani, M. A., Lévesque, M., & Therriault, D. (2012). Direct-write fabrication of freestanding nanocomposite strain sensors. *Nanotechnology*, *23*(8), 085502.

[100] Xiao, X., Yuan, L., Zhong, J., Ding, T., Liu, Y., Cai, Z., Rong, Y., Han, H., Zhou, J. & Wang, Z. L. (2011). High-strain sensors based on ZnO nanowire/polystyrene hybridized flexible films. *Advanced materials*, *23*(45), 5440-5444.

[101] Yeom, J., & Shannon, M. A. (2010). Detachment Lithography of Photosensitive Polymers: A Route to Fabricating Three-Dimensional Structures. *Advanced Functional Materials*, *20*(2), 289-295.

[102] Boparai, K. S., Singh, R., & Singh, H. (2016). Development of rapid tooling using fused deposition modeling: a review. *Rapid Prototyping Journal*, *22*(2), 281-299.

[103] Tsouknidas, A. (2011). Friction induced wear of rapid prototyping generated materials: a review. *Advances in Tribology*, *2011*.

[104] MakerBot Inc., retrieved from https://www.makerbot.com/3d-printers/

[105] Yamada, A., Niikura, F., & Ikuta, K. (2008). A three-dimensional microfabrication system for biodegradable polymers with high resolution and biocompatibility. *Journal of Micromechanics and Microengineering*, *18*(2), 025035.

[106] Allahverdi, M., Danforth, S. C., Jafari, M., & Safari, A. (2001). Processing of advanced electroceramic components by fused deposition technique. *Journal of the European Ceramic Society*, *21*(10-11), 1485-1490.

[107] Crump, S. S. (1992). *U.S. Patent No. 5,121,329*. Washington, DC: U.S. Patent and Trademark Office.

[108] Safari, A. (2001). Processing of advanced electroceramic components by fused deposition technique. *Ferroelectrics*, *263*(1), 45-54.

[109] Kopinke, F. D., Remmler, M., & Mackenzie, K. (1996). Thermal decomposition of biodegradable polyesters—I: Poly (β-hydroxybutyric acid). *Polymer Degradation and stability*, *52*(1), 25-38.

[110] Gibson, M. A., Mykulowycz, N. M., Shim, J., Fontana, R., Schmitt, P., Roberts, A., Ketkaew, J., Shao, L., Chen, W., Bordeenithikasem, P. & Myerberg, J. S. (2018). 3D

printing metals like thermoplastics: Fused filament fabrication of metallic glasses. *Materials Today*, *21*(7), 697-702.

[111] Barry III, R. A., Shepherd, R. F., Hanson, J. N., Nuzzo, R. G., Wiltzius, P., & Lewis, J. A. (2009). Direct-write assembly of 3D hydrogel scaffolds for guided cell growth. *Advanced materials*, *21*(23), 2407-2410.

[112] Guo, S. Z., Heuzey, M. C., & Therriault, D. (2014). Properties of polylactide inks for solvent-cast printing of three-dimensional freeform microstructures. *Langmuir*, *30*(4), 1142-1150.

[113] Xu, C., Wu, Q., L'Espérance, G., Lebel, L. L., & Therriault, D. (2018). Environment-friendly and reusable ink for 3D printing of metallic structures. *Materials & Design*, *160*, 262-269.

[114] Ahn, B. Y., Shoji, D., Hansen, C. J., Hong, E., Dunand, D. C., & Lewis, J. A. (2010). Printed origami structures. *Advanced Materials*, *22*(20), 2251-2254.

[115] Jakus, A. E., Taylor, S. L., Geisendorfer, N. R., Dunand, D. C., & Shah, R. N. (2015). Metallic architectures from 3D-printed powder-based liquid inks. *Advanced Functional Materials*, *25*(45), 6985-6995.

[116] Skylar-Scott, M. A., Gunasekaran, S., & Lewis, J. A. (2016). Laser-assisted direct ink writing of planar and 3D metal architectures. *Proceedings of the National Academy of Sciences*, *113*(22), 6137-6142.

[117] Antusch, S., Norajitra, P., Piotter, V., Ritzhaupt-Kleissl, H. J., & Spatafora, L. (2011). Powder Injection Molding–An innovative manufacturing method for He-cooled DEMO divertor components. *Fusion Engineering and Design*, *86*(9-11), 1575-1578.

[118] Murr, L. E., Gaytan, S. M., Ramirez, D. A., Martinez, E., Hernandez, J., Amato, K. N., Shindo, P.W., Medina, F.R. & Wicker, R. B. (2012). Metal fabrication by additive manufacturing using laser and electron beam melting technologies. *Journal of Materials Science & Technology*, *28*(1), 1-14.

[119] Xu, C., Bouchemit, A., L'Espérance, G., Lebel, L. L., & Therriault, D. (2017). Solvent-cast based metal 3D printing and secondary metallic infiltration. *Journal of Materials Chemistry C*, *5*(40), 10448-10455.